FEW-PHOTON NONLINEAR OPTICS IN PHOTONIC BANDGAP FIBERS

A Dissertation

Presented to the Faculty of the Graduate School

of Cornell University

in Partial Fulfillment of the Requirements for the Degree of

Doctor of Philosophy

by

Vivek Venkataraman

August 2012

FEW-PHOTON NONLINEAR OPTICS IN PHOTONIC BANDGAP FIBERS

Vivek Venkataraman, Ph.D.

Cornell University 2012

The ability to control light with light at ultralow powers has been a major avenue of research in photonics with applications to optical communications, computation, and signal processing. Such light-by-light scattering is achieved in a medium with a strong light-matter interaction, and for the development of quantum information networks it is important to demonstrate such effects near the single-photon level. Alkali-metal vapors such as rubidium (Rb) enable strong light-matter interactions due to the large cross section per atom and well-defined energy level structure, while the use of optical fibers offers the advantage of possible integration with modern optical communication systems. Hollow-core photonic band-gap fibers (PBGFs) can combine both these technologies such that both the atoms and the optical fields are transversely confined to a region that is a few wavelengths in size, which offers the prospect of exploring few-photon nonlinear interactions.

We generate large optical depths in such a Rb-PBGF system, and the tight light confinement, high vapor density and long interaction length allow us to perform nonlinear optics at ultralow power. We demonstrate large signal amplification (>100) and frequency conversion using a four-wave mixing process with only microwatts of pump power. This is, to our knowledge, the largest gain observed at such low power. We perturb the coherence of this four-wave mixing to demonstrate all-optical modulation at unprecedented bandwidths (~300 MHz) for an atomic-vapor system, with an energy density of only tens of pho-

tons per atomic cross-section, comparable to that achieved in more elaborate setups based on cold-atomic clouds. We then demonstrate an enhancement of several orders of magnitude in degenerate two-photon absorption in our Rb-PBGF system over that achieved in bulk vapor cells in a focused beam geometry. This allows us to directly measure two-photon absorption from a beam by detecting its intensity on a photodiode.

Further, employing a near-resonant, non-degenerate two-photon transition in Rb, we demonstrate all-optical intensity modulation with just a few photons (<20), or only a few attojoules of energy, at relatively large bandwidths (~50 MHz) for such a sensitive scheme. This result takes us to within an order of magnitude of single-photon switching, and improves upon previous experiments for freely propagating optical fields, including those in cold-atoms. Finally, we produce relatively large cross-phase shifts of a few milliradians on a meter beam with <20 signal photons by tuning slightly away from resonance on the same non-degenerate two-photon transition. This corresponds to a phase shift of 0.3 milliradian per photon, with a fast response time of <5 ns. This represents, to our knowledge, the largest such nonlinear phase shift induced in a single-pass through a room temperature medium. Our Rb-PBGF system can thus potentially be employed to realize weak-nonlinearity based quantum computation and quantum non-demolition measurement of photon number.

Through these experiments, we show the potential of a Rb-PBGF system for exploring quantum nonlinear optics at ultralow powers. Moreover, our system is simpler and easier to control and manipulate than setups based on cold atomic clouds and/or high-finesse cavities, and holds promise for integration with fiber-optic communication networks.

BIOGRAPHICAL SKETCH

Vivek Venkataraman was born in the city of Kolkata, located in the eastern state of West Bengal, India on 14th April 1984. Thereafter he moved north to the capital city of Delhi where he spent the first 22 years of his life. His interest in the physical sciences was piqued in high-school where he found himself marveling at the "unreasonable effectiveness of mathematics" (quoting Eugene Wigner) in explaining seemingly complicated natural phenomena. He joined the Indian Institute of Technology, Delhi in Fall 2002 to pursue his undergraduate degree in Electrical Engineering. He worked on the modeling and simulation of nanoscale strained-silicon transistors for his undergraduate thesis and obtained a Bachelor of Technology degree in Summer 2006. Vivek left his Delhi abode for the first time in Fall 2006 and came to Ithaca, NY, USA to pursue graduate study at Cornell University. He joined the Quantum and Nonlinear Photonics group of Prof. Alexander L. Gaeta in the School of Applied and Engineering Physics, and has been exploring nonlinear optical interactions at ultralow light-levels as part of his doctoral thesis research. He received a Master of Science degree from Cornell University in Spring 2010.

To my parents.

ACKNOWLEDGEMENTS

Firstly, I would like to thank my advisor Prof. Alexander L. Gaeta for giving me an opportunity to work in his group. Alex has been a constant source of inspiration and support throughout my doctoral program and has always been extremely encouraging, especially when times were tough. I always felt at home in your group and your timely advice on many matters have borne fruit on many occasions. I am also grateful to Prof. Michal Lipson, who agreed to be the chair of my special committee. My interactions with Michal have always been enjoyable and I had a very good experience as a Teaching Assistant for her courses in my first two semesters here. I am also greatly indebted to Prof. Farhan Rana, who helped me settle down and get my bearings when I first arrived in Ithaca. I am deeply appreciative of the freedom that I got to explore and figure out my path. Farhan is a great teacher and his quantum optics course was one of my best experiences at Cornell. Thank you for your insights, advice and stimulating thoughts.

I will always be indebted to my lab-mates with whom I worked and learnt a great deal about science and doing research. Amar was both my mentor and philosophical guide. He taught me everything I know about optics and experimental physics, and without him none of the work reported in this thesis would have been possible. Thanks Amar for being so patient and generous with me. Aaron lent me his advice on various matters and helped 'get my hands dirty' during my first couple of years. Thanks Aaron, you were fun to work with. Pablo worked with me on most of the experiments reported in this thesis and shepherded me through the travails of scientific research and gradschool. He was always willing to share his wisdom and rich experiences, preparing me for the real world ahead. Thank you Pablo for making me a better scientist and

person in general. Kasturi was a co-worker on experiments during the latter half of my doctoral study and a major contributor to the results reported here. Thanks for your help, support, cooperation and discussion. Bonggu taught me "life-lessons" and more over games of table-tennis and I can't imagine my time in the lab without him. You are an amazing person and I was extremely lucky to have you around. Thanks so much, and "I respect you a lot". Thanks to Yoshi, Sam, Ryan, Alessandro, Henry, Stephane, Adrea, Moti, Prathamesh, Mike, Jordan, Imad, Dan, Reza, Mark, Chris, Luat and Saikat for being wonderful colleagues at various points of time. I am also grateful to Faisal and Jahan, who were in Farhan Rana's group, for making me feel at home as soon as I arrived in Ithaca and motivating me to pursue my interests. Thanks for your advice on matters scientific and otherwise. I also thank Sasikanth, formerly in Michal Lipson's group, for encouraging me to come to Cornell and helping me find my way.

Special thanks to my great friends outside the lab who kept me sane all this while. Suresh was my housemate for five years and taught me how to appreciate life as it comes and that happiness is a state of mind. I have practically lived off him during my time in Ithaca and will forever be grateful to him. Rajendran taught me to appreciate literature and language as much as cricket, enjoy politics as much as music, understand film-noir as much as mathematics. You have opened the doors to 'hazaaron' of my 'khwahishein'. Anand has been my companion on many endeavours and I can always seem to count on him for anything and everything. We have had enjoyable and illuminating discussions on everything from bacteria to God, and I have learnt a lot from you. Sujata has been a true friend and confidante throughout my stay here, and I am very grateful for her constant support and the many 'chai' meetings that we have had. You

and Surya have been my family here in Ithaca, thanks so much. Pavithra, you have been a truly wonderful friend. Thanks for badminton, food, 'chaos' and much more. Vidhya, thanks for always lending an ear to my rants and keeping a check on my cynicism. I am lucky to have you as a true friend. Thanks to Amit and Shruti for being such wonderful neighbours and dinner companions, and making my life here a lot easier. Siddharth, thanks for being a good housemate for the last two years. Tanay, many thanks for pushing me into doing something periodically and feeding me a steady dose of laughter. Thanks to Krishna and Venkatachala for interesting conversations in the house during my first year.

Most importantly, I would like to thank my parents, because of whom I am what I am, and my wonderful brother Ashwin.

TABLE OF CONTENTS

LIST OF FIGURES

CHAPTER 1

INTRODUCTION

The ability to control light with light at ultralow powers has been a major avenue of research in photonics with applications to optical communications, computation, and signal processing [1, 2, 3, 4, 5]. The total energy per logic operation for current electronic transistors are at the femtojoule level and for all-optical logic to compete, efficient optical devices operating at the level of only hundreds of photons or below need to be developed [6]. Such light-by-light scattering, where one light beam induces changes in the amplitude and/or phase of another light beam, is achieved in a nonlinear medium with a strong light-matter interaction. It is also critical to demonstrate such nonlinear optical effects near the single-photon level for quantum information applications [7, 8]. Consequently, there is considerable interest in developing systems with high optical nonlinearities in geometries that enhance the light intensity by tight confinement of the optical mode.

1.1 Ultralow power nonlinear optics for quantum information

Performing nonlinear optics near the single-photon level is critical to the development of quantum networks [9, 10] and to fundamental studies of quantum electrodynamic (QED) effects [11, 12, 13]. Various nonlinear and quantum-optical techniques are being explored to solve problems in optical information processing, such as the realization of efficient all-optical switches [14, 15, 16, 17, 18], all-optical quantum computing gates [10, 19, 20], and quantum non-demolition (QND) measurements [21, 22, 23, 24].

Single-photon switches, where one photon controls the passage of another photon though a medium, may have useful applications in the development of quantum information networks. For example, the presence of one photon may cause another photon to be absorbed in a medium which is otherwise transparent to that photon. Such a system that absorbs two photons when they are simultaneously present but not each one separately has been theoretically proposed in an atomic vapor medium employing resonant nonlinearities and quantum interference [18]. This may have applications in the processing of quantum entangled states, such as the generation of three-fold entangled or GHZ states [25].

A strongly two-photon absorbing medium that absorbs two photons but not one can also be used to suppress failure events in a linear-optics approach to quantum computing [26], due to the quantum Zeno effect [19]. Such a medium would also allow the construction of deterministic universal logic gates for quantum computation, like the $\sqrt{(SWAP)}$ and controlled-NOT (cNOT) gates, using simple elements like evanescently-coupled optical fibers without the need for ancilla photons or high-efficiency detectors [19]. Photons can also be made to behave as fermions in such a system, in addition to their normal bosonic character, leading to a new paradigm for quantum computation [19]. Further, even heralded single photon sources can be built using such media with large two-photon absorption [27]. Classical logic gates and all-optical switches can also be implemented using these same concepts [28].

The ability to measure properties of a light field without destroying it (non-demolition measurement) is a key requirement of many quantum communication and computation protocols. A medium with a large third-order nonlinear-

ity can be employed for QND measurement of photon number via the optical Kerr effect [29]. A probe wave propagating through the medium gets a nonlinear optical phase shift proportional to the intensity, or number of photons, of a signal wave. By measuring the phase of the probe at the output through balanced homodyne detection, the signal photon number can be determined.

It has been proposed that an exceptionally strong Kerr medium, such that a single-photon in the signal wave causes a π-radian phase shift of the probe wave, can be used to build a quantum-optical Fredkin gate [30]. Such an optical Fredkin gate would be a reversible logic gate that dissipates no energy, closely related to the universal cNOT gate in quantum computing. Based on this idea, it was also shown that an all-optical simple quantum computer, capable of solving Deutsch's problem [31], can be built out of such highly nonlinear media [32].

Although the feasibility of realizing a single-photon π-phase shift remains in doubt [33], weaker Kerr nonlinearities that mediate interaction between photons through a strong coherent light field may also have useful applications in quantum optical information processing. A unified approach to quantum communication and computation has been recently proposed employing QND measurements of photons and robust distribution of quantum information through intense laser fields [34]. Such a protocol may be more feasible in terms of practical resources and the potential for scalability to many qubits.

All the above mentioned approaches require the realization of systems that can achieve measurable nonlinearities at the single-photon level and the development of schemes that can optimally exploit their nonlinear response, i.e. where the frequencies of the interacting light modes and the energy levels of the medium facilitate strong light-matter coupling [16, 18, 24, 35]. In view of this,

resonant nonlinearities in atomic vapors is a natural choice for exploring optical interactions at ultralow power.

1.2 Alkali vapors: Rubidium

In order to reach the single-photon limit, it is important to develop systems capable of generating ever-higher effective nonlinearities. A number of features are required in order to create a strong coherent nonlinear response in an atomic medium at very low photon numbers. One is a strong coupling between the light and the atomic medium. This can be achieved by maximizing $g\sqrt{OD}/\gamma$, where g is the atom-field coupling constant in units of angular frequency, OD = - log(T) is the optical depth experienced by the spatial light mode, T is the on-resonance transmission, and γ is the excited-state radiative decay rate. Another desired feature is a long spin coherence time, which requires management of various decoherence mechanisms including magnetic fields, inelastic collisions, and radiation trapping.

Alkali vapors are promising media for exploring ultralow power nonlinear optical interactions due to the large cross-section per atom, well-defined energy level structure, long interaction times, and the large optical depths (ODs) that can be achieved [36]. A number of interesting quantum and low-light level effects have been proposed and observed in such vapors, such as storage and retrieval of quantum states [37], switching at low photon number [16], quantum non-demolition (QND) measurements [11], and quantum noise correlations [38, 39].

Alkali metals are hydrogen-like elements belonging to Group 1 of the peri-

odic table with a single valence electron in the outermost shell. The inner shell electrons shield the outermost electron from the field of the atomic nucleus, resulting in a loosely bound valence electron. The outermost electron can thus be readily lost in chemical reactions, making alkali metals highly reactive even in standard ambient environments. Additionally, the small value of the atomic electric field at the outermost electron makes the atom easily polarizable under externally applied fields. With modest light intensities, one can make the external electric field approach the internal atomic electric field giving rise to nonlinearities in the optical response [40].

Rubidium (Rb, atomic number 37) lies below potassium and above cesium in the alkali-metal group. It has two naturally occurring isotopes, ^{85}Rb and ^{87}Rb in the ratio 72% and 28%, respectively. The primary electronic transitions (D_1 and D_2 lines) are resonant for light with wavelengths near 800 nm, where stable, low-noise, narrow-linewidth continuous-wave (CW) lasers are available. The oscillator strengths of these transitions are near unity, signifying a large atom-light coupling [36]. Moreover, Rb has a melting point near 40°C resulting in a large vapor pressure at room temperature (~10^{-6} torr at 33°C) [36]. This enables one to generate large vapor densities of Rb at modest temperatures. However, the high reactivity of atomic Rb makes it challenging to handle it in vapor form, and the use of ultra-high vacuum (UHV) chambers becomes necessary.

Fig. 1.1(a) shows the absorption spectrum of the Rb D_1 line. The transmission of a weak laser beam though a Rb vapor cell near room temperature is measured as it is scanned across the D_1 resonances at $\lambda = 795$ nm. The Doppler broadening at room temperature (~500 MHz) is much greater than the natural linewidth (~6 MHz) of the D_1 line determined by the lifetime of the excited state (~27 ns).

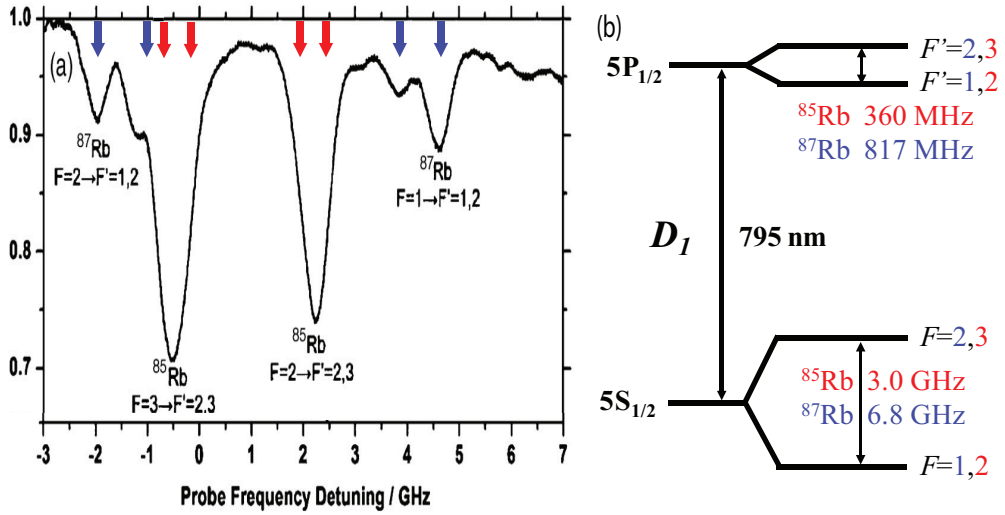

Figure 1.1: Rubidium D_1 line. (a) Transmission of a weak laser beam through a Rb vapor cell at room temperature (~300 K) as it is scanned across the D_1 resonance (λ = 795 nm). Red arrows indicate ^{85}Rb transitions while blue arrows indicate ^{87}Rb transitions. The Doppler broadening at room temperature (~500 MHz) is much greater than the natural linewidth (~6 MHz) of the D_1 line determined by the lifetime of the excited state (~27 ns). (b) Energy levels for the D_1 transition. The ground $5S_{1/2}$ state is dipole-coupled to the excited $5P_{1/2}$ state yielding a strong electronic transition. The ground $5S_{1/2}$ state is hyperfine split into two levels due to the interaction between the electron spin and nuclear spin (F denotes the total spin). The splitting is different for the two isotopes. The two ground levels are not dipole-coupled to each other and can have long lifetimes (μs - ms). At room temperature, an equal proportion of atoms are found in the two ground levels. The excited state is also split into two levels due to the hyperfine interaction.

Fig. 1.1(b) shows the atomic energy levels involved in the D_1 transition. The ground $5S_{1/2}$ state is dipole-coupled to the excited $5P_{1/2}$ state yielding a strong electronic transition. The ground $5S_{1/2}$ state is hyperfine split into two levels due to the interaction between the electron spin and nuclear spin (F denotes the total spin). The F numbers are different for the two isotopes because of the difference in their nuclear spin values (5/2 for ^{85}Rb and 3/2 for ^{87}Rb). The

splitting is 3.0 GHz for ^{85}Rb and 6.8 GHz for ^{87}Rb. The two ground levels are not dipole-coupled to each other and can have long lifetimes (μs - ms). At room temperature, an equal proportion of atoms are found in the two ground levels. The excited state is also split into two levels due to the hyperfine interaction.

Similarly, the Rb D_2 line at λ = 780 nm represents a strong dipole-allowed electronic transition coupling the ground $5S_{1/2}$ state to the excited $5P_{3/2}$ state. The spectroscopic properties of the D_2 line are similar to the D_1 line except for the excited state hyperfine structure [36]. In addition to these two primary transitions, experiments reported in this thesis also employ the higher-order $5S_{1/2} \rightarrow 5D_{5/2}$ two-photon transition at λ = 778 nm, and also the $5P_{3/2} \rightarrow 5D_{5/2}$ dipole-allowed transition at λ = 776 nm (refer to appendix for a detailed energy level structure of Rb).

1.3 Geometries for light-matter interactions

The strength of nonlinear optical interactions is proportional to the nonlinearity of the medium and the intensity of the light fields. The effective nonlinearity of the medium scales with the density of scatterers (atoms) N and the light-scattering cross-section σ_{sc} of each scatterer. The intensity of light is given by $I = P/A$, where P is the power and A is the mode area of the optical field in the medium. Thus the strength of nonlinear interactions typically depends on the parameter $N\sigma_{sc}L/A$, where L is the length of the medium. Alkali atoms like Rb have some of the largest possible values of $\sigma_{sc} \sim 3\lambda^2/2\pi$, where λ is the wavelength of light resonant with an atomic transition. The atom-photon interaction will be highest ($g \sim 1$) when the mode area A approaches σ_{sc}. Different geome-

tries of light-matter interaction can be designed in order to maximize L/A, and hence the nonlinear response, as shown in Fig. 1.2.

The simplest way to enhance the light intensity is to just focus a free-space beam into a vapor cell that may contain either thermal atoms or laser-cooled atoms [see Fig. 1.2(a)]. However, the intensity is enhanced only for the region where the beam remains focussed, which is given by the Rayleigh diffraction length $L_{df} \simeq \pi w^2/\lambda$, where w is spot size at the focus and λ is the wavelength. For a beam waist $w \sim 3$ μm, $L_{df} \sim 40$ μm for $\lambda \sim 800$ nm. This is a very small interaction length. Thus, typical experiments in bulk vapor cells have required significant power levels to see measurable effects.

Another way to enhance light-matter interaction is to use a high-finesse cavity [see Fig. 1.2(b)]. When the wavelength of light is resonant with the cavity, it bounces back and forth between the two mirrors and the intensity is enhanced by a factor of the finesse. The interaction length in the medium is also increased due to the multiple round trips. However, there are many practical issues in dealing with cavities. One has to trap the atoms in the small modal volume of the cavity, which is highly non-trivial. A large finesse results in a small cavity bandwidth making it very difficult to match it to the atomic transitions. The input-output coupling losses are also typically large due to mode matching problems between the free-space beam and the cavity mode. Although some ground-breaking experiments have been done in cavity-QED systems [12, 13, 41, 42], the technology involved is extremely elaborate and complicated with scalability being a major issue.

A third approach to enhance light-atom interactions, which we choose to employ in our experiments, is to confine light to a waveguide structure [see

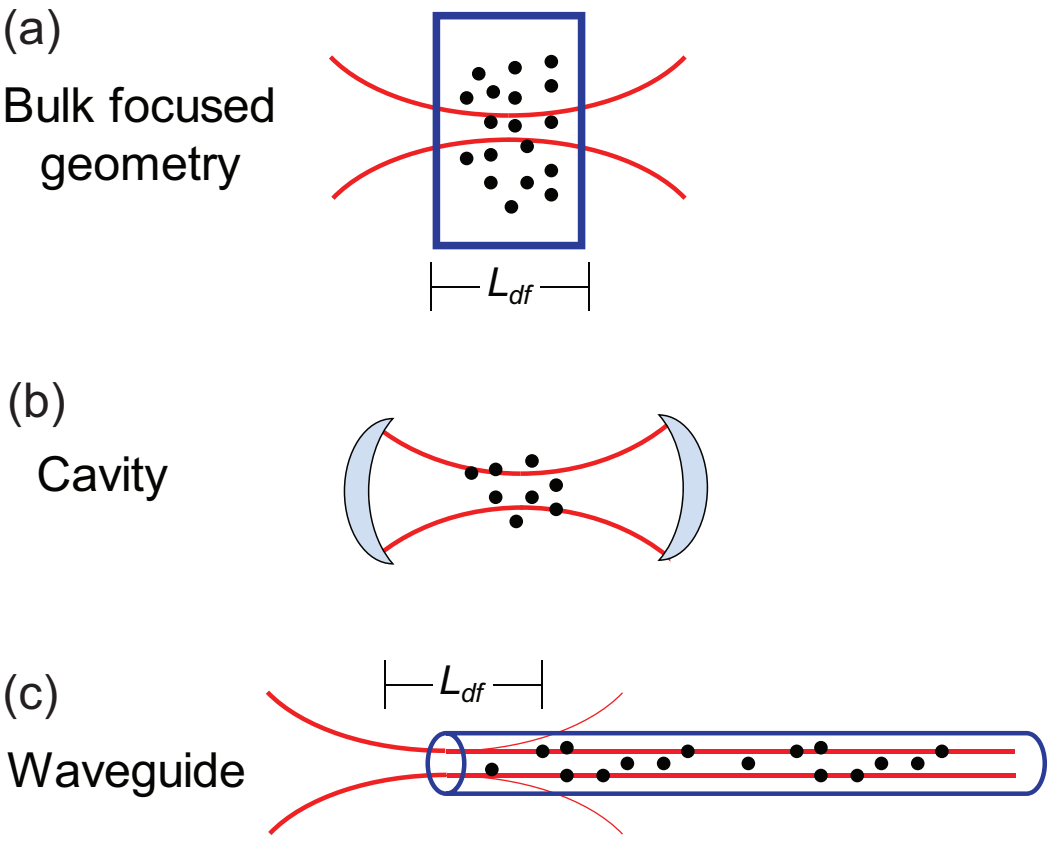

Figure 1.2: Different geometries for light-matter interactions. (a) Light is focussed free-space into a bulk vapor cell containing hot or cold atoms. The light is focussed to a small mode area and high intensity for only a length L_{df}, the Rayleigh diffraction length. (b) Light intensity is enhanced in a high-finesse cavity containing atoms trapped between its two mirrors. When the wavelength of light is resonant with the cavity, it bounces back and forth between the two mirrors and the intensity is enhanced by a factor of the finesse. The interaction length in the medium is also increased due to the multiple round trips. (c) Light is confined to a waveguide with a small mode area, with the atoms also present throughout the length of the waveguide. In this geometry, the light intensity can be enhanced for a length much greater than the Rayleigh diffraction length for a focused beam of a similar spot size.

Fig. 1.2(c)] where the vapor interacts either with the evanescent tail of the guided mode [43, 44, 45] or inside a hollow guiding structure [46, 47]. Such a geometry has the benefit of increasing the atom-photon coupling g while permitting interactions over a length much greater than the Rayleigh length of a similar-sized focused spot size. Mode diameters of a few microns can be maintained over centimeters of interaction length, greatly enhancing the nonlinear response. Moreover, one can work with freely propagating fields without the associated issues of cavities. Such a system also holds promise for integration with fiber-optic communication networks [48]. Furthermore these systems can utilize typical methods for magnetic field control and inherently suppress radiation trapping due to their high aspect ratio [49, 50]. Although short spin coherence times can be an issue due to the brief transit time across the beam cross-section, it may be possible to ameliorate the problem by trapping the vapor [51, 52], by applying a coating to walls of the system cell [53], or by using a buffer gas [54].

1.4 Hollow-core photonic bandgap fibers

Optical waveguides such as photonic band-gap fibers (PBGFs) with a hollow core [see Fig. 1.3(a)] allow various gases to be injected into the core and interact with single-mode optical fields [24, 55, 56, 57, 58, 59, 46, 60]. PBGFs consist of a Bragg structure surrounding an empty core, typically a few microns in diameter. The core supports guided mode propagation for many tens of meters. This architecture confines both the atoms and photons to a small transverse area, which permits weak fields to interact strongly with the atoms over a length that is much larger than the Rayleigh diffraction length for a focused beam of a

similar spot size.

The concept of a photonic bandgap is exactly analogous to the energy bandgap that arises for electron transport in a periodic crystal. The atomic lattice for the electronic case is replaced by a periodic refractive index variation for the photonic case. Using this principle, it was proposed [61] and demonstrated [62] that light can be guided in a low-index region surrounded by a Bragg structure. Hollow-core PBGFs are made using the stack and draw technique where hollow glass capillaries are stacked together, seven capillaries from the center are removed and the remaining structure is fused and drawn into fibers. The drawn fibers maintain the aspect ratio of the original structure and display a bandgap determined by the spacing (pitch) of the air-holes and the refractive index contrast. These fibers can also be dispersion-engineered and show very low nonlinearities from the silica structure itself because most of the light (> 92%) is confined to the hollow core [63].

The specific PBGF that we use for our experiments is the AIR-6-800 manufactured by NKT Photonics [64]. The fiber guides light with low loss and a fundamental mode area ~10 μm^2 in the 740-810 nm range, encompassing wavelenghts of the D_1, D_2 and two-photon transitions of Rb probed in our experiments [see Fig. 1.3]. Rb vapor is generated in the central core region, which then interacts with the light fields coupled into the core of the fiber.

The ability to generate large optical depths of Rb vapor inside of a hollow-core photonic band-gap fiber (PBGF) has been demonstrated previously by our group [46, 65]. A strong off-resonant light field causes Rb nanoclusters adsorbed on the inside walls to evaporate [66, 67], generating a vapor in the core that can interact with guided fields present in the fiber. However, the tight confinement

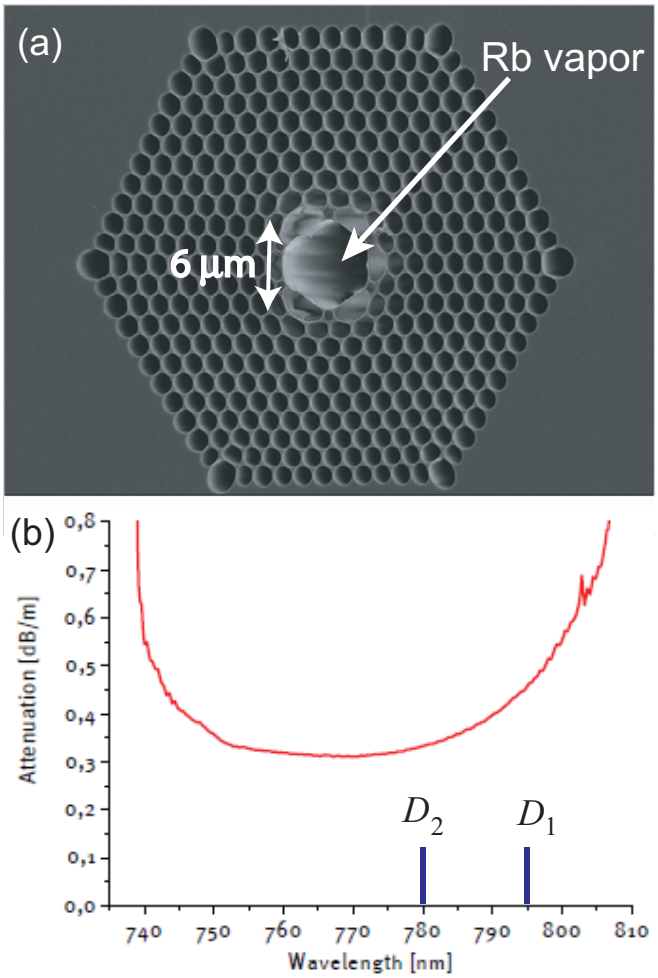

Figure 1.3: AIR-6-800 fiber from NKT Photonics. (a) Transmission electron microscope image of the cross section of the fiber used in these experiments. The core diameter is 6 μm and the fundamental mode area is ~10 μm^2 for the guided optical field. Rubidium vapor is generated in the central core region, which then interacts with the light fields coupled into the core of the fiber. (b) Spectral attenuation of the fiber [64]. The fiber guides light with low loss in the 740-810 nm range, encompassing wavelenghts of the D_1, D_2 and two-photon transitions of Rb probed in our experiments.

of thermal atoms and photons give rise to additional spectroscopic features such as transit-time broadening that must be taken into account [68]. The next section describes our Rb-PBGF system in a bit more detail.

1.5 The Rb-PBGF system

Our Rb-PBGF system basically consists of an ultra-high vacuum (UHV) chamber with a Rb source attached, inside of which one or more PBGFs are mounted. There are glass windows on each side to couple into and out of either end of the fiber(s). The details of the preparation of the UHV chamber have been described previously [67]. After initial bake-out of the chamber at 150-200°C for 3-4 days to reach a background pressure $<10^{-8}$ torr, an ampoule of Rb sitting inside a steel appendage (cold-finger) to the chamber is broken. Thereafter, the chamber is kept at 80-85°C and the Rb cold-finger is kept at 50-55°C for 1-2 weeks. During this time, the chamber "ripens" i.e. Rb atoms attach themselves to the inner surfaces of the chamber by chemically reacting with every available adsorbed oxygen or water molecule and any dangling OH-bonds. Once every reactive site has been covered, only then will a stable, ambient Rb vapor form in the chamber [69]. Once the vapor density (monitored through a weak laser scanning across the absorption lines) reaches a steady state value, the temperature of the chamber and cold-finger are brought down to ~60°C and ~40°C respectively for normal operation. Atoms from the ambient Rb vapor then start diffusing down the hollow core of the PBGF. Most of these atoms attach themselves to the inner silica walls forming Rb nanoclusters [66, 67], such that there is no Rb vapor inside the fiber core under steady state conditions.

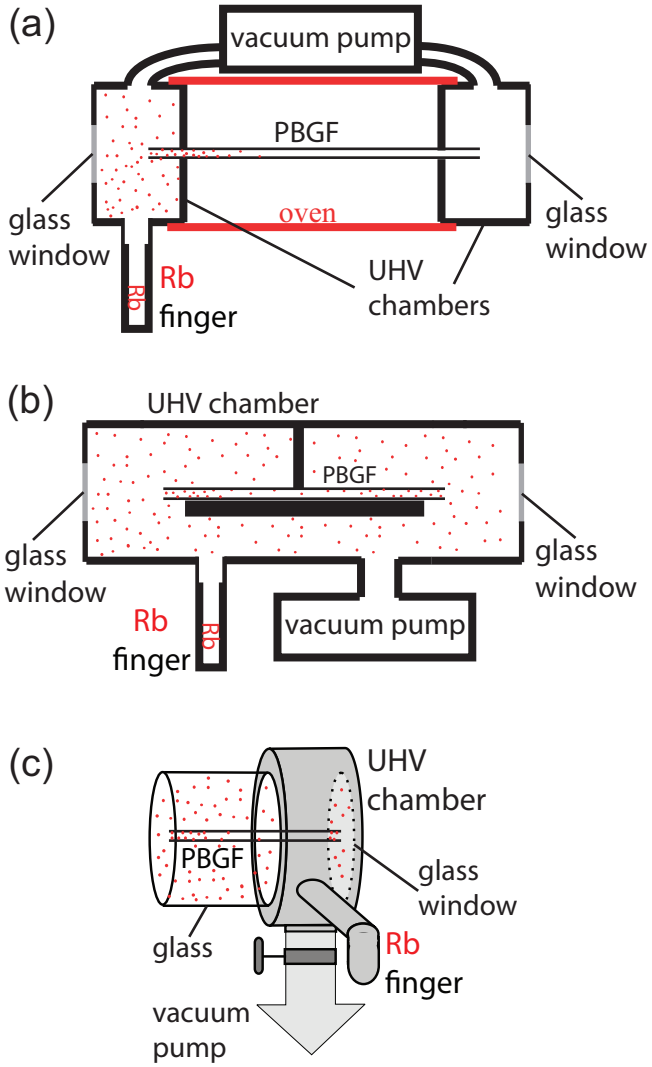

Figure 1.4: Evolution of the Rb-PBGF chamber design. (a) First generation chamber. A ~30-cm PBGF links two UHV cells. The Rb source is attached to one of the cells. This chamber design was used for the four-wave mixing experiment discussed in chapter 2. (b) Second generation chamber. ~3-cm PBGFs are mounted on a holder inside a UHV chamber with a Rb source attached. This chamber design was used for all-optical modulation of four-wave mixing discussed in chapter 3. (c) Third generation chamber. ~9-cm PBGFs are mounted inside a UHV chamber with a Rb source attached. On one side of the stainless steel UHV chamber, a cylindrical glass tube is attached that provides optical access to all sides of the fiber. This chamber design was used for experiments probing the two-photon transitions of Rb discussed in chapters 4, 5 and 6.

The design of the Rb-PBGF chamber has been revised a couple of times since the initial setup [see Fig. 1.4]. The first generation chamber consisted of a long ~30-cm fiber connecting two separate UHV chambers, one of which has a Rb source attached. The motivation for such a design was to have a long interaction length without having to ripen a large chamber [67]. This chamber design was used for the four-wave mixing experiment discussed in chapter 2. However, the epoxy seals connecting the fiber from atmosphere to vacuum at the two chambers were always a potential threat for a leak and limited the ultimate vacuum quality, and hence the chamber lifetime and optical depths achieved. Additionally, the Rb vapor was found to diffuse no more than ~1 cm into the fiber core, rendering such long fiber lengths useless [70]. The second generation chamber was a much simpler single-cell design, inside which multiple PBGFs (~3-cm length) could be mounted on a holder. This chamber design was used for all-optical modulation of four-wave mixing discussed in chapter 3. A smaller chamber and the elimination of epoxy fiber seals resulted in a much better vacuum quality, extending the chamber lifetime greatly. In addition, the PBGF was exposed to Rb vapor from both ends such that more atoms could diffuse into the core. The generation of large optical depths (>1000) of Rb was demonstrated in such a chamber [65]. Finally, a third generation chamber was designed for experiments probing the two-photon transitions of Rb reported in chapters 4, 5 and 6. The design was similar to the second-generation except for a cylindrical glass tube on one side of the UHV chamber providing optical access to all sides of the fiber, enabling us to collect two-photon fluorescence and also resonance fluorescence emitted from the atoms in the fiber core. We could thus image the Rb atoms diffused into the PBGF core, and found that the atoms were distributed over a ~1 cm length.

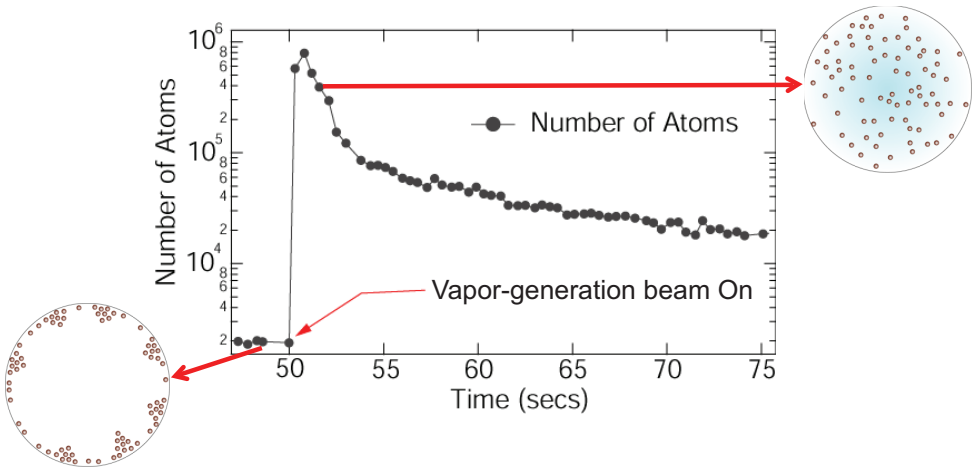

Figure 1.5: Generation of Rb vapor inside the PBGF core [46, 67]. Under steady-state conditions, the Rb atoms inside the PBGF core are all stuck to the inside walls of the fiber forming nanoclusters (bottom left). A strong vapor-generation beam at ~805 nm (far detuned from the atomic transitions of Rb) coupled into the PBGF heats and evaporates the adsorbed nanoclusters, creating a vapor of Rb atoms in the core (top right). The vapor density in the core is set by the generation beam power and duration.

As mentioned earlier, under steady-state conditions, the Rb atoms inside the PBGF core are all stuck to the inside walls of the fiber forming nanoclusters. In order to generate a Rb vapor inside the core, a strong (few mWs) vapor-generation beam at ~805 nm (far detuned from the atomic transitions of Rb) is coupled into the PBGF that heats and evaporates the adsorbed nanoclusters [66, 67]. The vapor density in the core is set by the generation beam power and duration [71]. As more nanoclusters are heated, the Rb vapor density inside the core increases. The vapor generation dynamics are shown in Fig. 1.5. We demonstrate the ability to generate large atomic densities (and optical depths) of Rb inside the hollow-core of PBGFs all-optically without the need for any change in the temperature of the cell. This is a fast, on-demand, controllable and repeatable way to produce desired vapor densities for various light-matter

interactions [66].

1.6 Thesis layout

In this thesis, we describe various experiments that demonstrate the potential of the Rb-PBGF system for exploring quantum nonlinear optics at ultralow powers. In chapter 2, we discuss the observation of large signal amplification and frequency conversion via extremely efficient four-wave mixing with microwatts of pump power. In chapter 3, we show that the coherence of this four-wave mixing process can be perturbed using an external switching field, and demonstrate all-optical intensity modulation with tens of photons per atomic cross-section. Chapter 4 discusses the enhancement of degenerate two-photon absorption in our Rb-PBGF system by several orders of magnitude over bulk vapor cells. In chapter 5, we describe the demonstration of significant all-optical intensity modulation with <20 photons using a non-degenerate two-photon transition. Chapter 6 reports the observation of large cross-phase modulation at the few-photon level using the same two-photon level scheme. We conclude in chapter 7 with a discussion of possible future experiments that may be investigated in the Rb-PBGF system following this work.

CHAPTER 2

ULTRALOW-POWER FOUR-WAVE MIXING

In this chapter, we describe the demonstration of extremely efficient four-wave mixing with gains greater than 100 at microwatt pump powers and signal-to-idler conversion of 50% in our Rb-PBGF system. We present a theoretical model that demonstrates such efficiency is consistent with the dimensions of the fiber and the optical depths attained. This is, to our knowledge, the largest four-wave mixing gain observed at such low total pump powers and the first demonstrated example of four-wave mixing in an alkali system with a large (~30 MHz) ground state decoherence rate.

2.1 Four-wave mixing in alkali vapor

Four-wave mixing (FWM) is the coherent exchange of energy among four different electromagnetic field modes that are propagating through a medium with a third-order nonlinearity $\left(\chi^{(3)}\right)$ [see Fig. 2.1]. Alkali atoms such as Rb can have relatively large ($\chi^{(3)}$) values due to near-resonant enhancement and the high oscillator strengths of their transitions. FWM experiments in particular provide a test bed for measuring the low-light interaction strengths that can be achieved in an alkali system while generating interesting effects such as frequency conversion, gain, optical phase conjugation, and relative intensity squeezing of light modes [72, 73, 74]. Here we show that large vapor densities can be produced in the Rb-PBGF system to generate nonlinear FWM at ultra-low pump powers. Efficient frequency conversion and large gain are demonstrated at only microwatts of pump power.

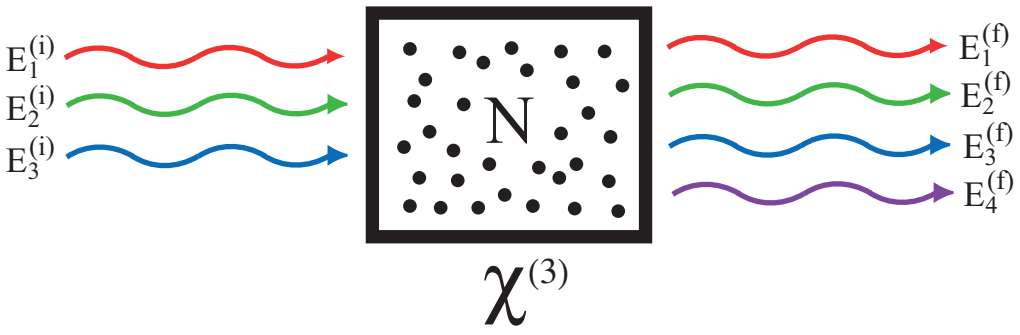

Figure 2.1: FWM in a nonlinear $\left(\chi^{(3)}\right)$ medium. Four different electromagnetic field modes (E_1, E_2, E_3 and E_4) can mix and exchange energy with each other while propagating through a medium with a third-order nonlinearity $\left(\chi^{(3)}\right)$. The field modes E_1, E_2, E_3 and E_4 can differ in frequency (energy), wave-vector (propagation direction) and/or polarization. As an example, the figure shows three input fields that undergo a nonlinear interaction and generate a fourth field at the output. Alkali vapors such as Rb can yield large $\chi^{(3)}$ values, many orders of magnitude larger than typical solid-state media.

2.2 Double-lambda FWM scheme

We investigate FWM in our Rb-PBGF system by employing a double-lambda configuration as shown in Fig. 2.2. Such interactions have been explored to study processes like generation of correlated photon pairs [73, 75], ultraslow propagation of entangled optical pulses [76], and mirrorless optical parametric oscillation [39]. The basic scheme consists of two ground states coupled to a single excited state by two pump fields. Pump field Ω_1 is on resonance with the $1 \leftrightarrow 3$ transition, while pump field Ω_2 is detuned to the blue of the $2 \leftrightarrow 3$ resonance by Δ. The weak signal field E_s is detuned from the $1 \leftrightarrow 2$ Raman transition involving E_s and Ω_2 by the quantity $\delta = \Delta' - \Delta$. This produces an idler field which is detuned from the $1 \leftrightarrow 2$ Raman transition involving E_i and Ω_1 by the quantity $-\delta$.

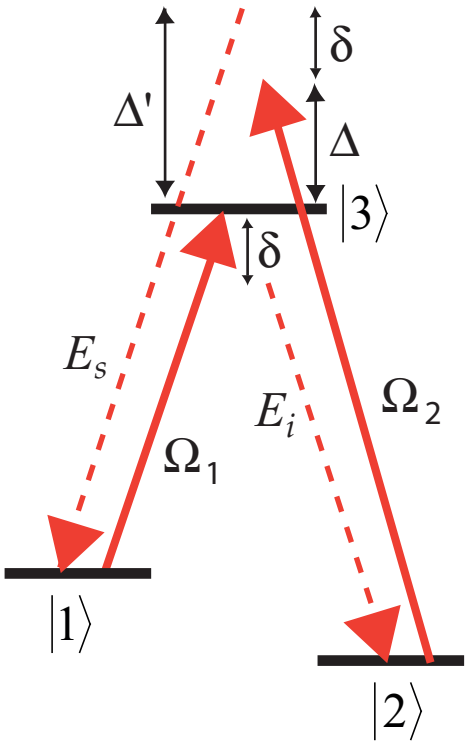

Figure 2.2: Energy-level diagram of the double-lambda FWM scheme. Pump fields of Rabi frequency Ω_1 and Ω_2 mix with the signal field E_s and the generated corresponding idler field E_i. Pump Ω_1 is on resonance while Ω_2 is blue-detuned from the excited state by Δ. The signal field is detuned from the excited state by Δ', and thus from the two-photon Raman resonance by $\delta = \Delta' - \Delta$. This generates an idler field E_i which is detuned from its Raman resonance by $-\delta$.

2.3 Theoretical modeling of FWM in confined geometry

The system is modeled assuming a thermal density matrix for the ensemble of atomic states, and transit-time broadening effects are added phenomenologically. The resulting Bloch equations are coupled to signal- and idler-field propagation through the susceptibilities of the respective wave equations. The set of equations can then be simplified to yield coupled wave equations for the signal and idler.

Since the atoms in the fiber exhibit inelastic scattering against the fiber walls at a rate of $\gamma_T/2\pi \sim 30$ MHz and have an excited state decay rate of $\gamma/2\pi = 6$ MHz, the system cannot be optically pumped into a pure state. Thus population in either of the ground hyperfine states $|1\rangle$ and $|2\rangle$ generates FWM incoherently with respect to population in the other hyperfine state. We follow the analysis outlined in [77], but also take into account the presence of atomic population in both ground states and Rabi cycling of population between states $|1\rangle$ and $|3\rangle$ due to Ω_1. This leads to the following coupled equations between the signal and idler fields that are more complicated than other systems:

$$\begin{aligned}\left[\frac{\partial}{\partial t}+c\frac{\partial}{\partial z}\right]E_s &= -i\frac{\alpha}{2}\left[(2A_2-A_1)+A_1\cos(2\Omega_1 t)\right]E_i^* \\ &\quad -iA_1\frac{\alpha}{2\Omega_1}\left[\gamma_T\sin(2\Omega_1 t)+2\Omega_1\cos(2\Omega_1 t)+\sin(2\Omega_1 t)\frac{\partial}{\partial t}\right]E_i^* \\ &\quad +(A_2-A_1)\frac{2\eta\gamma_L}{\gamma}\left[\gamma_T+\frac{\partial}{\partial t}\right]E_s \qquad (2.1)\end{aligned}$$

$$\begin{aligned}\left[\frac{\partial}{\partial t}+c\frac{\partial}{\partial z}\right]E_i^* &= +i\alpha(A_2-A_1)E_s \\ &\quad -\frac{\eta}{2}\left[(2A_2-A_1)\gamma_T+A_1\gamma_T\cos(2\Omega_1 t)-3A_1\Omega_1\sin(2\Omega_1 t)\right]E_i^* \\ &\quad -\frac{\eta}{2}\left[(2A_2-A_1)+A_1\cos(2\Omega_1 t)\right]\frac{\partial}{\partial t}E_i^*, \qquad (2.2)\end{aligned}$$

where γ_T is the inverse of the atomic transit-time across the fiber core, $\Omega_{1(2)}$ is the Rabi frequency of the corresponding field in Fig. 2.2, $\eta = g^2N/|\Omega_1|^2$, $g = d_{32}\sqrt{\omega_{32}/2\hbar\epsilon_0 V}$ is the atom-field coupling constant, d_{32} is the dipole moment of the $3 \leftrightarrow 2$ transition, ω_{32} is the angular frequency of the $3 \leftrightarrow 2$ transition, V is the quantization volume, N is the number of atoms, $\alpha = \eta\Omega_1\Omega_2/\Delta$, $\gamma_L = \gamma|\Omega_2|^2/2\Delta^2$, and $A_1 = 1/2 - \gamma/8\gamma_T$ and $A_2 = 1/2 + \gamma/8\gamma_T$ are the average steady-state populations of states $|1\rangle$ and $|2\rangle$, respectively.

Taking the limiting case of cold atoms ($A_1 = 0$, $A_2 = 1$, $\gamma_T = 0$), we note that one recovers expressions for FWM in a pure state [77]. In the full thermal

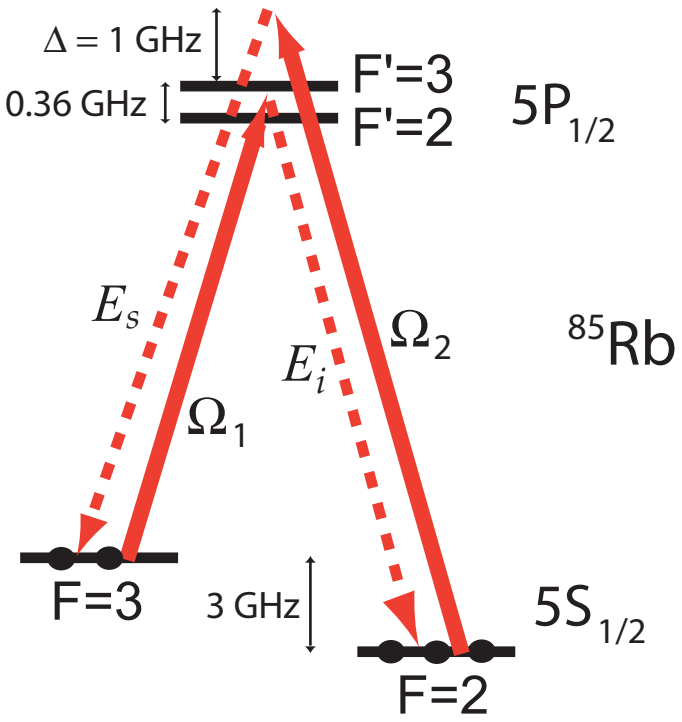

Figure 2.3: Level scheme for four-wave mixing in ^{85}Rb on the D_1 line. One pump is blue detuned by 1 GHz from the $F = 2 \rightarrow F' = 3$ transition while the other pump is tuned between the $F = 3 \rightarrow F' = 2$ and $F = 3 \rightarrow F' = 3$ transitions. A slight population imbalance ($\sim 5\%$) between the two ground states $F = 2$ and $F = 3$ is created within the transit time of the atoms across the fiber core. The signal field E_s acquires gain as a result of the FWM process and a corresponding idler field E_i is generated.

case, the presence of population in both states leads to a variety of effects. The signal and idler are cross-coupled by a number of terms proportional to α which generate FWM. Raman gain and loss are represented by the terms proportional to η. The presence of sinusoidal terms is due to population in state $|1\rangle$, which oscillates at the Rabi frequency of the resonant pump field.

2.4 FWM level scheme

The FWM interaction in our Rb-PBGF system is realized experimentally using the ^{85}Rb $5S_{1/2} \rightarrow 5P_{1/2}$ (D_1) transitions [see Fig. 2.3]. The $F = 2$ and $F = 3$ states associated with the $5S_{1/2}$ level are separated by 3 GHz and serve as the ground states of the system. The excited-state interaction takes place with both the $F' = 2$ and $F' = 3$ states of the $5P_{1/2}$ level, which are separated by 360 MHz and are thus within each others' Doppler-broadened profile. Pump Ω_2 is detuned 1 GHz to the blue of the $F = 2 \rightarrow F' = 3$ transition, and Ω_1 is tuned in between the $F = 3 \rightarrow F' = 2$ and $F = 3 \rightarrow F' = 3$ transitions.

2.5 Experimental setup

The setup for generating and measuring FWM is shown in Fig. 2.4. We use a 30-cm PBGF (Crystal Fiber AIR-6-800, 6 μm core, $\sim 3\mu$m FWHM fundamental field mode) that links two vacuum cells with a Rb source attached to one of the cells, as described in previous experiments by our group [46]. The pump beams are combined with the signal field E_s, using a polarization beam splitter (PBS) cube at the input of the PBGF. This ensures that the polarization of the pump and signal fields are orthogonal. All three beams are on continuously. We generate Rb vapor in the fiber core with 3 mW of power at 808 nm (detuned far from any Rb resonances) coupled counter-propagating to the pump and signal waves. The vapor-generation beam is pulsed with an acousto-optic modulator for the duration necessary to generate the desired OD in the fiber [66, 67], typically between 1 and 2.5 seconds. The frequency of the probe field E_s is scanned over 1.5 GHz at a rate of 10 Hz about the two-photon Raman resonance at $\delta = 0$ and the

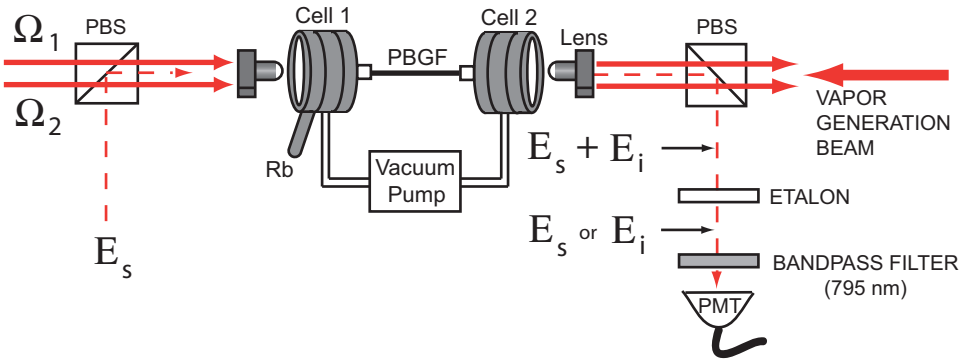

Figure 2.4: Experimental setup for observing ultralow power FWM. Pump fields Ω_1 and Ω_2 are combined with a cross-polarized signal field on a polarizing beam splitter (PBS), and propagate collinearly through the PBGF. The fiber is sealed to two vacuum cells, the left-most of which contains Rb vapor which enters the core of the fiber and attaches to the fiber walls. The vapor density is controlled by a counter-propagating vapor-generation beam of a chosen duration and power. The signal and idler fields are separated from the pump fields at the output by a polarizing beam splitter (PBS), and from each other by an etalon.

signal (E_s) and idler (E_i) powers are measured. The signal and idler fields are separated from the pump waves using a PBS cube at the output of the fiber. A temperature-controlled etalon (FSR = 40 GHz, finesse = 100) is then used to selectively transmit either of the fields onto a photo-multiplier tube (PMT) (Hamamatsu H7422-50). The output of the PMT was integrated into 100-μs time bins. A 795-nm bandpass filter in front of the PMT serves to remove any backscatter from the vapor-generation beam. We note that the continuous pump and signal field, 1 - 2.5 s desorption pulse, the signal field scanning rate given above, and the 100 μs integration time of the PMT output imply that these measurements are performed in the steady-state limit of equations (2.1) and (2.2).

2.6 Signal gain and frequency conversion

Our results are shown in Fig. 2.5 for an input signal power of 6 nW. A high OD is generated in the fiber by a 3-mW, 1-s long vapor-generation pulse. Figure 2.5(a) shows the probe transmission as it is scanned across the D_1 transition. Fitting the Rb resonances to the OD profile, taking into account transit time broadening and the temperature of the atoms generated in the fiber core [65, 68], we estimate an OD = 20 on resonance. In the presence of the pump waves, the signal field acquires gain when it is two-photon resonant with Ω_2 [see Fig. 2.5(c)]. We observe a signal field gain factor of 6 with 15 μW of total pump power at a power ratio of $|\Omega_2|^2 : |\Omega_1|^2 = 2 : 1$. When the etalon is set to transmit the idler field, we observe the power of the generated idler beam [see Fig. 2.5(b)] to be 50% that of the input probe. The idler field is not observed if any of the input fields are blocked, which corroborates that the FWM process is present inside the fiber.

We compare this data to a numerical integration of equations (2.1) and (2.2), which represent an approximate description of the experiment and which allow us to draw some general conclusions. Doppler broadening is not included, which affects the detuning of Ω_2 and introduces a detuning for Ω_1. We assume the pump beams are not absorbed by the medium since they are approximately 10^3 times the saturation intensity of rubidium atoms confined to the fiber core [68]. Inserting our experimental parameters and allowing only the atom number in the fiber to vary, we find the model predicts a gain of 6 for $N = 2.3 \times 10^5$ atoms. This value is reasonable when compared to the number of atoms required to fit to the absorption profile of Fig. 2.5(a), which we found to be 5.2×10^5 and suggests that the observed gain is consistent with the magnitude

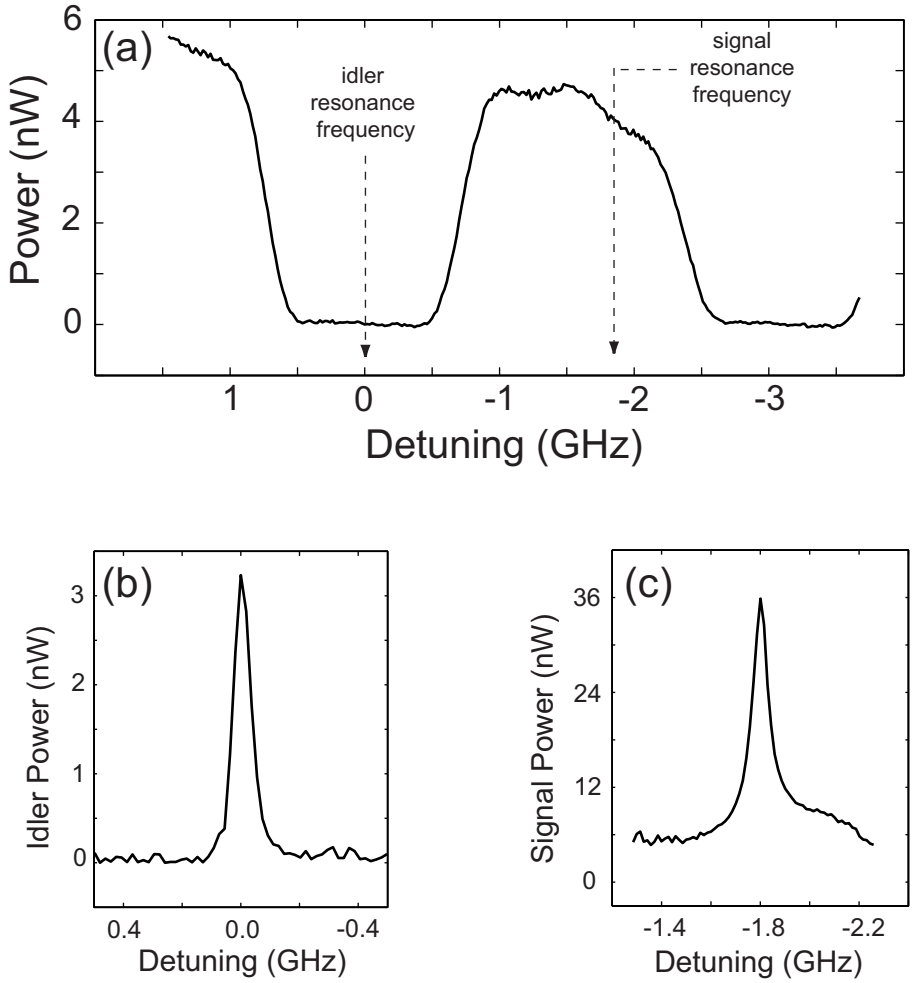

Figure 2.5: Ultralow power FWM. (a) Signal transmission through the fiber as its frequency is scanned across the D_1 line after generation of a dense Rb vapor (OD = 20). (b) Idler power versus frequency as detected while scanning the signal detuning. The input signal power is 6 nW and the total pump power in the fiber is 15 μW. 50% signal-to-idler frequency conversion is observed. (c) Gain (~6 at two-photon resonance) experienced by the signal field as a function of detuning.

one expects from FWM in the system.

2.7 Large amplification over wide bandwidth

At larger ODs and slightly larger pump powers, we observe dramatically higher gain at the signal frequency. As shown in Fig. 2.6, 36 μW of total pump power and a 2.5-s pulse of the vapor-generation beam (OD ~ 40) yield a peak gain of 105. The logarithmic plot of the gain curve shows that this imaginary component of the susceptibility is present over the 3-dB bandwidth of 300 MHz, which is capable of supporting 500-ps pulses. These gain efficiencies and bandwidth values are many orders of magnitude greater than similar experiments in bulk vapor cells. Hemmer *et al*. used a similar scheme in sodium vapor to observe a gain of 55 and response times of ~1 μs using 10 mW of pump power [72]. Boyer *et al*. observed a gain of 30 and bandwidth of ~10 MHz in rubidium vapor using 280 mW of pump power [76], though it should be noted that their double-lambda scheme used a degenerate pump that was off-resonance from all transitions.

Numerical integration of the propagation equations (2.1) and (2.2) yields an equivalent gain at 4.5×10^5 atoms, which is only twice that required for a gain of 6. This may be due not only to the exponential increase in gain as a function of N, but also to the transition into the high-gain regime, where the loss terms are weak compared to the cross-coupling strength.The observed effective nonlinearity is limited primarily by the number of atoms in the core and transit-time broadening, which is evident from equations (2.1) and (2.2). The cross-coupling coefficient α is proportional to the number of atoms, and the magnitude of the

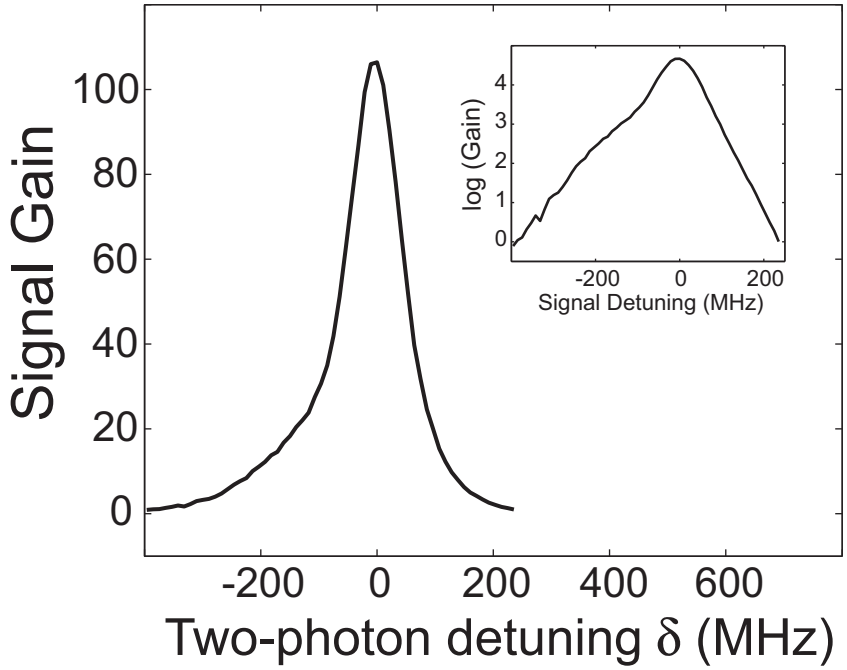

Figure 2.6: Large amplification over wide bandwidth. Signal gain versus two-photon Raman detuning for Rb vapor generated from a 2.5-s vapor-generation pulse (corresponding to an OD ~ 40 in the fiber). Gain of more than 100 is observed. The input signal power is ~1 nW and the total pump power in the fiber is 36 μW. Inset: The nonlinear susceptibility bandwidth can exceed 300 MHz and thus the system can amplify pulses as short as 500 ps.

DC cross-coupling terms increases as γ_T decreases.

2.8 Off-resonant FWM with degenerate pumps

We have also performed FWM with degenerate pumps in our Rb-PBGF system, using the scheme of McCormick *et al*. [74] where all pump, signal, and idler fields are off resonance and away from any absorption [see Fig. 2.7]. A weak gain (~1.7) is observed over a very wide bandwidth ($\gtrsim$ 500 MHz) [see Fig. 2.8]

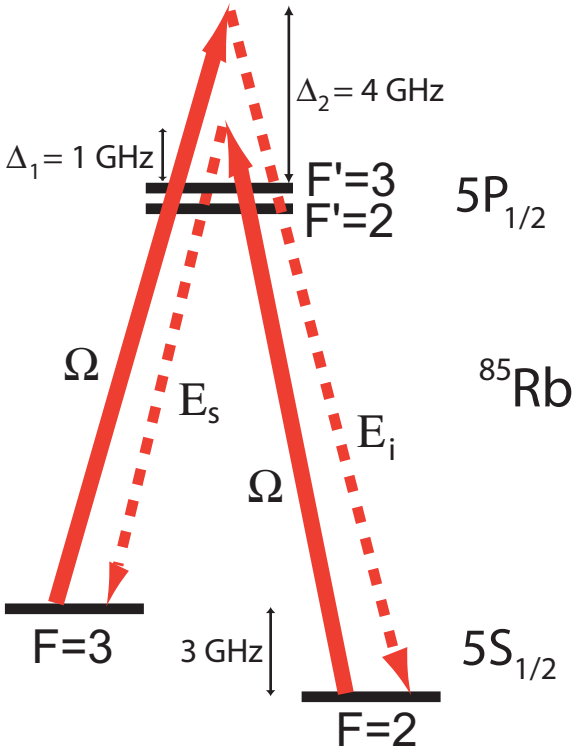

Figure 2.7: Level scheme for off-resonant FWM in ^{85}Rb on the D_1 line. A single degenerate pump (Ω) is used, which is blue detuned by 1 GHz from the $F = 2 \rightarrow F' = 3$ transition (and hence 4 GHz from the $F = 3 \rightarrow F' = 3$ transition). The pump, signal (E_s) and idler (E_i) are all far enough detuned to eliminate any absorption losses.

for 18 μW of pump power and an OD $\sim$ 20. This is particularly intriguing since it can in principle produce a high degree of nonclassical correlation between signal and idler even at low gain, and so may be usable for generation of correlated photon pairs.

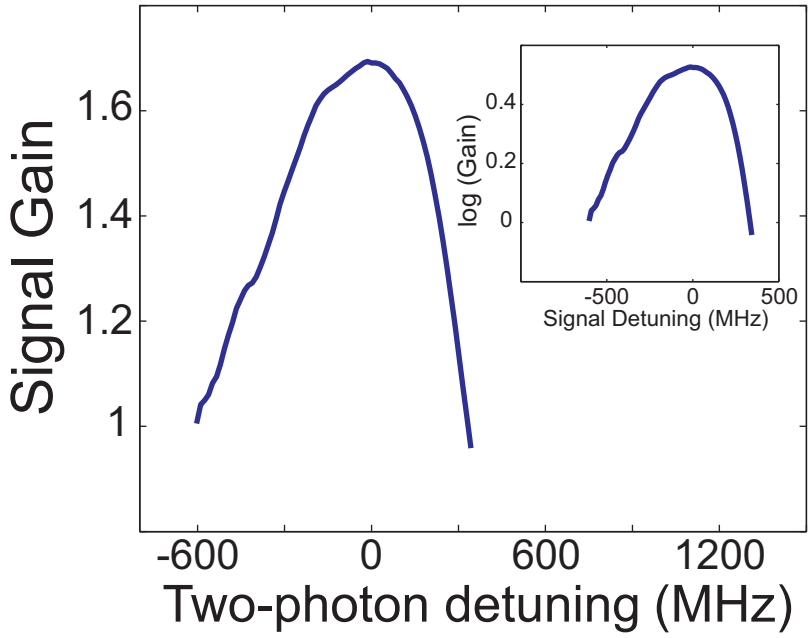

Figure 2.8: Observation of off-resonant FWM. Signal gain versus two-photon Raman detuning for FWM with degenerate pumps. The input signal power is 4 nW and the total pump power in the fiber is 18 μW. An OD ~ 20 is attained in the fiber. Inset: The nonlinear susceptibility bandwidth exceeds 500 MHz.

2.9 Summary and conclusion

There are a number of improvements that could further increase the nonlinearities we observe. Later experiments on redesigned Rb-PBGF chambers [65] show that it is be possible to produce ODs more than an order of magnitude larger than those presented in this chapter. One would expect the imaginary component of the susceptibility to increase accordingly. Another approach is to try to produce a purer state amongst the ground hyperfine levels by increasing the transit time, such as by injecting buffer gas into the PBGF [67].

In summary, our measurements show that this system can achieve extremely

efficient nonlinearities, with FWM gains >100 at only 36 μW of total pump power. This is, to our knowledge, the largest four-wave mixing gain observed at such low total pump powers and the first demonstrated example of FWM in an alkali-metal system with a large (~ 30 MHz) ground state decoherence rate. As such, this fiber-based system shows promise for studying other novel nonlinear optical effects such as classical and quantum noise correlations [78, 75] and dispersive effects from EIT and gain resonances [76], at ultra-low light levels and with exceptionally high bandwidths for an alkali vapor system.

CHAPTER 3

ALL-OPTICAL MODULATION OF FOUR-WAVE MIXING

In this chapter, we describe the demonstration of efficient all-optical modulation using a coherence perturbation of the four-wave mixing (FWM) scheme discussed in the previous chapter. The intensity of a signal field participating in the FWM process is modulated using a weak switching field. We observe 3-dB of attenuation in the signal field with only 3600 photons of switching energy, corresponding to ~36 photons per atomic cross-section $\lambda^2/2\pi$. In addition, tunable modulation bandwidths as high as 300 MHz are observed.

3.1 Coherence perturbation

Resonantly enhanced multi-level atomic interactions are attractive for exploiting low light level optical phenomena based on quantum interference in alkali atoms. Coherent interactions that exploit narrow resonances have yielded novel nonlinear processes such as electromagnetically-induced transparency (EIT) [79] and coherent population trapping (CPT) [80]. For example, in a lambda scheme two optical probe fields couple two ground states of the atom to a single excited state and establish coherence between the two ground states, which results in atom-light states called polaritons. Similar effects can be generated by using a double-lambda scheme, which uses four optical fields to couple the two ground states to an excited state in a four wave mixing (FWM) process [38, 77]. For example, the double lambda FWM process involving the two pump fields $\Omega_{1,2}$ and the signal (E_s) and idler (E_i) fields, as shown in Fig. 3.1, sets up a spatially varying coherence between the two ground states $|1\rangle$ and $|2\rangle$

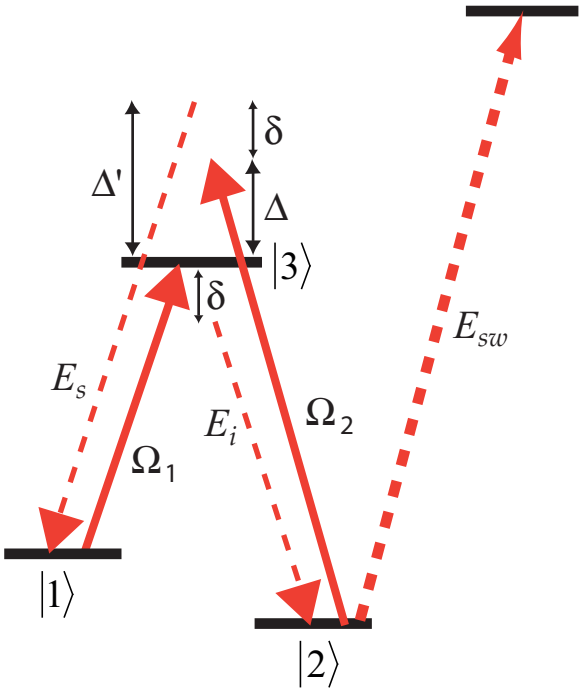

Figure 3.1: Perturbation of ground state coherence via an external field. The double lambda FWM process involving the two pump fields $\Omega_{1,2}$ and the signal (E_s) and idler (E_i) fields sets up a spatially varying coherence between the two ground states $|1\rangle$ and $|2\rangle$ in the medium. An external switching field E_{sw} can perturb this coherence leading to a change in the transmission of the signal and idler fields.

in the medium given by

$$\sigma_{12}(x) \simeq |\sigma_{12}| \exp i(k_1 - k_i + k_2 - k_s)x, \tag{3.1}$$

where k_1, k_2, k_s and k_i are the wavevectors of the two pumps and the signal and idler fields, respectively. These polaritons can interact with other external optical fields and can be used to perturb the atomic ground state coherence resulting in the change in transmission of a probe beam [81]. The external perturbing field, or switching field, usually couples one of the ground states to another separate excited state. An on-resonance switching field can be used for low power all-optical modulation or switching [18], while a slightly off-resonant switching

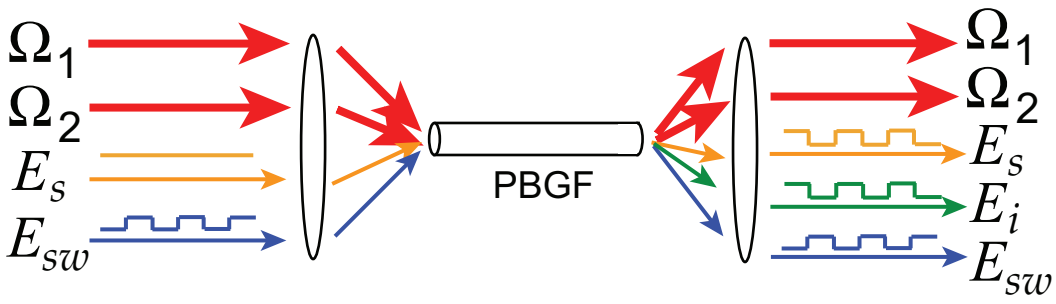

Figure 3.2: All-optical modulation of FWM. A switching field E_{sw} induces modulations on a continuous wave (CW) signal field (E_s) which is participating in a FWM process. The medium consists of Rb atoms confined to the hollow-core of a PBGF. The signal field, which acquires gain under normal conditions, is attenuated in the presence of the switching field. Modulations are also induced on the generated idler field.

beam can be employed for QND detection schemes [24].

Here we present all-optical intensity modulation of a signal field that is participating in the FWM process in our Rb-PBGF system [see Fig. 3.2]. We have previously shown that large optical depths can be generated in a Rb-PBGF system [65], which can result in large effective nonlinear susceptibilities and FWM gains greater than 100 with microwatts of pump power [82]. Consequently, introducing a field that can perturb this waveguide-based FWM allows us to study all-optical perturbations of highly nonlinear behavior at extremely low light powers.

3.2 Energy level scheme

The energy level diagram for our scheme is shown in Fig. 3.3. We use a double-lambda scheme on the D_1 line (795 nm) of ^{85}Rb to observe FWM with non-

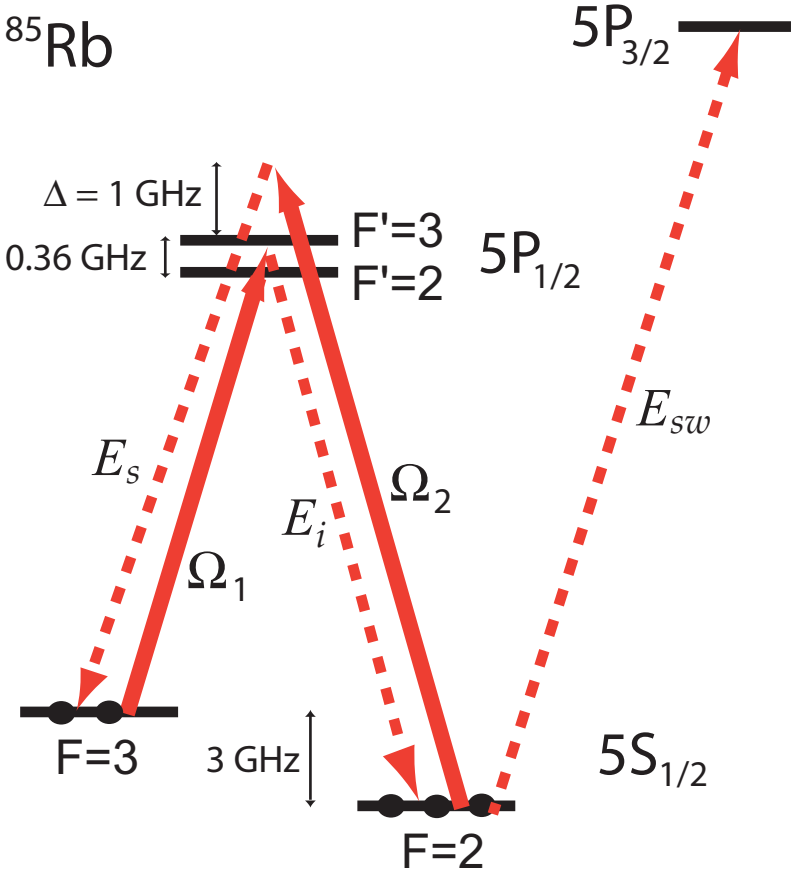

Figure 3.3: Energy-level diagram of the FWM modulation scheme. FWM is generated in a double-lambda configuration on the D_1 ($5S_{1/2} \rightarrow 5P_{1/2}$) transition of ^{85}Rb. It is modulated by periodically turning the switching field E_{sw} on to the D_2 ($5S_{1/2} \rightarrow 5P_{3/2}$) transition. Intensity modulation is imparted as a result on the signal (E_s) and idler (E_i) fields.

degenerate pumps. One pump field Ω_1 is blue detuned by 1 GHz from the $F = 2 \rightarrow F' = 3$ resonance, while the other pump field Ω_2 is tuned between the $F = 3 \rightarrow F' = 2$ and $F = 3 \rightarrow F' = 3$ transitions. A weak signal field E_s blue detuned by 1 GHz from the $F = 3 \rightarrow F' = 3$ transition is also coupled through the PBGF and generates an idler field E_i via the FWM process. The signal is cross-polarized with respect to the pump waves and all three beams are co-propagating in the PBGF. The generated idler is also co-propagating with

the same polarization as the signal. The switching field E_{sw}, which is also cross-polarized with the pumps, is resonant with the $F = 2$ transition of the D_2 line (780 nm) of ^{85}Rb.

3.3 Experimental setup

Figure 3.4 shows the experimental setup. We use a 3-cm-long PBGF (Crystal Fiber AIR-6-800, 6 μm diameter core) that sits inside a vacuum cell with a Rb source attached [65]. The pump beams are combined with the signal and switching beams using a polarization beam splitter (PBS) cube at the input of the PBGF, which ensures that the polarizations are orthogonal. A small portion of each input field is sent to a reference Rb vapor cell for frequency calibration. A pulsed vapor-generation beam at 808 nm (detuned far from the ^{85}Rb resonances), which is coupled counter-propagating to the pump and signal waves, is used to generate the desired vapor density and optical depth in the fiber [66]. The vapor density generated in the fiber is such that in the presence of the pumps (tens of microwatts in power), the signal experiences a gain of 2 at the two-photon resonance (peak of the FWM gain curve). The switching beam is temporally modulated as a triangle wave, at frequencies from 500 Hz - 1 kHz. The modulated signal exits the fiber, is separated from the pumps by a second PBS and from the switching beam by a temperature-controlled etalon (400 MHz linewidth) and is detected by a photo-multiplier tube (PMT).

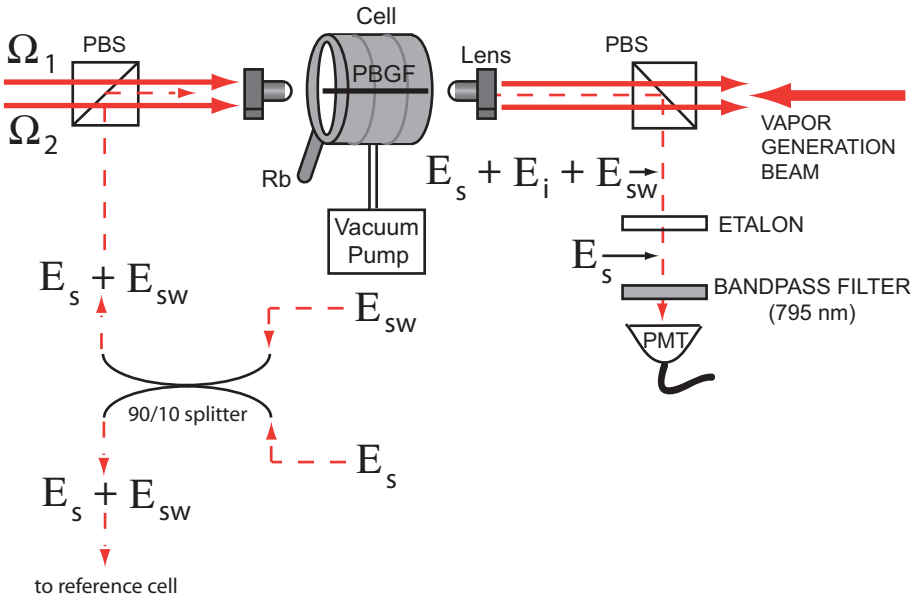

Figure 3.4: Experimental setup for observing all-optical modulation of FWM. The switching and signal fields are combined with the pump fields on a polarizing beam splitter (PBS). The beams are then focused into the core of the fiber. A counter-propagating vapor-generation beam generates the desired vapor density and optical depth. The modulated signal field is filtered from the pump beams by a second PBS and from the idler and switching fields by a temperature-controlled, high-finesse etalon and is then detected with a photo-multiplier tube (PMT).

3.4 Observation of intensity modulation

Figure 3.5 shows the modulated signal at 500 Hz with ~1 μW of peak switching power. The input signal power is 5 nW, and its frequency is set exactly at the two-photon resonance so that at the output of the fiber the signal power is 10 nW. We see that in the presence of the switching field, which is modulated at 500 Hz, the signal is attenuated by 50% (3-dB) to 5 nW. The switching field spoils the gain, and the signal passes through the fiber as if there was no FWM, and the idler field is completely extinguished.

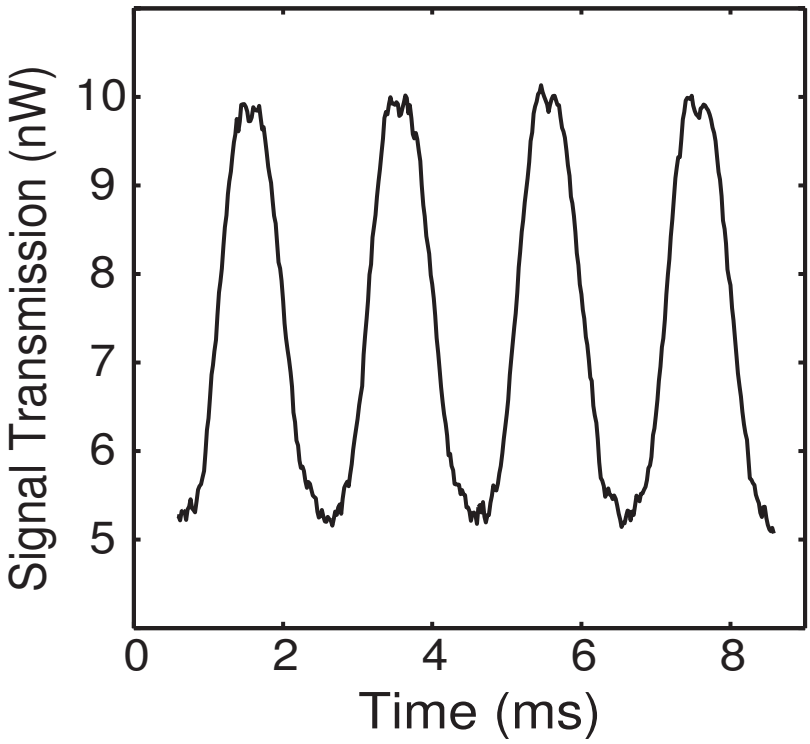

Figure 3.5: All-optical intensity modulation. FWM modulation at 500 Hz with the signal tuned to the two-photon resonance. The 5-nW signal experiences a gain of 2 with 15 μW of total pump power. We observe 3 dB of attenuation in the signal (i.e. extinction of the gain) with 1 μW of switching power. The switching field is on resonance with the D_2 transition.

Figure 3.6 shows the modulation depth observed in the signal as a function of the peak switching power. We find that the modulation depth begins to saturate at 50% for a switching power of 0.65 μW [see dotted line in Fig. 3.6], and increasing the switching power further does not improve the modulation depth.

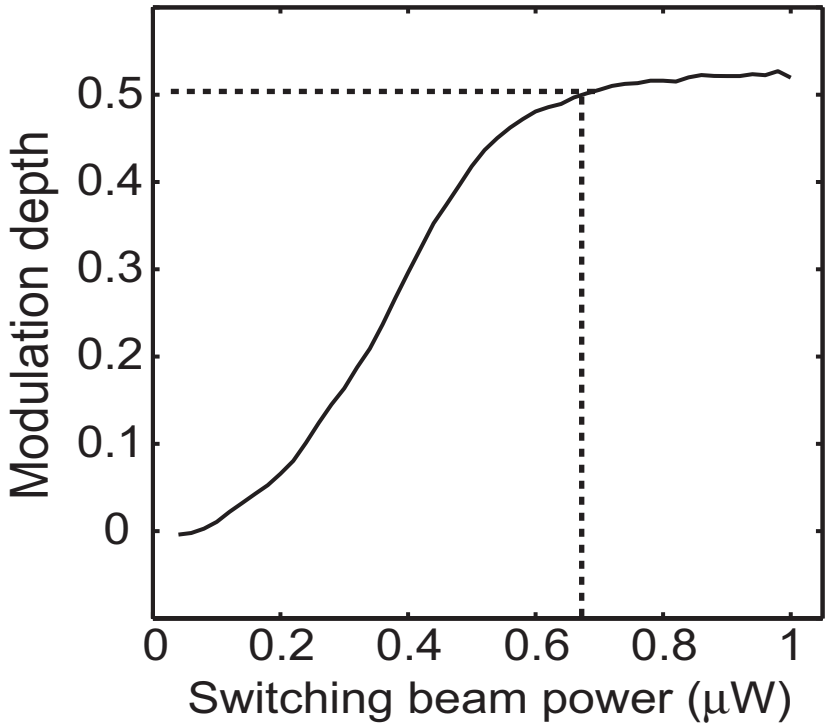

Figure 3.6: Saturation of modulation depth. Signal modulation depth as a function of switching power. Modulation begins to saturate for switching powers $\gtrsim 0.65\,\mu$W.

3.5 Low-light-level switching

A slow scan of the signal frequency about two-photon resonance reveals that the modulation is present over the entire FWM gain bandwidth of ~100 MHz [see Fig. 3.7], which implies a system response time $\tau \sim 1.6$ ns. In this case a weak switching beam (180 nW) was used, revealing both the modulation features as well as the shape of the FWM gain peak. We calculate the effective number of photons interacting within the response time τ of the system for a particular switching power P_{sw} as

$$N_P = \frac{P_{sw}\tau}{hc/\lambda}, \tag{3.2}$$

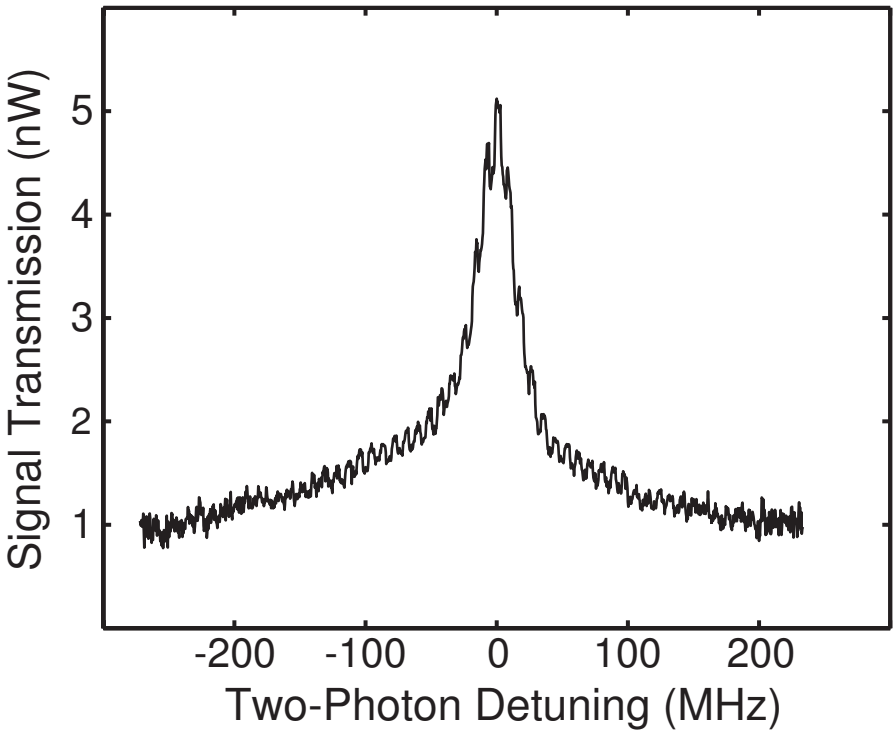

Figure 3.7: Signal gain modulation as a function of two-photon detuning. The FWM is modulated at 2 kHz while the signal is slowly scanned across the gain resonance. The modulation is observed over the full FWM bandwidth of ~100 MHz, implying a response time $\tau \sim 1.6$ ns. The switching beam power is 180 nW.

where hc/λ is the energy of one switching photon, and $\lambda = 780$ nm is the wavelength of the switching beam. Thus, 50% modulation at a switching power $P_{sw} = 0.65\ \mu$W [Fig. 3.6] corresponds to 3600 photons of switching energy. The switching energy density is calculated as

$$\frac{N_P}{A}\left(\frac{\lambda^2}{2\pi}\right), \tag{3.3}$$

where $A \sim 10^{-7}$ cm^2 is the optical mode area. The switching energy density is thus 36 photons per atomic cross-section $\lambda^2/2\pi$.

We interpret these results as the consequence of the population cycling on the D_2 transition that is induced by the switching beam. This spoils the phase

relationship between the ground states and destroys their coherence, which is necessary for performing FWM, within one Rabi cycle. The Rabi frequency corresponding to ~600 nW of switching power on the D_2 line is 120 MHz, i.e. roughly equal to the FWM gain bandwidth. Once there is sufficient power to destroy coherence within the FWM response time, greater switching power no longer increases the amount of modulation, which leads to the saturation behavior seen with respect to switching power.

3.6 Large tunable modulation bandwidths

We also studied the effect of gain/modulation bandwidth B on the modulation depth M for a constant switching field power [see Fig. 3.8]. The FWM gain bandwidth can be modified by changing the relative powers of the two pump fields. In the double lambda scheme used here, the FWM gain coefficient is proportional to the ratio of the Rabi frequency of the off-resonant pump to that of the on-resonant pump, i.e. to Ω_1/Ω_2. Since the gain bandwidth is proportional to the product of the Rabi frequencies of the two pumps i.e. $\Omega_1\Omega_2$ [82, 77], one can modify the gain bandwidth without changing the actual gain by simply changing the relative pump powers such that $\Omega_1\Omega_2$ varies but Ω_1/Ω_2 maintains its value. Based on this idea, we observe gain/modulation bandwidths up to 300 MHz, implying that the system can support 500-ps pulses. It is evident that the modulation depth decreases with increasing bandwidth for a given switching power (blue circles). We can determine the number of switching photons required for 3-dB modulation of the signal field i.e. the switching energy, by calculating the product of the switching power required for 50% modulation (M = 0.5) and the response time of the system (inverse of the bandwidth), for each

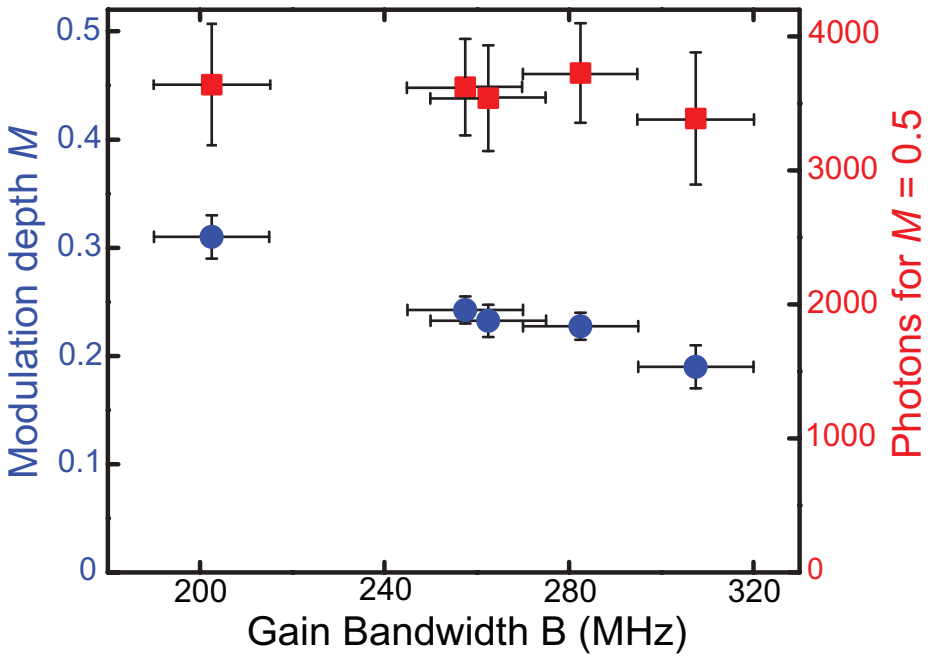

Figure 3.8: Modulation depth and number of switching photons versus FWM bandwidth. The blue circles show the modulation depth observed in the signal field as a function of the FWM gain bandwidth. The switching power used for all the measurements was 400 nW. The red squares show the switching photon number required for 50% modulation of the signal. The switching photon number is observed to be fairly insensitive to bandwidth. Error bars represent measurement inaccuracy.

bandwidth value B. We see that the number of photons required in the switching field is relatively insensitive to the bandwidth (red squares), and the data agree fairly well with the estimated number of 3600 photons.

3.7 Summary and conclusion

In summary, we have observed all-optical modulation of FWM using Rb vapor in a PBGF. We observe 3-dB attenuation of the signal beam using only 3600 photons of switching energy or 36 photons per atomic cross-section $\lambda^2/2\pi$, which is

comparable to that achieved in more elaborate cold atom setups [16, 17]. Moreover, we demonstrate tunable modulation bandwidths up to 300 MHz, which is very high for an alkali vapor interaction. These preliminary results show the potential of an Rb-PBGF system for nonlinear optical interactions at low photon number. For example it should be possible to enhance important alkali-based quantum-optical interactions, such as QND measurement techniques and the production of squeezed states, due to the tight confinement and high optical depths. One limiting factor in our setup currently is the small transit time (~5 ns) of the Rb atoms across the core of the PBGF, which limits the ground state coherence time. Producing a purer state among the ground hyperfine levels by increasing the transit time through collisions with a buffer gas should improve the results [54, 83, 84]. One could also increase the available switching bandwidth by broadening the D_2 transition with the injection of a buffer gas into the system.

In the previous two chapters, a major limiting factor of the Rb-PBGF system in generating ever higher nonlinearities is the inability to optically pump the entire atomic population into one ground state i.e. creating a pure state. As a result, in a highly confined geometry with a small transit-time, only a fraction of the atomic population (~5%) actually contributes to nonlinear optical interactions such as four-wave mixing (FWM) and electromagnetically-induced transparency (EIT). In the next three chapters, we probe the higher-order two-photon transitions of Rb, with the aim of employing them for nonlinear optical interactions involving only one ground state. Such processes benefit from the entire atomic population in a particular ground state without having to create a population difference between the two hyperfine-split ground states, eliminating the need for any optical pumping.

CHAPTER 4

ENHANCEMENT OF TWO-PHOTON ABSORPTION

In this chapter, we show that two-photon absorption (TPA) in Rb atoms can be greatly enhanced by the use of a hollow-core photonic bandgap fiber (PBGF). We investigate off-resonant, degenerate Doppler-free TPA on the $5S_{1/2} \rightarrow 5D_{5/2}$ transition and observe 1% absorption of a pump beam with a total power of only 1 mW in the fiber. These results are verified by measuring the amount of emitted blue fluorescence and are consistent with the theoretical predictions which indicate that transit time effects play an important role in determining the two-photon absorption cross-section in a confined geometry.

4.1 Two-photon absorption

Two-photon absorption (TPA) is the simultaneous absorption of either two photons from a single beam of light or two single photons from two beams which results in a resonant transition from the ground state to an excited state. A key feature of TPA is that it allows access to electronic states that are otherwise dipole-forbidden single-photon transitions. It also represents one of the simplest nonlinear processes that allows one to characterize the strength of the light-matter interaction and to generate novel non-classical effects. As a result, TPA processes have also been widely studied for various nonlinear and quantum optical phenomena, with applications in precision spectroscopy [85], the generation of single photons [27], the measurement of coherence and photon statistics [86], and all-optical switching [28, 87].

For many of the aforementioned applications, a significant amount of TPA is

desired at low power levels. Alkali-metal atoms have large two-photon cross-sections due to the near-resonant enhancement from the intermediate state and the high oscillator strengths of the transitions involved [88, 36]. Nevertheless, previous TPA experiments in bulk alkali-metal vapor cells still required relatively high powers to generate measurable effects [89]. One approach to significantly reduce the threshold for observing TPA is to use waveguide geometries such as hollow-core photonic band-gap fibers (PBGFs) filled with an alkali-metal vapor since it provides tight confinement of the light in a single mode over extended distances, enabling strong light-matter interactions and high nonlinearities at ultra-low power levels [46, 82, 17, 90]. Recently, non-degenerate resonant TPA experiments at nanowatt power levels were performed in tapered optical fibers with ambient thermal rubidium (Rb) vapor, in which the light-matter interaction occurs via the evanescent wave of the guided light in the fiber [91]. It has been shown previously that a Rb-PBGF system can provide large optical depths (ODs) [65]. However, the tight confinement of atoms and photons give rise to additional spectroscopic features such as transit-time broadening which must be taken into account and has been studied previously in our system [68].

Here we describe the experimental observation of efficient, Doppler-free TPA in a Rb-PBGF system using the $5S_{1/2} \rightarrow 5D_{5/2}$ two-photon transition at 778.1 nm at milliwatt power levels. We estimate theoretically the amount of TPA for our system (both from direct absorption from the pump beam and from the emitted blue fluorescence) and show that our experimental results are in good agreement with the theoretical predictions. From our measurements we obtain an estimate of the transit-time of the Rb atoms in the PBGF. We extend our calculations to show how TPA can be further enhanced using a non-degenerate, on-resonance scheme.

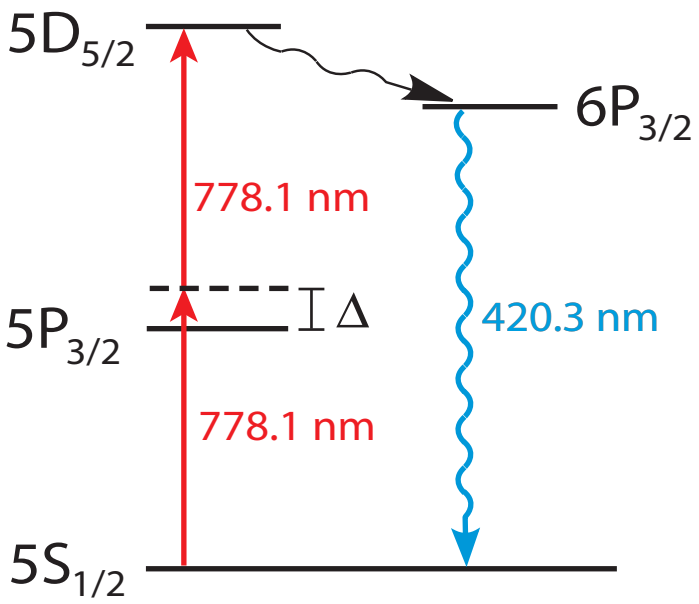

Figure 4.1: Degenerate TPA level scheme in Rb. An atom in the $5S_{1/2}$ ground state can simultaneously absorb two photons at 778.1 nm to make a resonant transition to the $5D_{5/2}$ excited state. Δ is the detuning from the intermediate $5P_{3/2}$ level. A small fraction of the excited atoms decay through the $6P_{3/2}$ level emitting blue fluorescence.

4.2 TPA level scheme

An illustration of the two-photon level scheme we use is shown in Fig. 4.1. An atom in the $5S_{1/2}$ ground state can simultaneously absorb two photons at 778.1 nm to make a resonant transition to the $5D_{5/2}$ excited state. Once excited to the $5D_{5/2}$ level, the Rb atoms decay with 35% probability to the intermediate $6P_{3/2}$ level, and then with 31% probability back to $5S_{1/2}$ ground state emitting blue photons at 420.3 nm [92]. When the pump beam (at 778.1 nm) is far detuned from the intermediate level, or when $\Delta \gg \Gamma$, where Γ is the linewidth of the intermediate level, the process is termed off-resonant two-photon excitation.

4.3 Nonlinear susceptibility and TPA coefficient

We characterize the nonlinearity of the Rb-PBGF system for this process by calculating the imaginary part of the third-order susceptibility $\chi^{(3)}_{Im}$ [40] corresponding to the relevant two-photon transition using,

$$\chi^{(3)}_{Im} = \frac{N\mu_1^2\mu_2^2}{\varepsilon_0\hbar^3\Delta^2\gamma}, \tag{4.1}$$

where N is the atomic number density, μ_1 and μ_2 are the dipole moments for the $5S_{1/2} \rightarrow 5P_{3/2}$ and $5P_{3/2} \rightarrow 5D_{5/2}$ transitions, respectively, Δ is the detuning from the $5P_{3/2}$ level, and γ is the homogeneous decay rate of the $5D_{5/2}$ level. In the Rb-PBGF system, γ is determined by the transit time of the atoms across the micron-scale core of the fiber, which is much smaller than the excited state lifetime [68].

The TPA coefficient is given by [40]

$$\beta\,(cm/W) = 2.82 \times 10^6 \times \left(\frac{2\pi\chi^{(3)}_{Im}}{\lambda}\right), \tag{4.2}$$

where λ is the wavelength of the pump (in cm) and $\chi^{(3)}_{Im}$ (in MKS units) is calculated using equation (4.1). For our system, using an OD $\sim$ 100 ($N \approx 2 \times 10^{13}$ atoms/cm^3), a beam waist area $A \sim 10^{-7}$ cm^2, γ = 50 MHz [68], we estimate the values of $\chi^{(3)}_{Im} \sim 4 \times 10^{-10}$ esu and $\beta \sim 1.3 \times 10^{-6}$ cm/W. Correspondingly, the two-photon scattering cross-section $\sigma^{(2)}$ is estimated to be 6.5×10^{-20} cm^4/W.

4.4 Calculation of two-photon absorption and fluorescence

The transmission of the beam through a medium with a second-order absorption process can be expressed as [40],

$$T = \frac{I_{out}}{I_{in}} = \frac{1}{(1 + \beta I_{in} L)}, \tag{4.3}$$

where I_{in} and I_{out} are the input and output intensities of the pump beam respectively, and L is the interaction length. For $\beta I_{in} L \ll 1$, the percentage of absorption is given by

$$\left[\frac{I_{in} - I_{out}}{I_{in}} = \beta I_{in} L\right] \times 100. \tag{4.4}$$

For 1 mW of power we expect to see 1% absorption in the Rb-PBGF system for a 1-cm interaction length [see Fig. 4.2], which is relatively large for the degenerate off-resonant TPA process at such low pump powers.

To estimate the fluorescence power of the emitted blue light at λ_2 = 420.3 nm, we take into account the branching ratios of the transitions involved during the decay from the excited $5D_{5/2}$ level to the ground $5S_{1/2}$ level, through the intermediate $6P_{3/2}$ level as discussed above. There are two possible decay mechanisms involved in the process. The first is due to a radiative decay from the $5D_{5/2}$ level, which has a lifetime τ_2 of ~240 ns, and the second is due to a non-radiative decay resulting from collisions with the walls of the fiber with a lifetime (transit-time, τ_1) of ~6 ns. Effectively, the fraction of atoms that fluoresces is $\propto \tau_1/(\tau_2 + \tau_1) \approx \tau_1/\tau_2$ [93, 94]. In addition, the decay path from $5D_{5/2} \rightarrow 5S_{1/2}$ (wavelength, λ_1 = 389.05 nm) involves the intermediate level $6P_{3/2}$. Hence we must also take into account the energy lost in the $5D_{5/2} \rightarrow 6P_{3/2}$ transition. Therefore, the total power of the blue fluorescence can be calculated

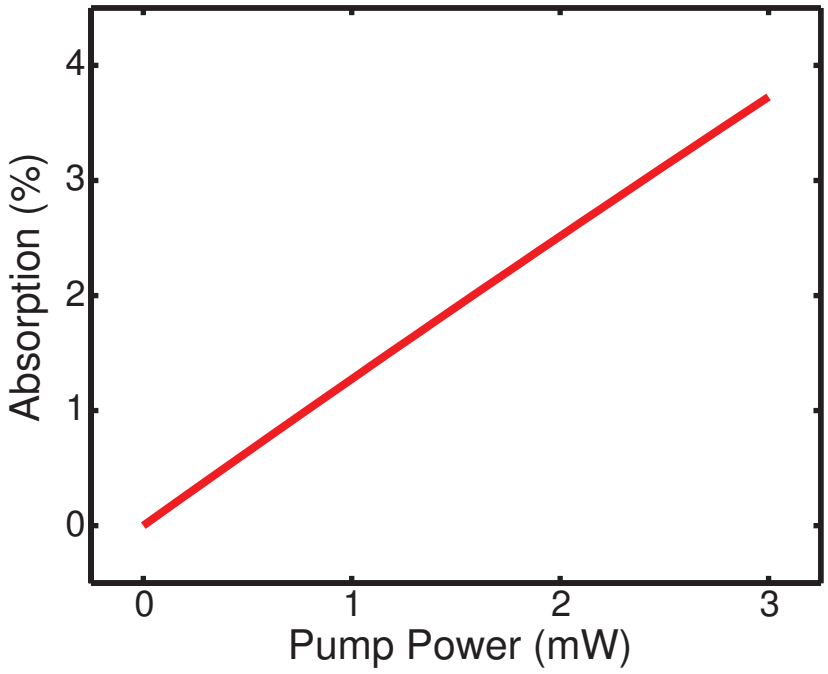

Figure 4.2: Amount of TPA versus pump power for the Rb-PBGF system. An absorption of 1% is estimated for only 1-mW of total pump power. An OD ~ 100 is assumed in the fiber.

from

$$P = (I_{in} - I_{out}) \times A \times R_1 \times R_2 \times \frac{\tau_1}{\tau_2} \times \frac{\lambda_1}{\lambda_2}, \tag{4.5}$$

where $R_1(= 0.35)$ and $R_2(= 0.31)$ are the branching ratios of the $5D_{5/2} \rightarrow 6P_{3/2}$ and $6P_{3/2} \rightarrow 5S_{1/2}$ transitions, respectively. Using equations (4.4) and (4.5) we obtain,

$$P = \{Const\} \times I_{in}^2. \tag{4.6}$$

The resulting quadratic dependence of the blue fluorescence on the pump power is shown in Fig. 4.3.

We perform TPA with counter-propagating beams at 778.1 nm such that TPA occurs by the simultaneous absorption of one photon from each of the beams. The advantage of using a counter-propagating scheme is that the interaction is Doppler free [89, 95, 96]. As the two photons get equal and opposite Doppler

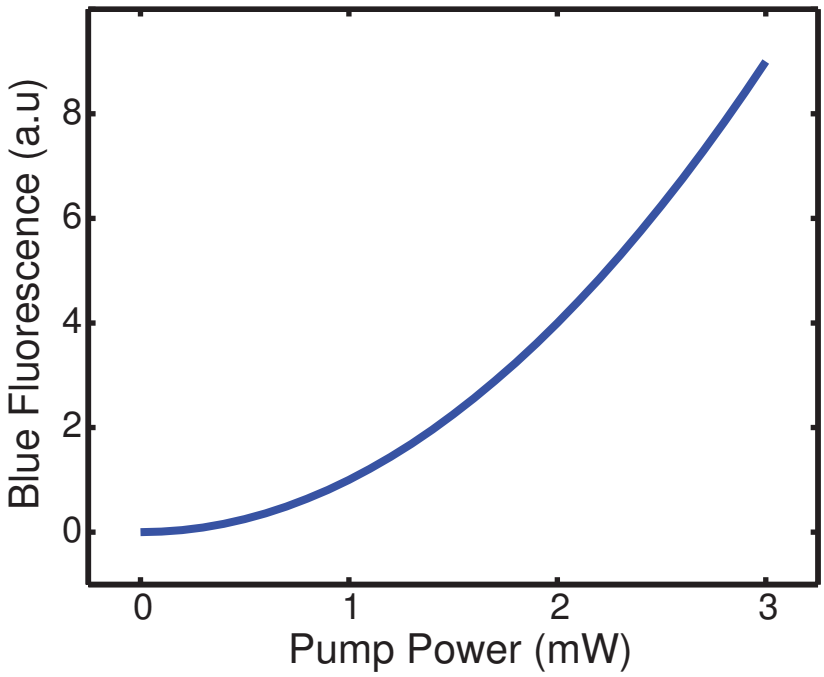

Figure 4.3: Amount of two-photon fluorescence versus pump power for the Rb-PBGF system. The blue fluorescence from Rb atoms due to two-photon excitation increases as the square of the pump power.

shifts for an atom moving at any velocity, their sum always corresponds to the same two-photon transition frequency for all the atoms. Therefore, we expect to see only homogeneously broadened lines due to transit-time effects.

4.5 Experimental setup

We modified the design of the previously used Rb-PBGF system [65] to allow us to image the fibers from the top and collect the emitted blue fluorescence. On one side of the ultra high-vacuum (UHV) compatible stainless steel chamber, we attached a cylindrical glass tube that provides optical access to all sides of the fiber. A schematic of the experimental setup is presented in Fig. 4.4. We use a

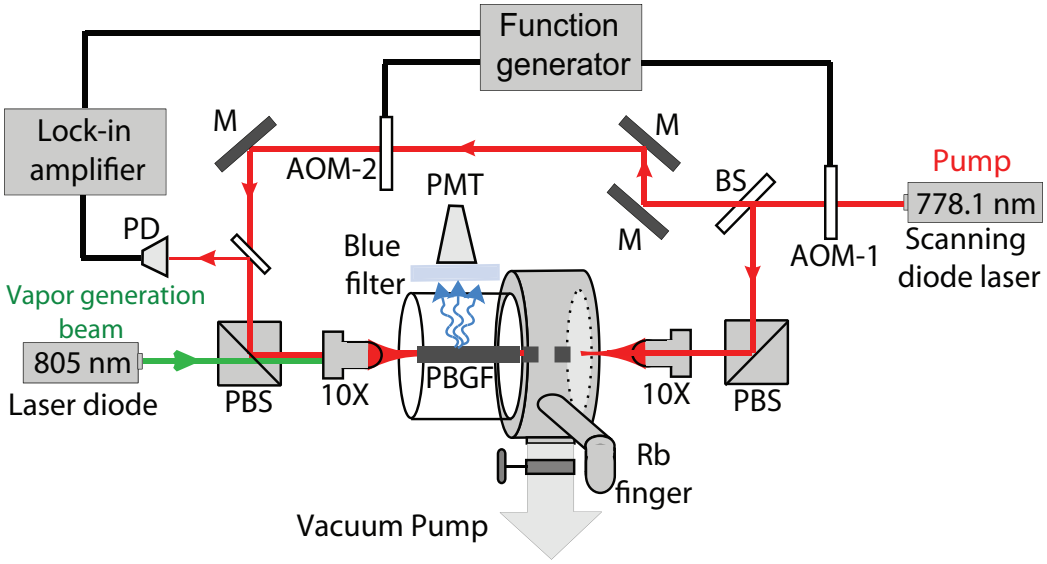

Figure 4.4: Experimental setup for measuring degenerate TPA. The pump laser is split into two counter-propagating beams using a 50:50 beam splitter (BS). The polarizations are made identical using polarization beam splitter (PBS) cubes, and the beams are then coupled through the hollow-core photonic bandgap fiber (PBGF). A strong off-resonant vapor generation beam is also coupled into the fiber to generate the desired atomic density and optical depth. A blue-colored glass is used to filter the fluorescence from the excited $6P_{3/2}$ state and then detected on a photomultiplier tube (PMT). An acousto-optic modulator (AOM-1) is used modulate the pump beams as a triangular wave at a 1-kHz frequency to vary linearly the intensity of the counter-propagating beams simultaneously. For lock-in detection of the TPA through the PBGF, one of the counter-propagating beams is modulated using AOM-2 as a square wave at 25-kHz. The signal is detected on a photodiode (PD) using a pick-off beam at one end and sent to a lock-in amplifier, the output of which is subsequently monitored using an oscilloscope.

9-cm-long and 6-μm-diameter hollow-core PBGF (Crystal Fiber, AIR-6-800) that guides light over the wavelength range of 750-810 nm. The fiber is mounted in a holder designed to hold multiple fibers. The entire fiber mount assembly is placed inside the vacuum chamber with an attached Rb source containing the two naturally occurring isotopes ^{85}Rb (~72%) and ^{87}Rb (~28%). The temperatures of the chamber and the cold-finger (Rb source) are maintained at 85°C and 55°C, respectively and the background pressure after bake-out is 10^{-8} torr. The beam from an external cavity diode laser at 778.1 nm, scanning mode-hop free across 5 GHz (over the two-photon resonances), is split into two counter-propagating beams using a 50:50 beam splitter (BS); these are each coupled to opposite ends of the fiber using 10x objectives. The two beams have equal powers and identical polarizations.

To generate the desired OD (~100), a highly off-resonant 20-mW vapor-generation beam at 805 nm is also coupled into the fiber with a polarization orthogonal with respect to the pump beams. We observe that the vapor is generated in the first 1 cm of the fiber at each ends. The design of our chamber enables us to collect the emitted blue photons from the top at one end. The blue photons are filtered using a blue-colored glass filter and detected by a photo-multiplier tube (PMT; Hamamatsu H7422P-40). The signal is then monitored and recorded for 1-s using an oscilloscope.

We measure the TPA as a function of the intensity of the light field using an acouto-optic modulator (AOM-1) (see Fig. 4.4) to vary the intensity of the two counter-propagating beams simultaneously using a triangular wave at 1 kHz. The emitted blue photons are collected and detected from the top of the fiber by the method described before. For direct measurement of TPA from the 778.1-

nm pump beams, we perform a lock-in detection by using another acousto-optic modulator (AOM-2) to modulate one of the two counter-propagating beams. A weak reflection of the forward propagating beam is collected from one end using a photodiode, its output is then sent to a lock-in amplifier, and the resultant output is then recorded using an oscilloscope.

4.6 Fluorescence measurement

Figure 4.5 shows the blue fluorescence signal detected by the PMT due to TPA. The four peaks correspond to each of the two hyperfine ground states of ^{85}Rb and ^{87}Rb. We recorded the wavelength of each of the lines using a wavemeter (Burleigh WA-1600) with an uncertainty of ±0.0001 nm in each reading. For the states $F = 3$ and $F = 2$ of ^{85}Rb, the wavelengths are 778.1055 nm and 778.1025 nm respectively, where as 778.1067 nm and 778.0997 nm correspond to the $F = 2$ and $F = 1$ states of ^{87}Rb, respectively. The signal is Doppler free, and the line-broadening is due only to the transit-time effect. As discussed earlier, the relatively short transit time of the Rb atoms in comparison to the lifetime of the excited $5D_{5/2}$ level suppresses the number of blue photons emitted, and we estimate the total amount of blue fluorescence emitted from the fiber taking into account the collection area of the PMT and assuming the fluorescence to be isotropic over the 4π solid angle. We obtain 30 nW of blue light for 1 mW of pump power, which corresponds to ~1% absorption [using equations (4.5) and (4.4)]. This agrees very well with the theoretically calculated value.

Figure 4.6 shows the measured blue fluorescence versus input pump power, in which the power of the two counter-propagating pump beams are varied

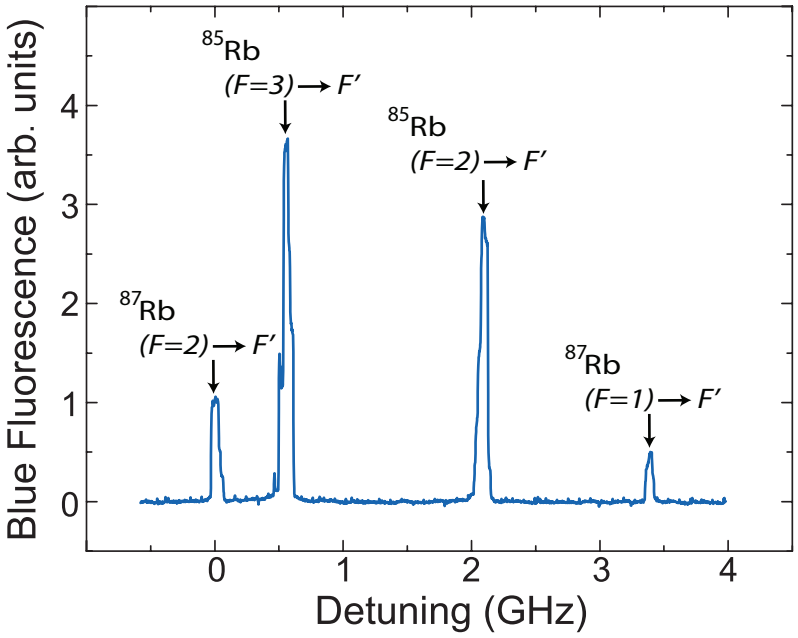

Figure 4.5: Blue fluorescence signal detected by the PMT. Fluorescence peaks corresponding to each of the hyperfine ground states of ^{85}Rb and ^{87}Rb are observed as the pump laser is scanned in frequency. Since the two beams are perfectly counter-propagating in the fiber, all the peaks are Doppler-free. The peaks are homogeneously broadened due to the short transit time (~5 ns) of the Rb atoms across the 6-μm core of the fiber.

from 100 μW to 500 μW using AOM-1. We observe that the blue fluorescence increases quadratically with the intensity of the pump beams, as expected for TPA. We experimentally determine the two-photon cross-section, $\sigma^{(2)}$ to be 5×10^{-20} cm^4/W for the ^{85}Rb $5S_{1/2} \rightarrow 5D_{5/2}$ transition, which agrees with the theoretically calculated value taking into account the short transit-time of the Rb atoms as the dominant decay rate.

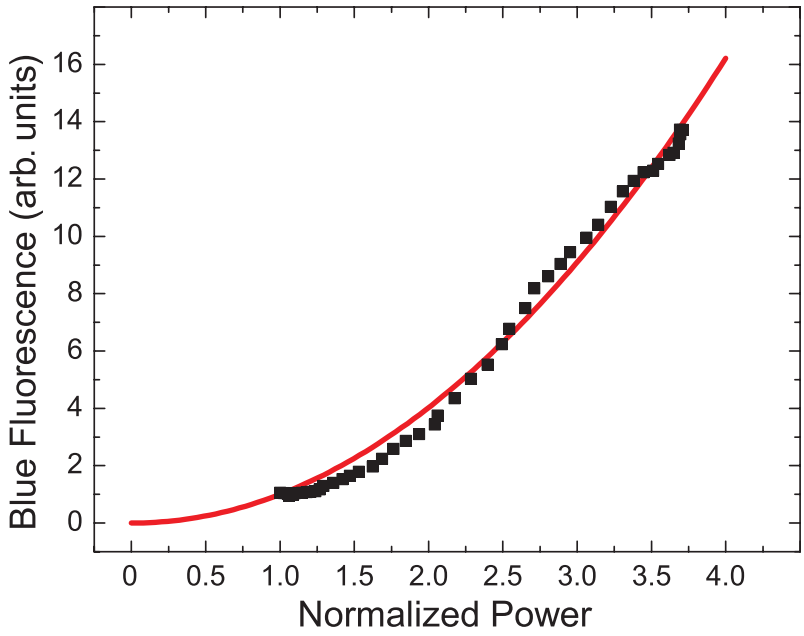

Figure 4.6: Quadratic dependence of two-photon fluorescence on pump power. Blue fluorescence signal (black dots) detected by the PMT as the pump laser power is varied using AOM-1 when the laser is tuned to the $5S_{1/2} \rightarrow 5D_{5/2}$ ($F = 3$ to F') two-photon transition of ^{85}Rb. The solid red line shows the expected square dependence of two-photon absorption on intensity.

4.7 Direct measurement of TPA

Due to the enhanced TPA in Rb-PBGF system, we can directly measure and quantify the amount of absorption from the pump beams. We use a lock-in detection method since the signal-to-noise ratio in our system is low. We use AOM-2 driven by a square wave at 25 kHz to modulate one of the counter-propagating beams. A pick-off beam from the other beam is detected using a photodiode and the output is sent to a lock-in amplifier. Figure 4.7 shows the result of our measurement, and with an input pump power of 1 mW and an OD ~ 100, we observe 1% absorption. This is in good agreement with our estimate of the amount of TPA from the experimental data of blue fluorescence

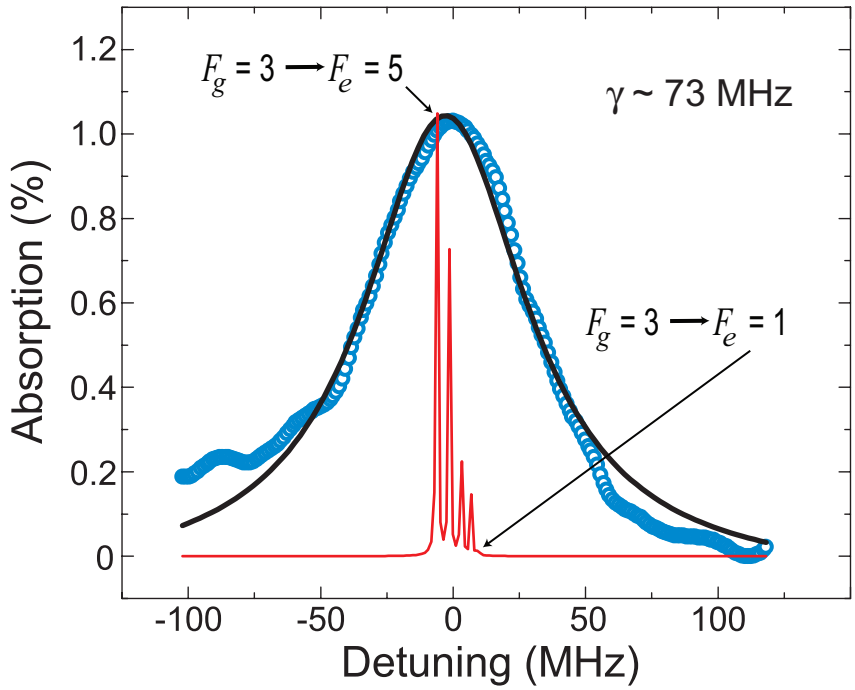

Figure 4.7: Direct measurement of TPA. Circles (blue) show the data from the direct measurement of two-photon absorption from one of the pump beams using a lock-in detector as the pump laser is scanned across the $5S_{1/2} \rightarrow 5D_{5/2}$, F_g=3 to F_e two-photon transition of ^{85}Rb (778.1055 nm). The solid (black) line shows the fit of a sum of five Lorentzians which correspond to each of the hyperfine lines. The homogeneous linewidth is estimated to be 73±10 MHz.

measurement and with our theoretical estimation of TPA.

The absorption lines can also be analyzed to determine the homogeneous linewidth. We fitted a sum of five Lorentzians corresponding to the hyperfine lines (F_g=3 to F_e=1,2,3,4,5) of the $5S_{1/2} \rightarrow 5D_{5/2}$ transition. The estimated linewidth is 73±10 MHz, and represents a direct measurement of the homogeneous linewidth of Rb atoms confined to a hollow-core PBGF. We also note that the homogeneous linewidth (which is determined by transit-time broadening) is slightly different from system (Rb-PBGF) to system [68]. This might be due to the fact that the Rb nanoclusters adsorbed on the inside walls of

the fiber are heated and evaporated at slightly different power levels [66, 67], which results in the corresponding temperatures and therefore the thermal velocities of the Rb vapor being slightly different. Nevertheless, the amount of off-resonance two-photon absorption is substantially high for such low pump powers, which demonstrates the potential of the Rb-PBGF system for exploring novel classical and quantum nonlinear effects at low powers. If we perform an on-resonance non-degenerate TPA [91] with counter-propagating 780.2 nm and 776 nm beams, we theoretically expect to see a 10^8 enhancement over the off-resonance TPA. Such a scheme can be used for all-optical switching at low photon number, and this is investigated in more detail in the next chapter.

4.8 Summary and conclusion

In summary, we demonstrate efficient Doppler-free degenerate TPA in Rb vapor confined to a PBGF. We observed 1% TPA with a 1-mW incident pump power. This represents an enhancement of 4 to 5 orders of magnitude over similar experiments in bulk vapor cells [89, 92, 96]. Further, these results can readily be improved by several orders of magnitude by performing the on-resonance TPA, which will allow for two-photon effects at sub-nanowatt input power levels. We have also been able to measure the transit-time broadening in a more direct manner. Moreover, our system enables us to explore a wide range of ODs and pump intensities in a controllable manner [66]. Accessing TPA resonances in this system shows promise for exploring quantum nonlinear effects at ultralow powers such as single-photon all-optical switching and generation and measurement of non-classical states of light without the usual associated issues of inhomogeneous broadening, linear absorption and spontaneous emission noise.

CHAPTER 5

FEW-PHOTON ALL-OPTICAL INTENSITY MODULATION

In this chapter, we describe the demonstration of 25% all-optical modulation with <20 photons, i.e., a few attojoules of energy, using non-degenerate two-photon absorption in our Rb-PBGF system. An attenuation of up to 3 dB is induced on an optical field with a switching energy density of less than one photon per $(\lambda^2/2\pi)$. We show that the temporal response of the system is determined by the 5-ns transit time of the atoms across the optical mode of the fiber, which results in a modulation bandwidth up to 50 MHz.

5.1 Non-degenerate two-photon absorption

Non-degenerate two-photon absorption (TPA) is the simultaneous absorption of two photons from two different light fields (one from each) and results in a resonant transition from the ground state to an excited state. Many interesting two-photon processes and their applications, such as all-optical switching [87], generation of single photons [27], measurement of coherence and photon statistics [86], and precision spectroscopy [85], require a significant TPA at low power levels. For example, it has been shown that the quantum Zeno effect can be used to implement optical logic gates for classical and quantum computing, where the Zeno effect is produced using a strong TPA medium [28]. Figure 5.1 shows how a TPA medium can be used for all-optical modulation, where a control field induces amplitude modulations on an otherwise transparent signal field. Alkali atoms such as Rb can have relatively large two-photon cross-sections due to near-resonant enhancement and the high oscillator strengths of their transitions. Nevertheless, TPA experiments in bulk alkali vapor cells require rela-

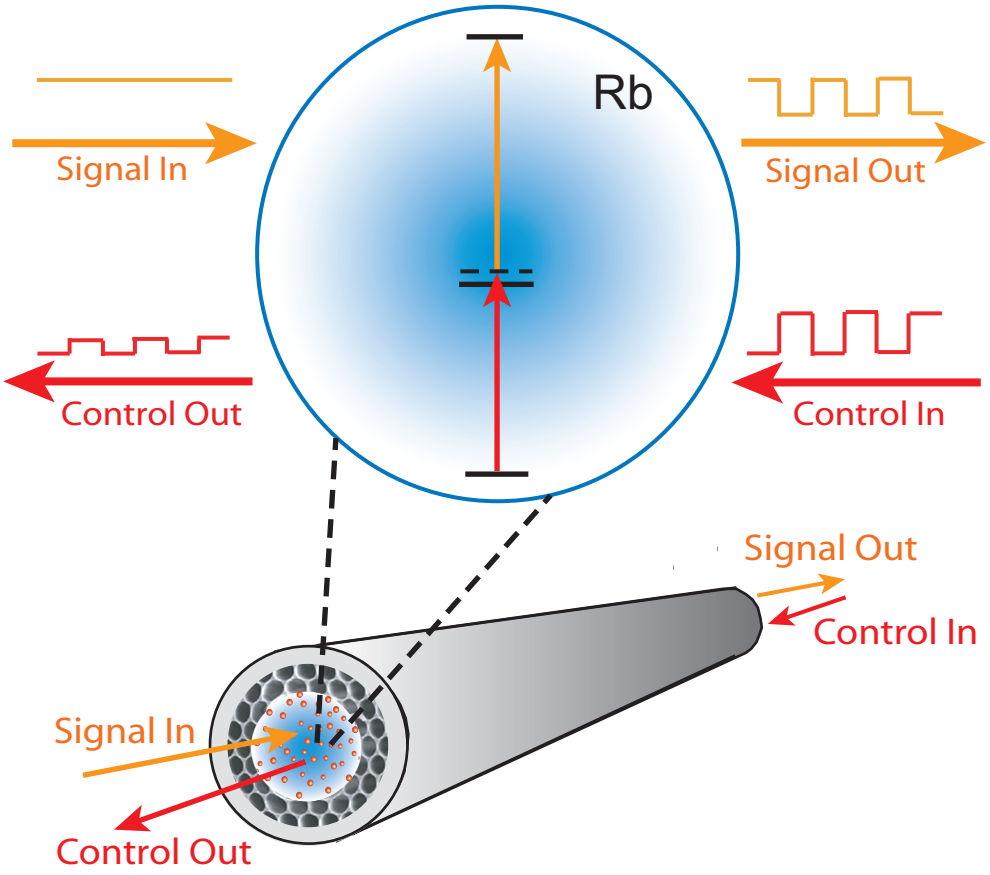

Figure 5.1: All-optical modulation via non-degenerate two-photon absorption (TPA). A control field induces modulations on a continuous wave (CW) signal field while passing through a TPA medium. The atoms in the medium, which could be confined to a waveguiding geometry, undergo TPA when the signal and control fields are both present simultaneously. The signal field, which is transparent to the medium under normal conditions, is attenuated in the presence of the control field.

tively high powers to generate measurable effects [89]. Waveguide geometries, such as hollow-core PBGFs filled with an alkali vapor or tapered optical fibers with an ambient thermal vapour of alkali atoms, can enhance nonlinear interactions greatly and significantly reduce the threshold for observing TPA [97, 91].

Here we describe the observation of large TPA at sub-nanowatt power levels at the ^{85}Rb $5S_{1/2} \rightarrow 5D_{5/2}$ two-photon transition using a near-resonant, non-

degenerate scheme in our Rb-PBGF system. This system demonstrates that as few as 20 photons can induce appreciable all-optical modulation on another beam and that it can be used to explore novel classical and quantum nonlinear effects at ultralow powers. In addition, we measure a fast response time of a few nanoseconds that can yield large modulation bandwidths. Our fiber-based system uses thermal atoms, is relatively simple and easier to control and manipulate than more complicated and elaborate cold atomic clouds [15, 16, 17] and cavity-based setups [41, 42], and holds promise for integration with fiber-optic communication networks [48].

5.2 TPA level scheme

The relevant energy levels of Rb and the two-photon level scheme are shown in Fig. 5.2. An atom in the $5S_{1/2}$ ground state can simultaneously absorb one photon at 780.2 nm (control) and another at 776 nm (signal) to make a resonant transition to the $5D_{5/2}$ excited state. By using a counter-propagating configuration, one can eliminate Doppler broadening in the TPA signal [89]. A small fraction of the excited atoms can decay back to the ground state through the $6P_{3/2}$ level emitting blue fluorescence. In the confined geometry here, most of the excited atoms collide with the walls of the fiber and decay non-radiatively [97].

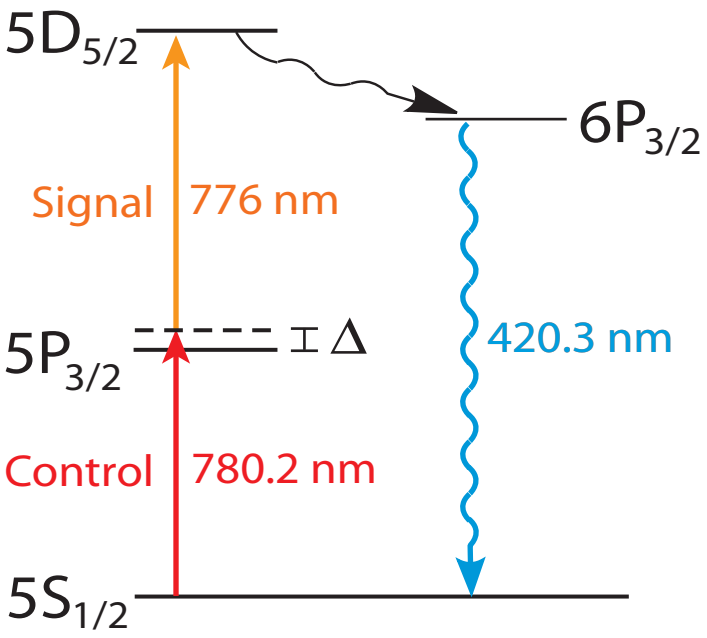

Figure 5.2: TPA level scheme in ^{85}Rb used for performing all-optical modulation. An atom in the ground $5S_{1/2}$ state can simultaneously absorb a photon each from the 780-nm control and 776-nm signal beams to make a resonant transition to the excited $5D_{5/2}$ state. The signal photon can only be absorbed if the control photon is also present. A small fraction of the excited atoms decay through the $6P_{3/2}$ level emitting blue fluorescence.

5.3 Nonlinear susceptibility

The imaginary part of the third-order susceptibility corresponding to TPA [40] is given by

$$\chi^{(3)} \simeq \frac{N\mu_1^2\mu_2^2}{\varepsilon_0\hbar^3\Delta^2\gamma}, \tag{5.1}$$

where N is the atomic number density, μ_1 and μ_2 are the transition dipole moments for the $5S_{1/2} \rightarrow 5P_{3/2}$ and $5P_{3/2} \rightarrow 5D_{5/2}$ transitions, Δ is the detuning from the intermediate $5P_{3/2}$ level, and γ is the homogeneous decay rate from the $5D_{5/2}$ level. In the Rb-PBGF system, γ is determined by the transit time of the atoms across the micron-scale core of the fiber (~5 ns), which is much smaller

than the excited-state lifetime (240 ns) [68, 97]. To maximize TPA, naively one might reduce the detuning from the intermediate level Δ as much as possible to resonantly enhance the interaction. However, since the 780-nm control beam experiences ordinary linear absorption in addition to TPA, the optimal detuning for maximal TPA is non-trivial.

5.4 Calculation of optimum detuning

To theoretically model non-degenerate resonant TPA in a counter-propagating geometry, we numerically solve the following coupled nonlinear propagation equations for the intensities I_C and I_S of the control and signal beams respectively, taking into account the Gaussian velocity distribution of thermal atoms in the fiber,

$$\frac{dI_C}{dz} = -\alpha I_C - \beta I_C I_S, \tag{5.2}$$

$$\frac{dI_S}{dz} = \beta I_C I_S, \tag{5.3}$$

for $0 < z < L$, where L ~1 cm is the sample length, α is the linear absorption coefficient and β is the TPA coefficient. We assume α is given by a Doppler broadened Gaussian absorption profile as

$$\alpha(\Delta) = OD \exp(-\frac{\Delta^2}{w_D^2}), \tag{5.4}$$

where OD is the optical depth on resonance for the $5S_{1/2} \rightarrow 5P_{3/2}$ (D_2) transition, Δ is the detuning of the control beam from line center, and w_D is the Doppler width, which is a function of the temperature of the atoms. For the Rb atoms generated in the hollow core of the PBGF, $w_D \sim 325$ MHz [65]. We compute an average β for a particular detuning Δ by integrating over the Gaussian velocity

distribution of thermal atoms in the fiber. For an atom moving at velocity v, the two-photon cross-section [40] at detuning Δ is

$$\sigma^{(2)}(\Delta, v) = \frac{\mu_1^2 \mu_2^2}{\varepsilon_0 \hbar^3 \gamma((\Delta - kv)^2 + \gamma^2)}, \tag{5.5}$$

where $k = 2\pi/\lambda$ is the wavenumber. The average β is computed by integrating over the thermal velocity profile as

$$\beta(\Delta) = N \int_{-\infty}^{+\infty} \sigma^{(2)}(\Delta, v) f(v) dv, \tag{5.6}$$

where

$$f(v) = \frac{1}{\sqrt{2\pi} v_D} \exp(-\frac{v^2}{v_D^2}), \tag{5.7}$$

is the thermal velocity distribution, $v_D = w_D/k$ and N is the atomic density.

We thus compute both the linear [$\alpha(\Delta)$] and two-photon [$\beta(\Delta)$] absorption coefficients for a particular detuning Δ and then numerically simulate the non-linear propagation equations (5.2) and (5.3) to calculate the amount of TPA expected at that detuning. Figure 5.3 shows the calculated TPA as a function of the detuning from the intermediate $5P_{3/2}$ level for an OD = 100. It is evident that maximum TPA is expected at $\Delta \sim 600$ MHz and going closer to resonance is deleterious because of the dominance of the linear absorption of the 780-nm control beam over the TPA process. Our experimental observation is consistent with this theoretical prediction.

5.5 TPA coefficient and its dependence on atomic density

For the Rb-PBGF system, using an OD ~100 which corresponds to an atomic density $N = 2 \times 10^{13}$ atoms/cm^3 and a homogeneous decay rate $\gamma \sim 50$ MHz due

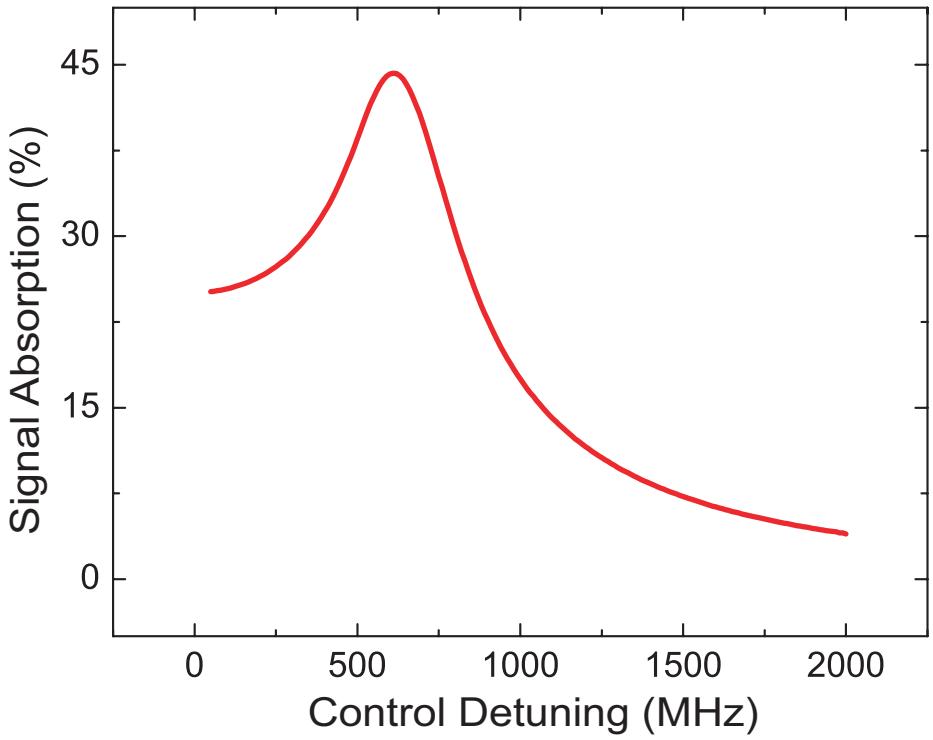

Figure 5.3: Optimum detuning for non-degenerate TPA. Absorption of the signal beam at two-photon resonance with varying detuning of the control beam from the intermediate $5P_{3/2}$ level.

to transit-time broadening [68], we estimate an effective TPA coefficient β = 50 cm/W. We also studied the dependence of TPA on the atomic density/optical depth (OD). From the simulation of equations (5.2) and (5.3), we conclude that the ratio β/α plays a critical role in determining the amount of TPA in this system. Figure 5.4 plots the TPA at different optical depths for a fixed Δ = 600 MHz. The amount of TPA for a specified amount of optical power is found to first increase with OD but then saturate for OD $\gtrsim$100; increasing the atomic number further has no effect. We confirm this by measuring TPA at different optical depths and observing that it is nearly independent of OD, which is consistent with the theoretical prediction since β/α is independent of OD and atomic density.

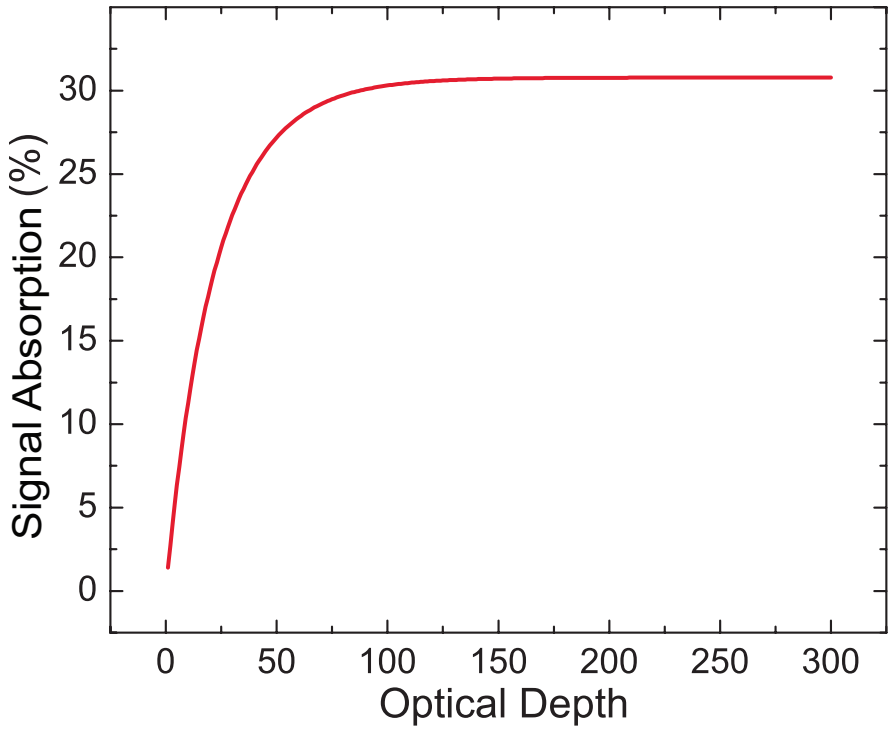

Figure 5.4: Dependence of TPA on optical depth. Absorption of the signal beam at two-photon resonance with varying atomic density.

5.6 Experimental setup

The experimental setup is shown in Fig. 5.5. Hollow-core PBGFs (Crystal Fiber AIR-6-800) are mounted inside a vacuum chamber with a Rb source attached. The fiber has a 6-μm diameter hollow core and guides light in the 750-810 nm wavelength range with a fundamental mode area given by 10^{-7} cm^2. The signal and control beams (at 776 nm and 780.2 nm) have identical circular polarizations and are coupled counter-propagating into the core of the fiber to eliminate Doppler broadening. The 776-nm laser is scanned across the TPA resonances while the 780-nm laser is tuned near the D_2 line of ^{85}Rb. Every Rb atom can simultaneously absorb one photon from each of the two counter-propagating beams, thus eliminating Doppler broadening. A 3-mW highly non-resonant va-

por generation beam at 805 nm with orthogonal polarization to the pump beams is also coupled into the fiber to evaporate Rb nanoclusters adsorbed on the inside walls of the core [66, 67], and to generate a high OD ~100. The OD generated is continuously monitored during the experiment using another laser at 795 nm scanning across the Rb D_1 line. This low power beam scans across a different hyperfine transition, $5S_{1/2} \rightarrow 5P_{1/2}$ ($F = 2 \rightarrow F'$), and does not interfere with the TPA process. A pick-off is used to directly measure the absorption from the 776-nm pump beam after it exits the fiber using a sensitive photodetector. In addition, for pulsed measurements, an electro-optic amplitude modulator driven by a function/waveform generator is used to make square pulses of varying duration (5 - 200 ns) from the 776-nm signal beam. The time period of the pulse train is kept at least 5 times the pulse width for each measurement. The peak power in the signal beam pulses is kept the same (5 nW) for each measurement run. The 776-nm laser is also slowly scanned in frequency across the TPA resonance, so that there are many pulses for each detuning. The 780-nm control beam is kept CW and at the same power (5 nW) for all the measurements. The average power of the signal beam after exiting the PBGF is measured using a sensitive but slow detector, and the amount of absorption induced at two-photon resonance is deduced. This procedure is repeated for each different value of the pulse width.

5.7 Observation of ultralow power TPA

Figure 5.6 shows the transmission of the signal beam as it was scanned across the $5P_{3/2} \rightarrow 5D_{5/2}$ line of ^{85}Rb. The control beam was tuned to a frequency 600 MHz to the blue of the $5S_{1/2} \rightarrow 5P_{3/2}$ ($F = 3 \rightarrow F' = 4$) transition. This detun-

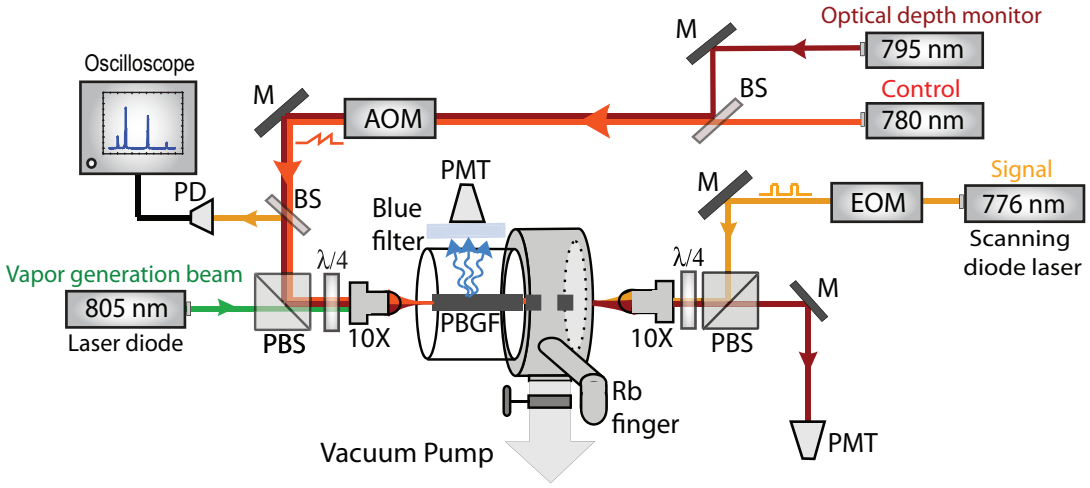

Figure 5.5: Experimental setup for few-photon all-optical modulation. The polarizations of the signal and control beams are made identical (circular) using polarization beam splitter (PBS) cubes and quarter ($\lambda/4$) waveplates, and the beams are then coupled counter-propagating into the fiber. A pick-off is used to monitor the transmission of the signal beam using a sensitive photodetector (PD). A strong (3 mW) off-resonant vapor generation beam is also coupled into the fiber to generate the desired atomic density and optical depth. The optical depth is monitored during the experiment using a weak 795-nm beam scanning across the D_1 resonance of Rb. An electro-optic modulator (EOM) driven by a function/waveform generator is used to make square pulses from the signal beam for the pulsed measurement shown in Fig. 5.7. An acousto-optic modulator (AOM) driven by another function generator is used to ramp the power of the control beam as a sawtooth wave for the measurement shown in Fig. 5.8.

ing was observed to give the maximum TPA, as expected from our theoretical calculation, and tuning closer to resonance decreased the effect due to linear absorption of the control beam. We observed 25% absorption with less than 2 nW of total power in the fiber. The powers in the signal and control beams were 600 pW and 825 pW, respectively. A transit-time limited transmission profile is of the form

$$T(\omega) = 1 - A\exp(-\tau|\omega|), \tag{5.8}$$

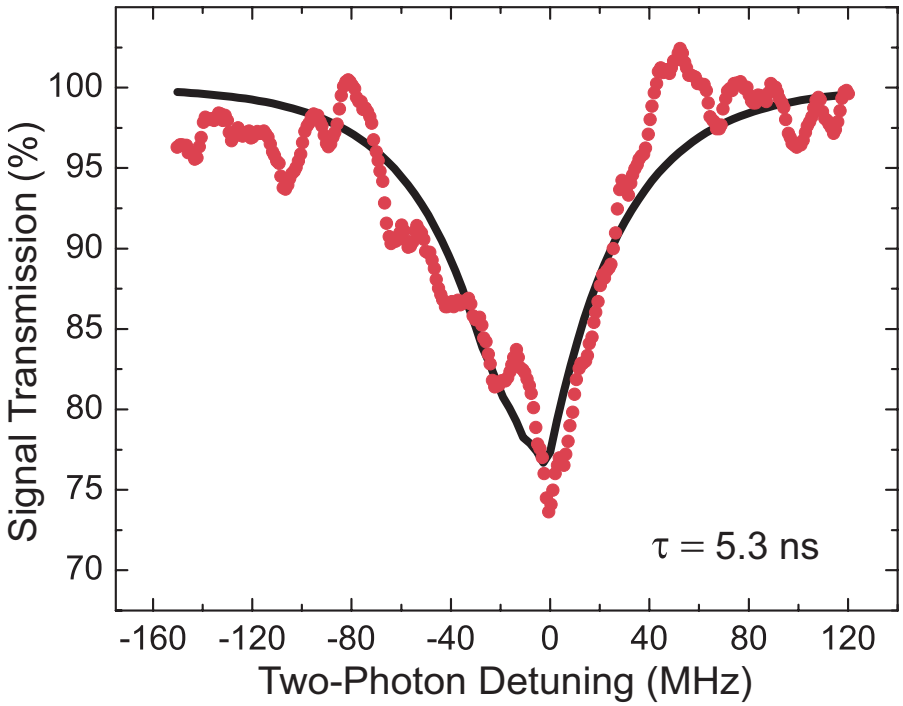

Figure 5.6: Ultralow power TPA. Transmission (red dots) of the signal beam as it is scanned across two-photon resonance showing 25% absorption with 1.4 nW of total power in the fiber. The powers in the signal and control beams are 600 pW and 825 pW, respectively. The control beam is tuned 600 MHz from the $5S_{1/2} \rightarrow 5P_{3/2}$ ($F = 3 \rightarrow F' = 4$) transition. The OD attained in the fiber is ~200. The Doppler-free lineshape is homogeneously broadened due to the short transit time of the Rb atoms across the fiber core. The solid black line shows a fit produced by summing five exponential lineshapes corresponding to the accessible hyperfine states of $5D_{5/2}$ level, from which the transit time τ was determined to be 5.3 ns.

where ω is the detuning from two-photon resonance and τ is the transit-time [98]. We fit the data in Fig. 5.6 to a sum of five exponential functions corresponding to the hyperfine states ($F' = 1, 2, 3, 4, 5$) of the excited $5D_{5/2}$ level in ^{85}Rb and extract the transit-time to be 5.3 ns. This agrees very well with our previous measurement of the transit-time in a Rb-PBGF system [68, 97]. We also extract the TPA cross-section $\sigma^{(2)}$ to be 5×10^{-12} cm^4/W, which agrees with the theoretically calculated value taking into account the transit time of the Rb

atoms as the dominant decay rate and averaging over the Doppler profile.

5.8 Response time and modulation bandwidth

In order to confirm that the response time of our system is comparable to the transit time, we set up a pulsed measurement. An electro-optic modulator (EOM) is used to amplitude modulate the signal beam [see Fig. 5.5] and make square pulses of varying duration (from 5 - 200 ns), and the TPA is measured for each pulse width. The powers in the two beams were kept 5-10 times higher than in the previous CW measurement to improve the signal-to-noise ratio. The TPA is found to reduce with decreasing pulse width, with a profile as shown in Fig. 5.7.

We also theoretically calculate the absorption for each pulse width by averaging the homogeneously broadened absorption profile over the pulse bandwidth. A transit time limited absorption profile is given by $A(\omega) = A_0 e^{-\tau|\omega|}$, where ω is the detuning from two-photon resonance and τ is the transit-time [98]. The absorption A_0, at two-photon resonance, is determined from the numerical simulation of the nonlinear propagation equations (5.2) and (5.3), for a specific set of signal and control beam powers and optical depth. The power spectrum of a square pulse of duration T is given by [99],

$$F(T,\omega) = N_0 sinc^2\left(\frac{\omega T}{2\pi}\right), \tag{5.9}$$

where $sinc(x) = \sin(\pi x)/(\pi x)$, and N_0 is a normalization constant such that $\int_{-\infty}^{+\infty} F(T,\omega)d\omega = 1$. For a pulse of duration T, the effective TPA at two-photon

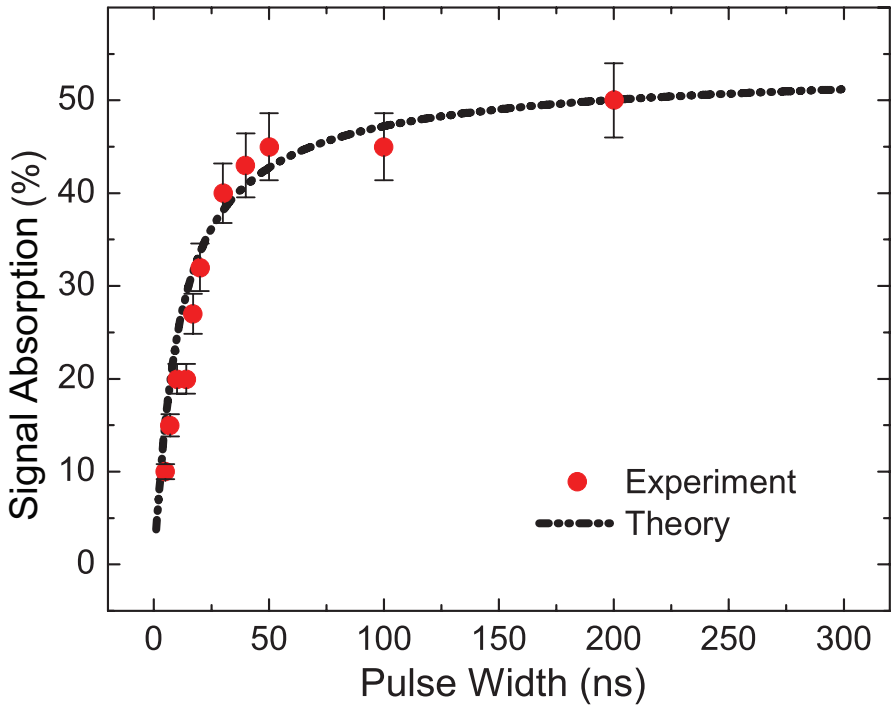

Figure 5.7: Pulsed TPA measurement. Absorption (red dots) of the pulsed signal beam at two-photon resonance versus pulse width. Error bars indicate measurement noise (one standard deviation). An amplitude modulator is used to create square pulses of varying duration (from 5 - 200 ns) from the signal beam, and the TPA is measured for each pulse width. The peak power in the signal pulses is kept the same (5 nW) for each measurement run. The control beam is kept CW and at the same power (5 nW) for all the measurements. The experimental data agree very well with the theoretically predicted curve (dotted black line) for a transit time τ = 5 ns of the Rb atoms across the fiber core and corroborates that the response time of the system is determined by the transit time.

resonance is calculated as

$$A(T) = \int_{-\infty}^{+\infty} F(T,\omega)A(\omega)d\omega, \tag{5.10}$$

In Fig. 5.7, the dotted black line plots $A(T)$ for T varying from 1 - 300 ns with no additional fitting parameters. The experimental data agree very well with the theoretically predicted curve for a transit time τ = 5 ns. As there are no

fitting parameters in the theory curve, the pulsed measurement concurs with the CW linewidth measurement to confirm the response time of our system as 5 ns. Modulation bandwidths up to 50 MHz are thus possible even with this sensitive scheme.

5.9 Few-photon switching

We calculate the effective number of photons interacting within the response time τ of the system for a particular power P as

$$N_P = \frac{P\tau}{hc/\lambda}, \tag{5.11}$$

where hc/λ is the energy of one photon. Thus, for P = 600 pW and λ = 776 nm, $N_P \sim 12$, and for P = 825 pW and λ = 780 nm, $N_P \sim 16$. This implies on average only 12 and 16 photons in the signal and control beams, respectively, are interacting with the atoms within the transit time, for the 25% modulation shown in Fig. 5.6. The switching energy is $N_P hc/\lambda$, which for the 780-nm control beam corresponds to ~5 aJ.

Finally, we measured the attenuation induced on the CW signal beam with varying power of the control beam at two-photon resonance. An acousto-optic modulator (AOM) is used to amplitude modulate the control beam [see Fig. 5.5] and ramp its power as a sawtooth wave. Figure 5.8 shows the data for one continuous ramp. The switching energy density is calculated as

$$\frac{N_P}{A}\left(\frac{\lambda^2}{2\pi}\right), \tag{5.12}$$

where $A \sim 10^{-7}$ cm^2 is the optical mode area. We observe larger attenuation in the signal beam with higher control beam power, and up to 3 dB attenuation is

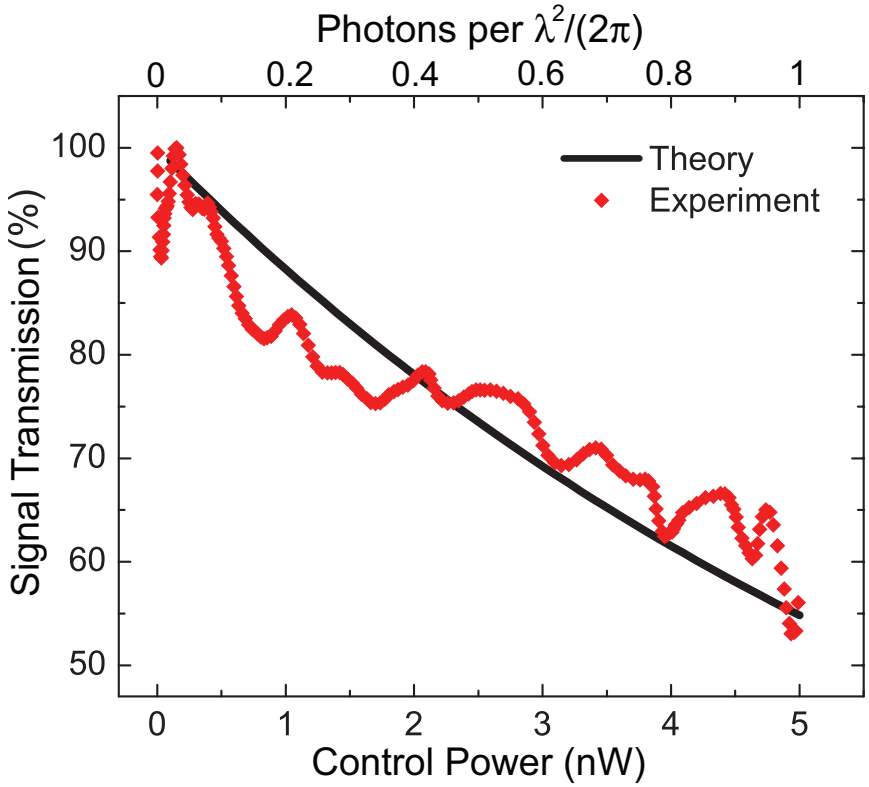

Figure 5.8: Dependence of modulation depth on control beam power. Transmission (red dots) of the signal beam at two-photon resonance with varying power in the control beam. An amplitude modulator ramps the power of the control beam as a sawtooth wave. The data are shown for one continuous ramp. Up to ~3 dB attenuation in the signal beam is observed with less than 5-nW of control power which corresponds to an energy density less than one photon per $(\lambda^2/2\pi)$. The solid black line shows the theoretical prediction from numerical simulation of the nonlinear propagation equations.

achieved with less than 5-nW power, which corresponds to an energy density of less than one photon per $(\lambda^2/2\pi)$. The experimental data match the theoretical trend reasonably well.

5.10 Summary and conclusion

In summary, we demonstrate few-photon all-optical modulation using non-degenerate TPA in thermal Rb atoms confined to a hollow core PBGF. We show 25% attenuation of a signal beam with a switching energy of only 5 attojoules, corresponding to about 16 photons. The switching energy density is less than one photon per atomic cross-section. We also characterize the time response of the system to be 5 ns, which enables large modulation bandwidths up to 50 MHz for a highly sensitive atomic vapour-based scheme. Our results compare favourably with those achieved in previous experiments, including more elaborate and complicated cold atom setups [14, 15, 16, 17]. Moreover, our system enables us to explore a wide space of atomic density and optical intensity in a controllable manner and holds promise for integration with fiber-optic communication networks [48]. These results show the potential of a Rb-PBGF system for exploring quantum nonlinear effects at ultralow powers such as single-photon all optical switching, generation and measurement of non-classical states of light and accessing higher-order nonlinear susceptibilities.

CHAPTER 6

CROSS-PHASE MODULATION AT THE FEW-PHOTON LEVEL

In this chapter, we describe the production of relatively large cross-phase shifts (XPS) on a meter beam with <20 signal photons using our Rb-PBGF system. Through use of a non-degenerate near-resonant two-photon transition, an XPS of ~0.3 milliradian per signal photon with a fast response time of <5-ns is induced in our system. This represents, to our knowledge, the largest such nonlinear phase shift induced in a single-pass through a room-temperature medium. Our system can thus potentially be employed to realize weak-nonlinearity based quantum computation and quantum non-demolition measurement of photon number.

6.1 Cross-phase modulation for quantum computing

Large cross-phase modulation (XPM) near the single-photon level [100, 101], where one light field induces a nonlinear phase shift on another light field, is desired for many quantum information applications. The ability to measure properties of a light field without destroying it is a key requirement of many quantum communication and computation protocols. A medium with large third-order nonlinearity can be employed for QND measurement via the optical Kerr effect [29]. A meter wave propagating through the medium gets a nonlinear optical phase shift (XPS) proportional to the intensity of a signal wave. By measuring the phase of the meter at the output the signal intensity, or photon number, can be determined. It was proposed that an exceptionally strong Kerr medium, such that a single-photon in the signal causes a π-radian phase shift of the meter, can be used to build universal gates [30] and perform all-

optical quantum computing [32]. Although atomic vapor based schemes using electromagentically-induced transparency (EIT) have been proposed as possible candidates to realize such quantum phase gates [11, 102], fundamental doubts have been raised to the feasibility of a single-photon π-phase shift [33, 103]. A new paradigm for quantum computation has recently been proposed based on weak-nonlinearities, where a strong coherent light field mediates interactions between photons [34, 104]. This is a unified approach to quantum communication and computation, employing QND measurements of photons and robust distribution of quantum information through intense laser fields. Such a protocol may be more feasible in terms of practical resources and the potential for scalability to many qubits. Weak-nonlinearities can be exploited to build photon-number resolving QND detectors [29, 105], and when coupled with homodyne measurements and classical feed-forward elements, can be used to construct nearly deterministic controlled-NOT (cNOT) gates [106] and non-destructive Bell state detectors [107]. An XPS of 10^{-5} to 10^{-2} radians per photon is typically desired to make these schemes feasible [34, 104, 105, 106, 107]. For comparison, an XPS of 10^{-7} radians per photon was measured recently using a nonlinear photonic crystal fiber [21].

Previous experiments exploring large XPM in atomic vapors have mainly employed EIT-based schemes [35, 108, 109, 110], where the signal field spectrum has to fit within the narrow EIT transmission window, resulting in timescales >1 μs. Although these schemes provide large values of the nonlinear susceptibility, large optical mode areas have limited the XPSs achieved to ~10^{-6} radians per photon. Here we describe the observation of large XPM (> 10^{-3} radians with <20 photons) at the ^{85}Rb $5S_{1/2} \rightarrow 5D_{5/2}$ two-photon transition using a near-resonant, non-degenerate, 3-level scheme [23, 111] in our Rb-PBGF system. We produce

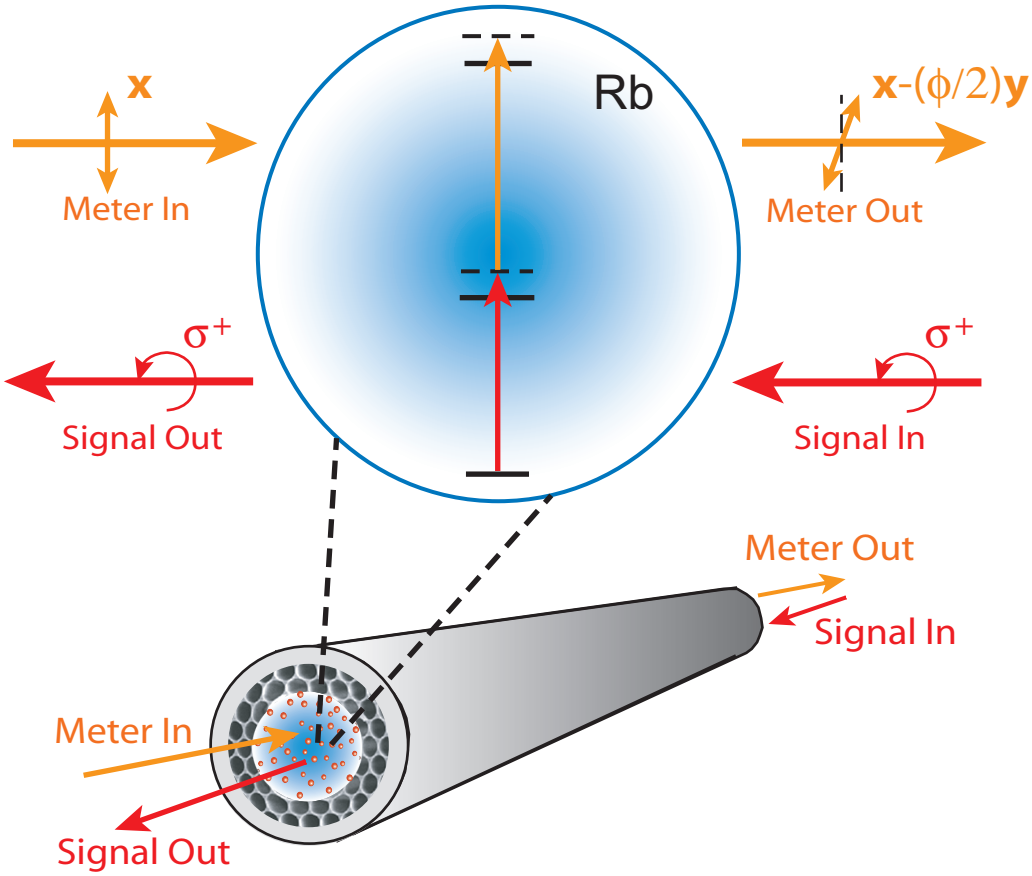

Figure 6.1: Cross-phase modulation (XPM) using a two-photon, 3-level scheme in Rb vapor confined to a hollow core PBGF. A weak circularly-polarized signal field induces a nonlinear phase shift ϕ on a linearly-polarized meter field while passing through a medium of Rb atoms confined to a PBGF. Due to the selection rules of the two-photon transition used, the meter field acquires a slight polarization rotation proportional to the intensity of the signal beam.

large phase shifts of 0.3 milliradian per photon at relatively fast response times of a few nanoseconds which can yield much larger phase modulation bandwidths as compared to other atomic vapor based setups [35, 108, 109, 110]. Our fiber-based system uses thermal atoms at room temperature, is relatively simple and easier to control and manipulate than more complicated and elaborate cold atomic clouds [15, 16, 35, 109, 110] and cavity-based setups [100, 101], and holds

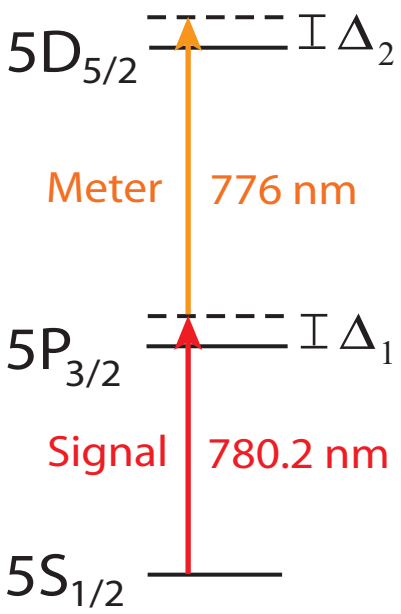

Figure 6.2: 3-level scheme in ^{85}Rb used for performing cross-phase modulation. A weak signal beam tuned close to the $5S_{1/2} \rightarrow 5P_{3/2}$ transition imparts a phase shift on a strong meter beam on the $5P_{3/2} \rightarrow 5D_{5/2}$ transition through a cross-Kerr ($\chi^{(3)}$) interaction.

promise for integration with fiber-optic communication networks [48].

6.2 3-level scheme and nonlinear susceptibility

The energy level scheme in ^{85}Rb used to perform XPM is shown in Fig. 6.2. A weak signal beam (780.2 nm) tuned close to the $5S_{1/2} \rightarrow 5P_{3/2}$ transition induces XPS on a stronger meter beam (776 nm) tuned to the $5P_{3/2} \rightarrow 5D_{5/2}$ transition due to the third-order Kerr nonlinearity. Since the entire atomic population is in the ground $5S_{1/2}$ state, the meter beam (tuned to the upper transition) does not experience any self-phase modulation. The real part of the third-order susceptibility corresponding to XPM [40] is given by

$$\chi^{(3)} \simeq \frac{N\mu_1^2\mu_2^2}{\varepsilon_0\hbar^3\Delta_1^2\Delta_2}, \tag{6.1}$$

where N is the atomic number density, μ_1 and μ_2 are the transition dipole moments for the $5S_{1/2} \rightarrow 5P_{3/2}$ and $5P_{3/2} \rightarrow 5D_{5/2}$ transitions, respectively, Δ_1 is the signal detuning from the intermediate $5P_{3/2}$ level, and Δ_2 is the two-photon detuning. The second-order index of refraction is related to the third-order susceptibility as

$$n_2\left(cm^2/W\right) = \left(2.82 \times 10^6\right)\chi^{(3)}, \tag{6.2}$$

where $\chi^{(3)}$ (in MKS units) is calculated using equation (6.1).

To maximize XPM, naively one might reduce the detunings Δ_1 and Δ_2 as much as possible to resonantly enhance the interaction. However, it is necessary to have $\Delta_2 >> \gamma$ to minimize loss due to two-photon absorption (TPA), where $\gamma \sim 50$ MHz is the TPA linewidth previously measured in our system [112]. Moreover, since the 780-nm signal beam experiences ordinary linear absorption, the optimal detuning Δ_1 is non-trivial.

6.3 Calculation of optimum detuning

The XPS induced on the meter beam, ϕ, for a given signal beam power, P_S, is given by

$$\phi = 2k_M n_2 P_S \frac{L_{eff}}{A}, \tag{6.3}$$

where n_2 is the second-order index of refraction, $k_M = 2\pi/\lambda_M$ is the wave-number of the meter, $\lambda_M = 776$ nm is the wavelength of the meter, L_{eff} is the effective interaction length and $A \sim 10^{-7}$ cm^2 is the optical mode area. The XPS thus scales linearly with signal power. The effective interaction length is given by

$$L_{eff} = \frac{1 - \exp(\alpha L)}{\alpha}, \tag{6.4}$$

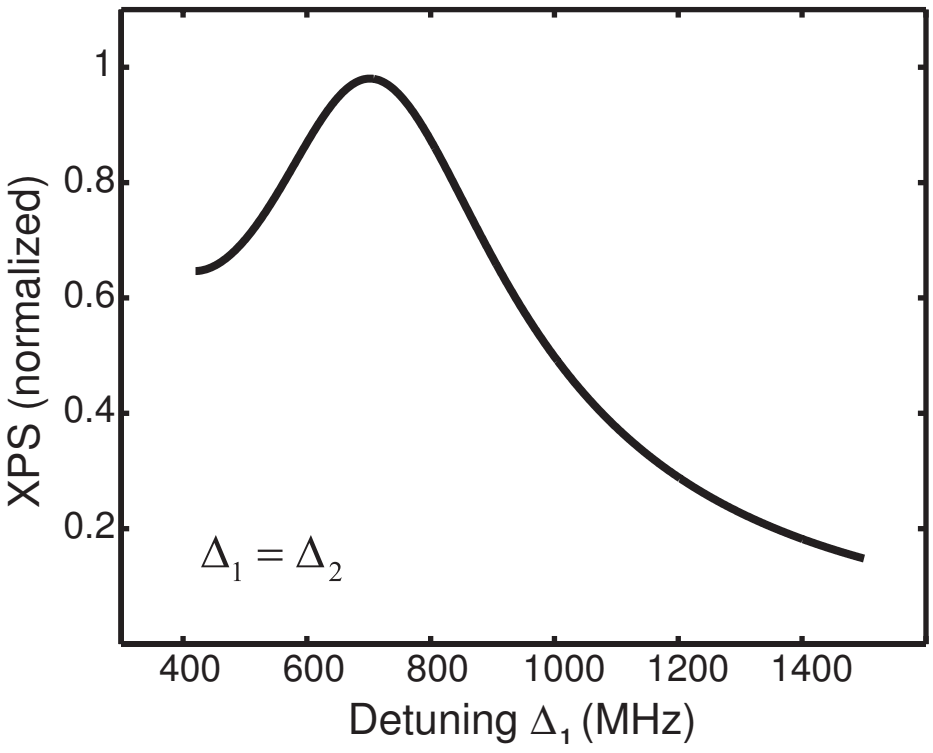

Figure 6.3: Optimum detuning for cross-phase modulation using a 3-level scheme. XPS induced on the meter beam with varying detuning of the signal beam from the intermediate $5P_{3/2}$ level, for an OD = 100 in the fiber and a given signal power.

where $L \sim 1$ cm is the sample length and α is the absorption coefficient of the signal. We assume α is given by a Doppler broadened Gaussian absorption profile as

$$\alpha(\Delta) = OD \exp(-\frac{\Delta^2}{w_D^2}), \tag{6.5}$$

where OD is the optical depth on resonance for the $5S_{1/2} \rightarrow 5P_{3/2}$ (D_2) transition, Δ is the detuning of the control beam from line center, and w_D is the Doppler width, which is a function of the temperature of the atoms. For the Rb atoms generated in the hollow core of the PBGF, $w_D \sim 325$ MHz [65].

From equations (6.2) and (6.1), n_2 for a particular detuning $\Delta_1 = \Delta_2 = \Delta \gg \gamma$,

where γ is the TPA linewidth, is of the form

$$n_2 \simeq \frac{n_2^0}{\Delta^3}, \tag{6.6}$$

where $n_2^0 \propto$ OD is a constant.

We thus compute $n_2(\Delta)$, $\alpha(\Delta)$ and L_{eff} for a particular detuning Δ using equations (6.6), (6.5) and (6.4), and then calculate the XPS induced at that detuning. Figure 6.3 shows the calculated XPS as a function of the detuning from the intermediate $5P_{3/2}$ level for an OD = 100. It is evident that maximum XPS is expected around ~700 MHz and going closer to resonance is deleterious because of absorption of the 780-nm signal beam. At this detuning, off-resonance absorption of the signal corresponds to an effective OD ~ 1 and tuning closer to resonance results in significant absorption of the signal. For the Rb-PBGF system, using an atomic density $N = 2 \times 10^{13}$ atoms/cm^3 which corresponds to an OD ~ 100, we estimate an effective nonlinear refractive index $n_2 = 3 \times 10^{-6}$ cm^2/W.

6.4 Experimental setup

The experimental setup is shown in Fig. 6.4. A hollow-core PBGF (Crystal Fiber AIR-6-800) is mounted inside a vacuum chamber with a Rb source attached. The fiber has a 6-μm diameter hollow core and guides light in the 750-810 nm wavelength range with a fundamental mode area given by 10^{-7} cm^2. The meter and signal lasers at 776 nm and 780.2 nm, respectively are coupled counter-propagating (to eliminate Doppler broadening of the XPM) into the core of the fiber using 10x objectives. A 3-mW highly non-resonant vapor generation beam at 805 nm is also coupled into the fiber to evaporate Rb nanoclusters adsorbed on the inside walls of the core [66, 67] and to generate a high OD ~100. The OD

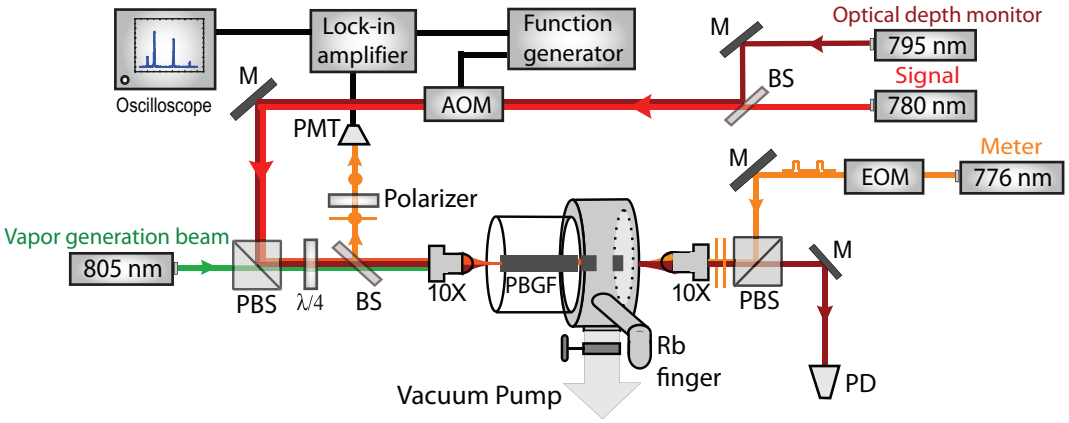

Figure 6.4: Experimental setup for few-photon cross-phase modulation. The linearly polarized meter and circularly polarized signal beams are coupled counter-propagating into the fiber. The meter beam undergoes slight polarization rotation due to cross-phase modulation from the weak signal beam. A polarizer is used at the output to select the meter polarization orthogonal to that at the input, and measured with a photomultiplier tube (PMT). An acousto-optic modulator (AOM) is used to amplitude modulate the signal at 25 kHz, and a lock-in amplifier detects the cross-phase shift imparted on the meter at the same frequency. A strong (3 mW) off-resonant vapor generation beam is also coupled into the fiber to generate the desired atomic density and optical depth. The optical depth is monitored during the experiment using a weak 795-nm beam scanning across the D_1 resonance of Rb. An electro-optic modulator (EOM) is used to make square pulses of varying duration from the meter beam for pulsed measurements.

is continuously monitored during the experiment using another laser at 795 nm scanning across the Rb D_1 line. The signal is circularly polarized (σ^+), and the meter is linearly polarized ($\mathbf{x} = \sigma^+ + \sigma^-$) at the input. Due to the relative values of the transition dipole moments of the $5S_{1/2} \rightarrow 5D_{5/2}$ two-photon transition [113], only the σ^+ component of the meter primarily experiences XPS. As a result, the polarization of the meter at the output of the fiber is $\sigma^+ + e^{-i\phi}\sigma^- \approx \mathbf{x} - (\phi/2)\mathbf{y}$ (for $\phi << 1$), where ϕ is the XPS in radians. The meter thus acquires a slight polarization rotation proportional to the XPS induced. A polarizer then selects

only the **y**-component of the meter polarization for detection to deduce the XPS. An acousto-optic modulator (AOM) is used to amplitude modulate the signal at 25 kHz, and a lock-in amplifier is utilized to detect the XPS imparted on the meter at the same frequency to improve the signal-to-noise ratio. The power in the meter beam is kept between 1 and 10 μW for all measurements.

In addition, for pulsed measurements, an electro-optic amplitude modulator (EOM) driven by a function/waveform generator is used to make square pulses of varying duration (5 - 200 ns) from the 776-nm meter beam. The time period of the pulse train is kept at least 5 times the pulse width for each measurement. The peak power in the meter beam pulses is kept the same (10 μW) for each measurement run. The 780-nm signal beam is kept CW and at the same power (20 nW) for all the measurements. After exiting the PBGF, the polarization of the meter orthogonal to that at the input is selected, the average power is measured using a sensitive but slow detector, and the amount of XPS is deduced. This procedure is repeated for each different value of the pulse width.

6.5 Non-demolition measurement of signal power

Figure 6.5 shows the XPS imparted on the meter as the signal is scanned in frequency to the blue of the $5S_{1/2} \rightarrow 5P_{3/2}$ ($F = 3 \rightarrow F' = 4$) transition. The meter beam has a fixed frequency such that $\Delta_1 = \Delta_2$. The data are shown for one continuous scan. Tens of milliradians of phase shift are observed even for detunings greater than 1 GHz from line center. The signal absorption at these detunings is <1%, so this is truly a non-demolition measurement of the signal intensity. The deviation of the experimental data from theory is due to slow

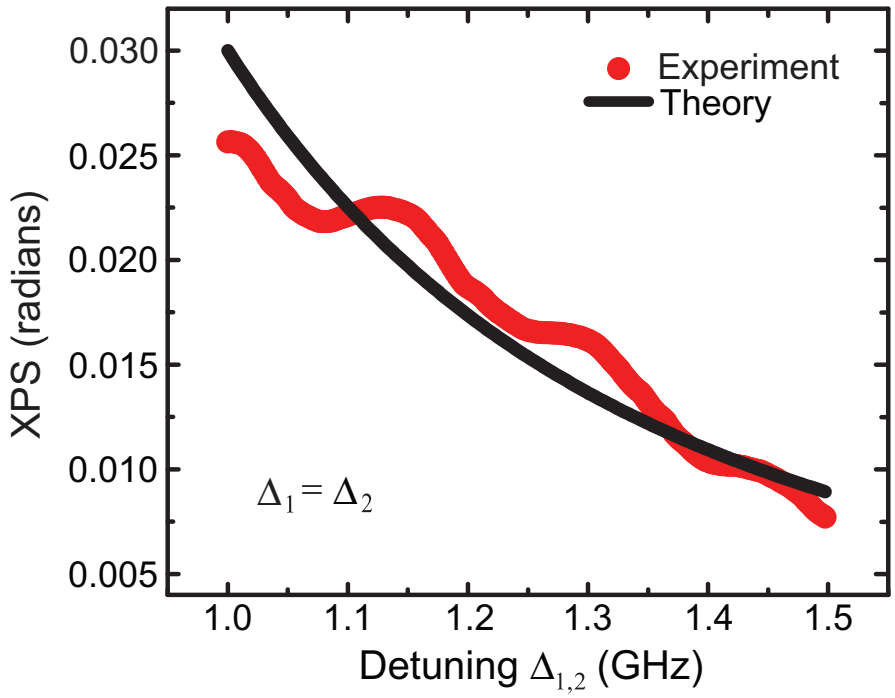

Figure 6.5: Non-demolition measurement of signal power. Cross-phase shift (XPS) imparted on the meter beam (red dots) versus detuning from two-photon resonance. The data are shown for one continuous scan of the laser. Tens of milliradians of phase shift are observed even for detunings greater than 1 GHz from line center. The signal absorption at these detunings is <1%. The signal power is 50 nW, and the OD in the fiber is ~50. The power in the meter beam is 2 μW. The solid black line shows the theoretical calculation taking into account the Doppler absorption profile of the atoms in the fiber core. The deviation of the experimental data from theory is due to slow drifts in the coupling and polarization maintenance of the PBGF as the laser is scanned in frequency at a rate of ~10 Hz.

drifts in the coupling and polarization maintenance of the PBGF as the laser is scanned in frequency at a rate of ~10 Hz.The signal power was 50 nW, while the meter power was 2 μW, and the OD in the fiber was 50. The XPS increases closer to resonance as expected from theory, but also results in greater absorption of the signal.

6.6 Response time and modulation bandwidth

In order to determine the response time of our system, we set up a pulsed measurement. An electro-optic modulator (EOM) is used to amplitude modulate the meter beam [see Fig. 6.4] and make square pulses of varying duration from 5 - 200 ns, and the average XPS is measured for each pulse width. The power in the meter beam was kept 5 times higher than in the previous CW measurement to improve the signal-to-noise ratio. The signal detuning Δ_1 and the two-photon detuning Δ_2 were both kept at 700 MHz for each measurement, where off-resonance absorption of the signal corresponds to an effective OD ~ 1. As the pulse width is reduced, the XPS decreases with a dependence as shown in Fig. 6.6.

We also theoretically calculate the XPS for each pulse width by averaging the nonlinear susceptibility spectral profile (plotted in Fig. 6.3) over the pulse bandwidth. The power spectrum of a square pulse of duration T is given by [99],

$$F(T,\omega) = N_0 sinc^2\left(\frac{\omega T}{2\pi}\right), \tag{6.7}$$

where $sinc(x) = \sin(\pi x)/(\pi x)$, and N_0 is a normalization constant such that $\int_{-\infty}^{+\infty} F(T,\omega)d\omega = 1$.

If the center frequency of the pulse corresponds to a detuning Δ, the XPS induced at $\Delta + \omega$, $\phi(\Delta + \omega)$, is calculated using the procedure described above involving equations (6.4), (6.5) and (6.6). For a pulse of duration T, the effective XPS induced at the detuning Δ is calculated as

$$\phi(T) = \int_{-\infty}^{+\infty} F(T,\omega)\phi(\Delta+\omega)d\omega, \tag{6.8}$$

In Fig. 6.6, the solid black line plots $\phi(T)$ for T varying from 1 - 300 ns for Δ = 700 MHz with no additional fitting parameters.

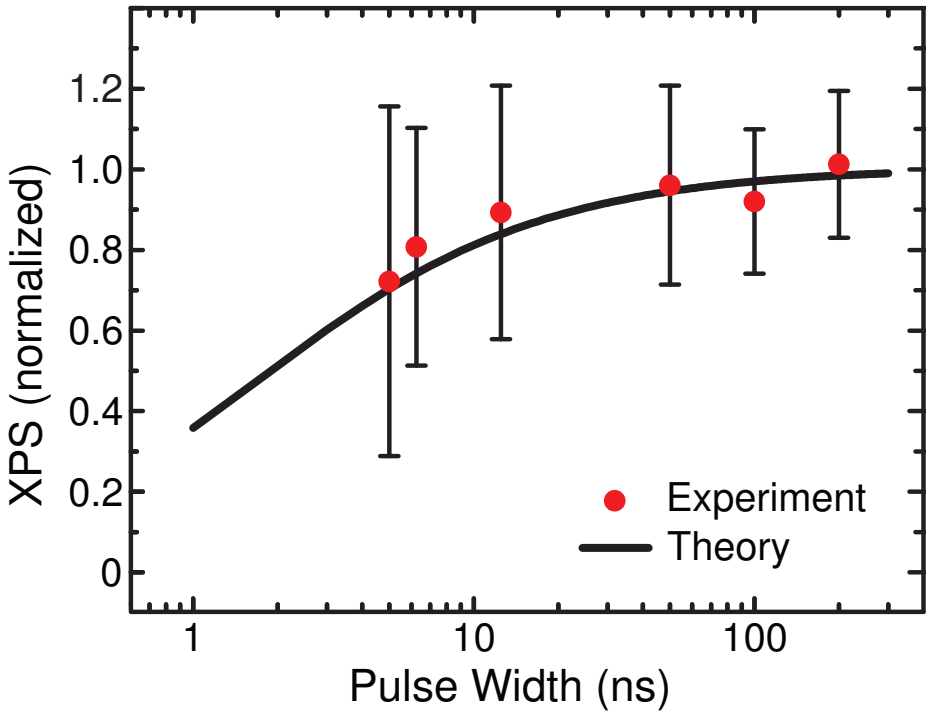

Figure 6.6: Pulsed XPM measurement. Average cross-phase shift (XPS) (red dots), relative to CW, imparted by the signal for varying pulse widths of the meter. Error bars indicate measurement noise (one standard deviation). Square pulses of the meter at 20% duty cycle are made using an electro-optic modulator (EOM). The signal detuning Δ_1 and the two-photon detuning Δ_2 were both kept at 700 MHz for each measurement. The peak power in the meter beam pulses is 10 μW and the CW signal power is 20 nW for each measurement run. The system response time is observed to be <5 ns, enabling phase modulation bandwidths >50 MHz. The experimental data are in excellent agreement with the theoretically predicted curve (black line).

The experimental data agree very well with the theoretically predicted curve, and the XPS remains close to the CW value for pulse widths down to 5 ns. As there are no fitting parameters in the theory curve, the response time of our Rb-PBGF system for this XPM scheme is thus <5 ns, indicating that phase modulation bandwidths greater than 50 MHz are therefore possible even with such a sensitive scheme.

6.7 Few-photon cross-phase modulation

Finally, we measured the XPS induced on the meter beam with varying power of the signal beam for an OD ~ 100 in the fiber. For each measurement, the signal detuning Δ_1 and the two-photon detuning Δ_2 were both kept at 700 MHz, and the power in the meter beam was 10 μW. As expected from equation (6.3), the XPS has a linear relationship with signal power as shown in Fig. 6.7. A few milliradians of phase shift is measurable even for sub-nanowatt signal power. The experimental data agrees well with the theoretical calculation.

We calculate the effective number of photons interacting within the response time τ of the system for a particular power P as

$$N_P = \frac{P\tau}{hc/\lambda}, \tag{6.9}$$

where hc/λ is the energy of one photon. Thus, for $P \sim 0.8$ nW and $\lambda = 780$ nm, taking $\tau \sim 5$ ns, we get $N_P \sim 16$ (the lowest point in the data of Fig. 6.7 in the main text). We thus measure a ~5 milliradian phase shift for only ~16 signal photons. The switching energy is $N_P hc/\lambda$, which corresponds to only ~5 aJ of

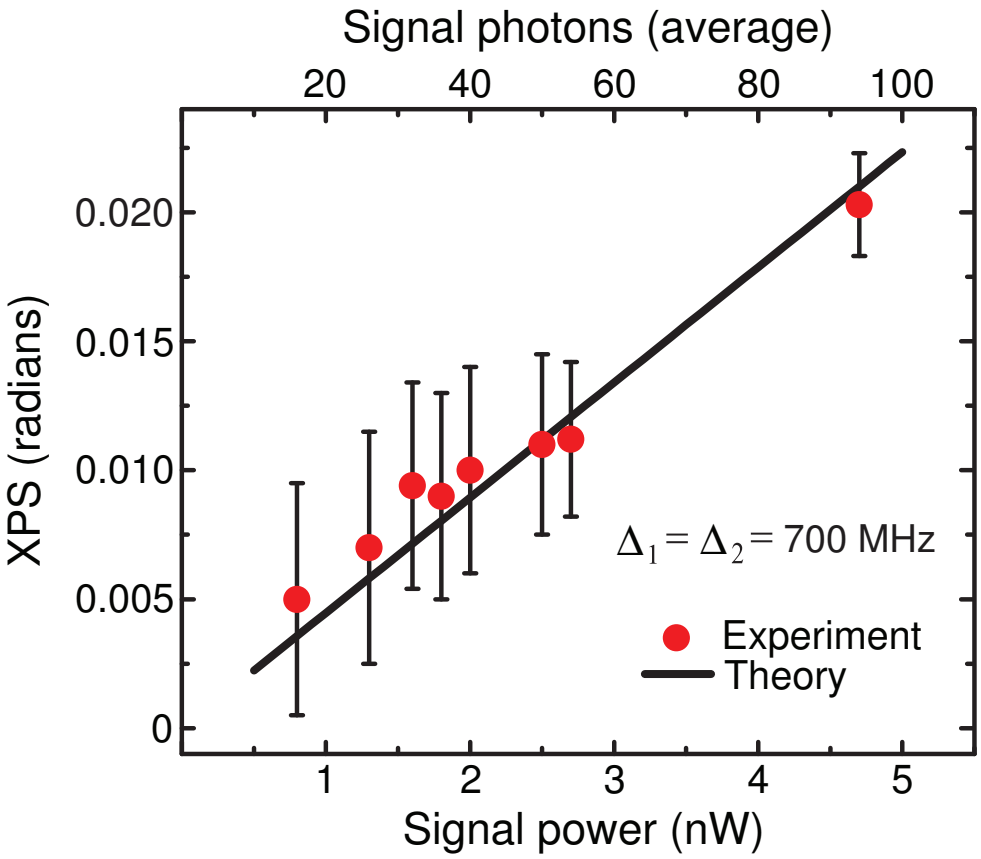

Figure 6.7: Large cross-phase modulation at the few-photon level. Cross-phase shift (XPS) imparted on the meter (red dots) as a function of average signal power (and average number of signal photons in a 5-ns pulse). Error bars indicate measurement noise (one standard deviation). An OD~100 is produced in the fiber for each measurement. The power in the meter beam was 10 μW for each measurement. A ~5 mrad phase shift is measured for ~16 signal photons, corresponding to ~5 aJ of energy. The solid black line shows the theoretical prediction, and the slope corresponds to an XPS of ~0.3 mrad per signal photon, which to our knowledge, represents the largest such nonlinear phase shift induced in a single-pass through a room-temperature medium.

signal energy. The number of photons per atomic cross-section is calculated as

$$\frac{N_P}{A}\left(\frac{3\lambda^2}{2\pi}\right), \tag{6.10}$$

where $A \sim 10^{-7}$ cm^2 is the optical mode area. Thus $P \sim 0.8$ nW corresponds to an energy density much less than one photon per atomic cross-section. From the slope of the solid black line in Fig. 6.7, we infer an XPS of 0.3 milliradian per signal photon, which to our knowledge, represents the largest such nonlinear phase shift induced in a single-pass through a room-temperature medium.

6.8 Summary and conclusion

In summary, we demonstrate large XPM at the few-photon level using a non-degenerate, two-photon transition in thermal Rb atoms confined to a hollow-core PBGF. A few milliradians of phase shift is induced on a meter beam with <20 signal photons, corresponding to a few attojoules of energy. The signal energy density is much less than one photon per atomic cross-section. We also characterize the time response of the system to be <5 ns, which enables large modulation bandwidths of >50 MHz for a highly sensitive atomic vapour-based scheme. A nonlinear refractive index value of $n_2 = 3 \times 10^{-6}$ cm^2/W and a phase shift of 0.3 milliradian per signal photon are inferred. Our system is thus able to access the regime where it can potentially be employed to realize weak-nonlinearity based quantum computing gates [34, 104, 105, 106, 107] and quantum non-demolition measurement of photon number [29, 105]. Our results with 'hot' atoms compare favourably with those achieved in previous experiments, including more elaborate and complicated cold-atom setups [35, 109, 110]. Moreover, our system enables us to explore a wide space of atomic density and

optical intensity in a controllable manner and holds promise for integration with fiber-optic communication networks [48]. These results show the potential of a Rb-PBGF system for exploring quantum nonlinear effects at ultralow powers.

CHAPTER 7

FUTURE DIRECTIONS

In this chapter, we discuss some possible future experiments that may be pursued using the Rb-PBGF system and some new directions to explore following the work reported in this thesis.

7.1 Coherent photon conversion

We explore the feasibility of a Rb-PBGF system to perform coherent photon conversion (CPC), a scheme recently proposed for realizing efficient quantum computing [114]. The basic idea behind CPC is to combine a third-order nonlinearity $\chi^{(3)}$ with an intense coherent field (pump) to realize a large effective second-order nonlinearity $\chi^{(2)}_{eff}$. Using this large engineered $\chi^{(2)}_{eff}$, photons can be coherently converted from one mode into two new modes, yielding new effective ways to generate and process states for photonic quantum computing. CPC can potentially be employed to realize deterministic multi-qubit entanglement gates (such as the universal controlled-phase gate), generate high-quality heralded single and multi-photon states, and improve single-photon detection efficiencies [114].

Consider a four-wave-mixing (FWM) interaction in a $\chi^{(3)}$ medium involving four different field modes a, b, c and d,

$$\hat{H} = \hbar\kappa\hat{a}\hat{b}^{\dagger}\hat{c}^{\dagger}\hat{d} + h.c., \tag{7.1}$$

where the coupling strength κ is given by

$$\kappa = \frac{c\gamma_{eff}\hbar\omega}{\tau}. \tag{7.2}$$

Here γ_{eff} is the effective nonlinearity of the $\chi^{(3)}$ medium (units of $W^{-1}m^{-1}$), ω is the angular frequency of the optical field(s), and τ is the inverse of the bandwidth of the field modes (or the pulse width in time). The effective nonlinearity of the medium γ_{eff} is given by [40]

$$\gamma_{eff} = \frac{2\pi}{\lambda}\frac{n_2}{A}, \tag{7.3}$$

where λ is the optical wavelength, n_2 is the second-order index of refraction (giving rise to the intensity dependent refractive index), and A is the optical mode area. The n_2 is related to $\chi^{(3)}$ as [40]

$$n_2\left(cm^2/W\right) = \left(2.82 \times 10^6\right)\chi^{(3)}, \tag{7.4}$$

where $\chi^{(3)}$ is in MKS units.

Pumping mode d in equation (7.1) with a bright classical beam yields an effective $\chi^{(2)}$ interaction

$$\hat{H}_{eff} = \hbar\Gamma\hat{a}\hat{b}^{\dagger}\hat{c}^{\dagger} + h.c., \tag{7.5}$$

where the effective coupling strength Γ is given by

$$\Gamma = \kappa\sqrt{N_P}. \tag{7.6}$$

Here N_P is the average number of pump photons per pulse of width τ in mode d.

Under an interaction such as (7.5), an input state $|100\rangle$ (corresponding to one photon in mode a, and none in modes b and c) will evolve to $\cos(\Gamma t)|100\rangle + i\sin(\Gamma t)|011\rangle$ after an interaction time t. To implement complete Rabi oscillations between $|100\rangle$ and $|011\rangle$, which is required for applications like controlled-phase gates [114], it is thus desired to have $\Gamma t \sim \pi/2$.

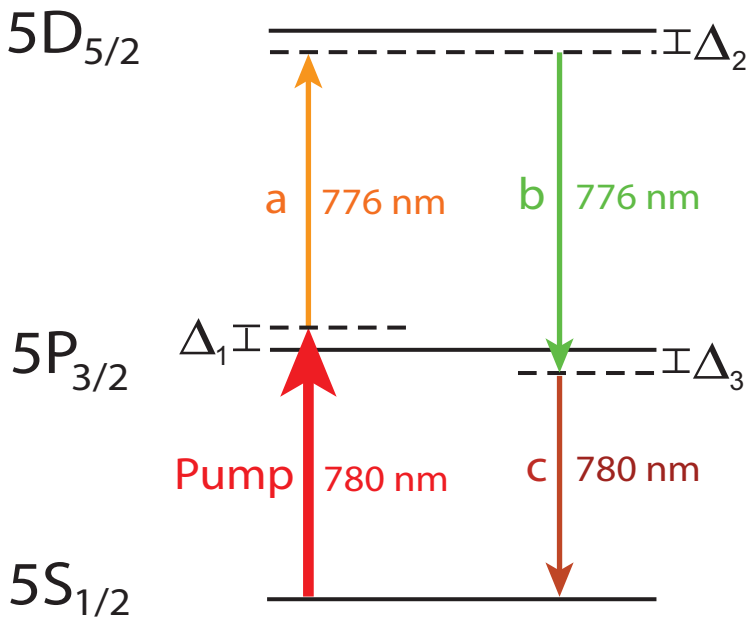

Figure 7.1: Four-wave mixing (FWM) level scheme in ^{85}Rb for performing coherent photon conversion (CPC). An atom in the ground $5S_{1/2}$ state undergoes a parametric nonlinear process involving a strong pump field and three weak (single-photon level) fields a, b and c.

In the experiment reported in [114], a nonlinear photonic crystal fiber was used as the FWM medium. The fiber had a $\gamma_{eff} \sim 0.1$ W^{-1}m^{-1} at $\lambda \sim 700$ nm. For $\tau \sim 10$-ps pump pulses at a repetition rate of 76 MHz, and an average power of ~1 W corresponding to $N_P \sim 10^{10}$ photons, they get $\Gamma \sim 10^5$ s^{-1}. Using a fiber length $z = 50$ cm, corresponding to a propagation/interaction time $t \sim 10^{-9}$ s, results in $\Gamma t \sim 10^{-4}$.

We consider here the possibility of using our Rb-PBGF system to implement CPC with much higher efficiency. We propose a FWM interaction using the $5S_{1/2} \rightarrow 5P_{3/2} \rightarrow 5D_{5/2}$ cascade of ^{85}Rb, as shown in Fig. 7.1.

The nonlinear susceptibility for such a scheme is given by [40, 115]

$$\chi^{(3)} \simeq \frac{N\mu_1^2\mu_2^2}{\varepsilon_0\hbar^3\Delta_1\Delta_2\Delta_3}, \tag{7.7}$$

where N is the atomic number density, μ_1 and μ_2 are the transition dipole moments for the $5S_{1/2} \rightarrow 5P_{3/2}$ and $5P_{3/2} \rightarrow 5D_{5/2}$ transitions, $\Delta_{1,2,3}$ are the one-, two- and three-photon detunings, respectively, as shown in Fig. 7.1. An optical depth of ~100 is routinely achieved in the Rb-PBGF system [65], corresponding to an atomic density $N = 2 \times 10^{13}$ atoms/cm^3. The Doppler width of the thermal atoms generated in the fiber core is ~ 325 MHz [65]. The frequencies of the input fields, i.e. the pump and mode a, are set such that $\Delta_1 \sim \Delta_2 \sim 2$ GHz. This is done to obtain a near resonant enhancement but also be far enough detuned to avoid linear and nonlinear absorption and spontaneous emission losses [115]. The spontaneous FWM process has a probability of generating photons in modes b and c distributed over a range of detunings Δ_3. Although the nonlinear susceptibility increases with decreasing Δ_3 according to equation (7.7), the absorption loss for the generated modes also increases. The net gain for modes b and c after propagation through the medium is thus optimum for a detuning $\Delta_3 \sim 2$ GHz [115].

Using equations (7.7) and (7.4), we get an $n_2 \sim 10^{-7}$ cm^2/W for the above mentioned parameters. The PBGF has a 6-μm diameter hollow core and guides light in the 750-810 nm wavelength range with a fundamental mode area given by 10^{-7} cm^2. Thus, using equation (7.3), we get $\gamma_{eff} \sim 10^7$ W^{-1}m^{-1}. Detunings of $\Delta \sim 2$ GHz would determine the response time of the system to be $\tau \sim 1/\Delta \sim$ 100 ps. A peak pump power of ~2 mW at λ = 780 nm would then correspond to $N_P \sim 10^6$ photons. Putting these values of γ_{eff}, N_P and τ into equations (7.6) and (7.2), we get $\Gamma \sim 10^{10}$ s^{-1}. A typical sample length $z \sim 1$ cm corresponds to a propagation time $t \sim 10^{-10}$ s, giving $\Gamma t \sim 1$.

The mW-level pump power required means that the experiment may be per-

formed CW. To separate the different modes (modes a and b would be ~4 GHz apart, the same for mode c and the pump), high-finesse etalons (temperature-controlled) may be employed. In addition, polarization separation may also be used by using a scheme with cross-polarized modes (say the pump and mode a having H-polarization, and modes b and c having V-polarization). One should also note that the pump power cannot be increased arbitrarily to increase the effective coupling strength as this would give rise to noise from unwanted processes (e.g. FWM with two pump photons (modulation instability)). It is probably desirable to restrict pump power levels to mW or below.

The FWM process should be phase-matched if all four modes are co-propagating in the fiber [115], since $\Delta k = k_{pump} + k_a - k_b - k_c = 0$, where $k_i \simeq \omega_i/c$ is the wavenumber of mode i. If one wants to use a counter-propagating geometry, the phase mismatch Δk would be minimum for the case when the pump and mode c are propagating in one direction, and modes a and b are propagating in the opposite direction (note that one still needs to separate the two co-propagating modes in each direction which are ~4 GHz apart). Then, $\Delta k = k_{pump} - k_c + k_b - k_a \simeq 2(\Delta_1 + \Delta_3)/c \sim 2\ \mathrm{cm}^{-1}$, where $\Delta_{1,3} \sim 2$ GHz. The walk-off length L, corresponding to $\Delta k L \sim 1$, would then be ~ 0.5 cm. This is close to the typical sample length (~1 cm) in a Rb-PBGF system.

7.2 Quantum frequency conversion via Bragg scattering

Bragg scattering is a four-wave mixing (FWM) process with two non-degenerate pumps that results in wavelength exchange between weak signal and idler fields [116]. For each idler photon that is created, a signal photon is destroyed

and vice-versa, causing an exchange in power between the two frequency modes. Since the total signal plus idler power is conserved, vacuum fluctuations are not amplified and quantum states of single-photons can be noiselessly translated from one frequency mode to another [117]. Bragg-scattering thus acts as a beam-splitter in frequency space, enabling creation of frequency superposition and entangled states for use in quantum computation and communication. Such quantum frequency conversion is also important for connecting disparate quantum system and building quantum networks because the optimum photon frequencies required for encoding, transmission, storage and detection of quantum information may all be different from each other.

The Hamiltonian for a FWM Bragg-scattering interaction is given by

$$\hat{H} = \hbar c \kappa \hat{a} \hat{b}^{\dagger} + h.c., \tag{7.8}$$

where a is the signal mode, b is the idler mode, $\kappa = \gamma_{eff} \sqrt{P_{p1} P_{p2}}$ is the coupling strength, γ_{eff} is the effective nonlinearity of the $\chi^{(3)}$ medium (units of $\mathrm{W^{-1}m^{-1}}$), and P_{p1} and P_{p2} are the powers of the two pump modes. Under such an interaction, an input state $|10\rangle$ (corresponding to one photon in mode a, and none in mode b) will evolve to $\cos(\kappa z)|10\rangle + i \sin(\kappa z)|01\rangle$ after an interaction length z. To implement complete Rabi oscillations between $|10\rangle$ and $|01\rangle$, which is required for quantum information applications, it is thus desired to have $\kappa z \sim \pi/2$.

In the experiment reported in [118], a nonlinear photonic crystal fiber was used as the FWM medium and single-photon states were translated from λ = 683 nm to λ = 659 nm with ~25% efficiency. The fiber had a $\gamma_{eff} \sim 0.1$ $\mathrm{W^{-1}m^{-1}}$ at $\lambda \sim 700$ nm. Using a fiber length z = 20 m and average pump powers of ~25 mW (100-ps pump pulses at a repetition rate of 76 MHz), they get $\kappa z \sim 0.5$.

We consider here the possibility of using our Rb-PBGF system to implement

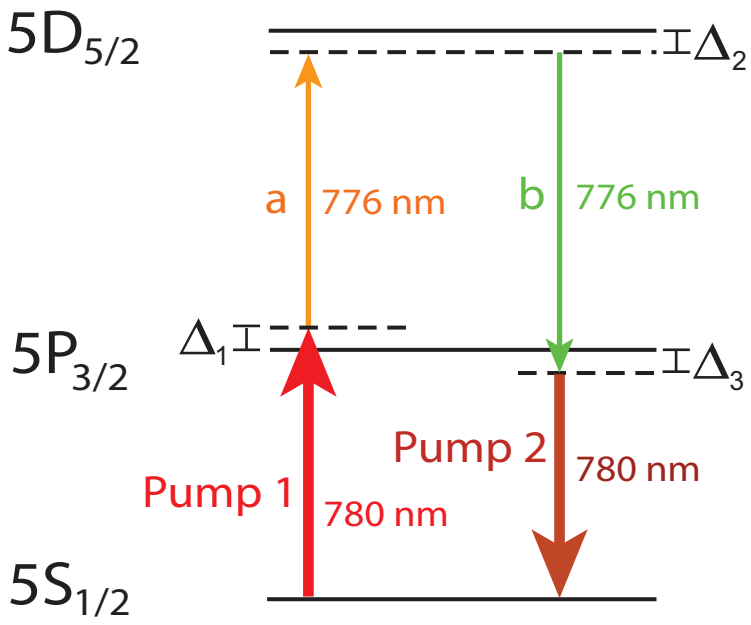

Figure 7.2: Four-wave mixing (FWM) level scheme in ^{85}Rb for performing quantum frequency conversion using Bragg scattering. Atoms in the ground $5S_{1/2}$ state undergo a parametric nonlinear process involving two strong pump fields, converting single-photon states from the signal mode a to the idler mode b.

quantum frequency conversion with much higher efficiency at much lower pump powers. We propose performing Bragg scattering using the same FWM interaction on the $5S_{1/2} \rightarrow 5P_{3/2} \rightarrow 5D_{5/2}$ cascade of ^{85}Rb, as shown in Fig. 7.2. Again, if the frequencies of the input fields are set such that $\Delta_1 \sim \Delta_2 \sim \Delta_3$ 2 GHz, as in the CPC case discussed above, and for a typical optical depth ~ 100, we get $\gamma_{eff} \sim 10^7$ W^{-1}m^{-1} for our Rb-PBGF system. Low pump powers $P_{p1} \sim P_{p2} \sim 10\ \mu$W, and a typical sample length $z \sim 1$ cm, can yield $\kappa z \sim 1$. For $P_{p1} \sim P_{p2} \sim 30\ \mu$W, one can get $\kappa z \sim \pi$, thus covering the entire range of conversion from signal to idler and back. Moreover, the experiment can be performed CW.

The phase-matching considerations are identical to those in the CPC case discussed above, and the same techniques for separating the different modes

may be employed. Since the pumps are 4-nm away from the signal and idler modes, pump extinction may be easier to achieve in this case. One may also interchange one of the pumps and the weak fields to get conversion between 776 nm and 780 nm, although pump extinction in this case will be more difficult.

7.3 Other general directions

Modifications to the Rb-PBGF system may be explored to increase light-matter interaction and further enhance the nonlinear optical effects reported in this thesis. Building a cavity around the fiber would both increase the intensity of the light and the effective interaction length (or optical depth) by a factor of the finesse. This may enable one to extend the four-wave mixing studies discussed earlier and build an ultralow threshold optical parametric oscillator (OPO). A finesse of ~10 should result in an improvement in the all-optical switching using two-photon absorption such that significant effects may be measurable at the single-photon level. Such a cavity would also enhance the cross-phase shift induced per photon for non-demolition measurements.

Another direction that may be pursued is to investigate techniques to push the Rb atoms further down into the PBGF core and increasing the interaction length beyond the current typical value of ~1 cm, resulting in a larger OD. Possible techniques here could include light-induced-drift (LID) in the presence of buffer gases [119] and/or introducing a vapor-generation beam from the side of the fiber to evaporate the nanoclusters with higher optical power [67]. Finally, exploring avenues to reduce the ground-state decoherence rate of the Rb atoms by increasing the transit-time across the fiber core, maybe again through

collisions with a buffer gas [54, 67, 120], could also prove worthwhile.

In the long term, developing the technology to splice hollow-core PBGFs containing adsorbed Rb nanoclusters inside to standard solid-core fibers in vacuum would be an intriguing prospect. This might lead to all-fiber Rb-PBGF systems that can be operated in the ambient environment and easily integrated into fiber-optic communication networks [48].

APPENDIX A

RUBIDIUM ENERGY LEVELS

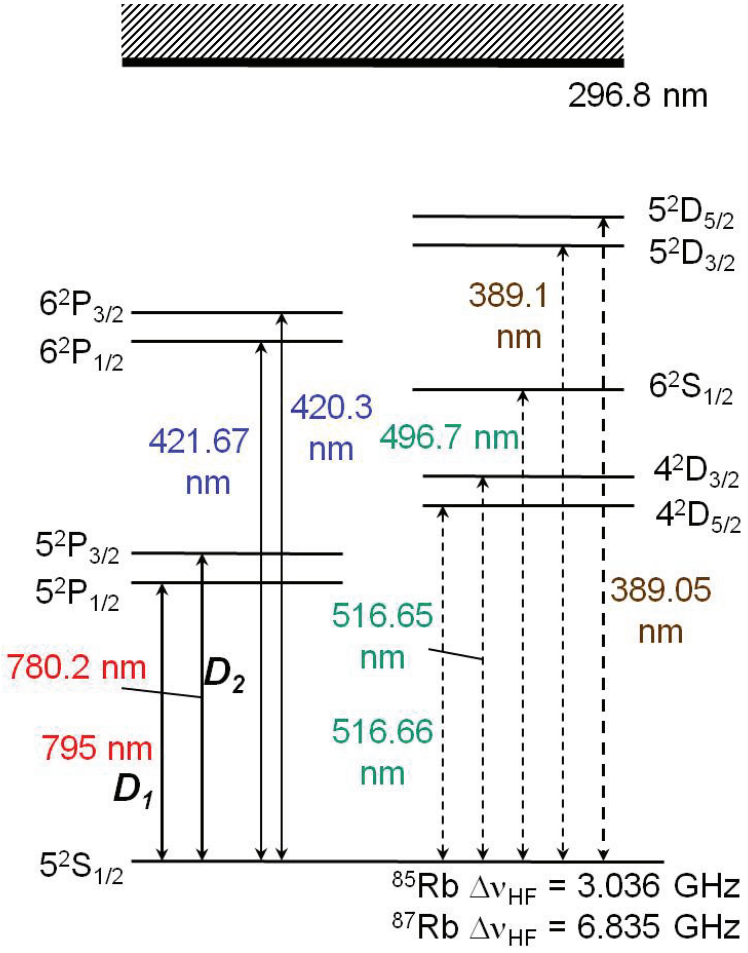

Figure A.1: Energy level structure of Rb. The ground state of the lone valence electron is the $5S_{1/2}$ level. The first few excited states are shown along with the wavelengths of photons having energy equal to the transition energies. The solid lines denote dipole-allowed single-photon transitions. The dashed lines denote higher order (two-photon) transitions. The dashed box on top denotes the vacuum level. The ground $5S_{1/2}$ state is hyperfine split into two levels, and the splitting is different for the two isotopes ^{85}Rb and ^{85}Rb. The experiments reported in this thesis employ the $5S_{1/2} \rightarrow 5D_{5/2}$ two-photon transition at $\lambda = 778.1$ nm (389.05×2), and also the $5P_{3/2} \rightarrow 5D_{5/2}$ transition at $\lambda = 776$ nm, in addition to the D_1 and D_2 lines.

BIBLIOGRAPHY

[1] A. A. Sawchuck, Proc. IEEE **72**, 758 (1984).

[2] A. Huang, Proc. IEEE **72**, 780 (1984).

[3] R. Ramaswami, K. Sivarajan, and G. Sasaki, *Optical Networks: A Practical Perspective* (Morgan Kaufmann, 2009).

[4] H. M. Gibbs, *Optical Bistability: Controlling Light with Light* (Academic Press, 1985).

[5] T. Baehr-Jones, M. Hochberg, and A. Scherer, IEEE J. Sel. Top. Quantum Electron. **14**, 1335 (2008).

[6] D. A. B. Miller, Nat. Photon. **4**, 3 (2010).

[7] D. Bouwmeester, A. K. Ekert, and A. Zeilinger, *The Physics of Quantum Information* (Springer, 2000).

[8] M. D. Lukin, Rev. Mod. Phys. **75**, 457 (2003).

[9] D. Petrosyan, J. Opt. B: Quantum Semiclass. Opt. **7**, S141 (2005).

[10] J. L. O'Brien, Science **318**, 1567 (2007).

[11] H. Schmidt and A. Imamoglu, Opt. Lett. **21**, 1936 (1996).

[12] I. Schuster, A. Kubanek, A. Fuhrmanek, T. Puppe, P. W. H. Pinkse, K. Murr, and G. Rempe, Nature Phys. **4**, 382 (2008).

[13] B. Dayan, A. S. Parkins, T. Aoki, E. P. Otsby, K. J. Vahala, and H. J. Kimble, Science **319**, 1062 (2008).

[14] A. M. C. Dawes, L. Illing, S. M. Clark, and D. J. Gauthier, Science **308**, 672 (2005).

[15] M. Vengalattore, M. Hafezi, M. D. Lukin, and M. Prentiss, Phys. Rev. Lett. **101**, 063 901 (2008).

[16] D. A. Braje, V. Balic, G. Y. Yin, and S. E. Harris, Phys. Rev. A **68**, 041 801(R) (2003).

[17] M. Bajcsy, S. Hofferberth, V. Balic, T. Peyronel, M. Hafezi, A. S. Zibrov, V. Vuletic, and M. D. Lukin, Phys. Rev. Lett. **102**, 203 902 (2009).

[18] S. E. Harris and Y. Yamamoto, Phys. Rev. Lett. **81**, 3611 (1998).

[19] J. D. Franson, B. C. Jacobs, and T. B. Pittman, Phys. Rev. A **70**, 062 302 (2004).

[20] P. Kok, W. J. Munro, K. Nemoto, T. C. Ralph, J. P. Dowling, and G. J. Milburn, Rev. Mod. Phys. **79**, 135 (2007).

[21] N. Matsuda, R. Shimizu, Y. Mitsumori, H. Kosaka, and K. Edamatsu, Nat. Photon. **3**, 95 (2009).

[22] G. J. Pryde, J. L. OBrien, A. G. White, S. D. Bartlett, and T. C. Ralph, Phys. Rev. Lett. **92**, 190 402 (2004).

[23] P. Grangier, J. F. Roch, and G. Roger, Phys. Rev. Lett. **66**, 1418 (1991).

[24] H. Schmidt and A. R. Hawkins, Laser Photon. Rev. **4**, 720 (2003).

[25] D. M. Greenberger, M. A. Horne, A. Shimony, and A. Zeilinger, Am. J. Phys. **58**, 1131 (1990).

[26] E. Knill, R. Laflamme, and G. J. Milburn, Nature **409**, 46 (2001).

[27] B. C. Jacobs, T. B. Pittman, and J. D. Franson, Phys. Rev. A **74**, 010 303(R) (2006).

[28] B. C. Jacobs and J. D. Franson, Phys. Rev. A **79**, 063 830 (2009).

[29] N. Imoto, H. A. Haus, and Y. Yamamoto, Phys. Rev. A **32**, 2287 (1985).

[30] G. J. Milburn, Phys. Rev. Lett. **62**, 2124 (1989).

[31] D. Deutsch and R. Jozsa, Proc. R. Soc. London Ser. A **439**, 553 (1992).

[32] I. L. Chuang and Y. Yamamoto, Phys. Rev. A **52**, 3489 (1995).

[33] J. H. Shapiro, Phys. Rev. A **73**, 062 305 (2006).

[34] W. J. Munro, K. Nemoto, and T. P. Spiller, New J. Phys. **7**, 137 (2005).

[35] H. Kang and Y. Zhu, Phys. Rev. Lett. **91**, 093 601 (2003).

[36] D. A. Steck, http://steck.us/alkalidata/ (2010).

[37] J. Sherson, A. S. Sorensen, J. Fiurasek, K. Molmer, and E. S. Polzik, Phys. Rev. A **74**, 011 802(R) (2006).

[38] M. D. Lukin, A. B. Matsko, M. Fleischhauer, and M. O. Scully, Phys. Rev. Lett. **82**, 1847 (1999).

[39] A. S. Zibrov, M. D. Lukin, and M. O. Scully, Phys. Rev. Lett. **83**, 4049 (1999).

[40] R. W. Boyd, *Nonlinear Optics* (Academic Press, 2008).

[41] K. M. Birnbaum, A. Boca, R. Miller, A. D. Boozer, T. E. Northup, and H. J. Kimble, Nature **436**, 87 (2005).

[42] T. Wilk, S. C. Webster, A. Kuhn, and G. Rempe, Science **317**, 488 (2007).

[43] F. L. Kien, S. D. Gupta, V. I. Balykin, and K. Hakuta, Phys. Rev. A **72**, 032 509 (2005).

[44] T. Aoki, B. Dayan, E. Wilcut, W. P. Bowen, A. S. Parkins, T. J. Kippenberg, K. J. Vahala, and H. J. Kimble, Nature **443**, 671 (2006).

[45] S. M. Spillane, G. S. Pati, K. Salit, M. Hall, P. Kumar, R. G. Beausoleil, and M. S. Shahriar, Phys. Rev. Lett. **100**, 233 602 (2008).

[46] S. Ghosh, A. R. Bhagwat, C. K. Renshaw, S. Goh, A. L. Gaeta, and B. J. Kirby, Phys. Rev. Lett. **97**, 023 603 (2006).

[47] W. Yang, D. B. Conkey, B. Wu, D. Yin, A. R. Hawkins, and H. Schmidt, Nat. Photon. **1**, 331 (2007).

[48] F. Benabid, F. Couny, J. C. Knight, T. A. Birks, and P. S. J. Russell, Nature **434**, 488 (2005).

[49] R. Stites, M. Beeler, L. Feeney, S. Kim, and S. Bali, Opt. Lett. **29**, 2713 (2004).

[50] A. B. Matsko, I. Novikova, M. O. Scully, and G. R. Welch, Phys. Rev. Lett. **87**, 133 601 (2001).

[51] S. Chu, J. E. Bjorkholm, A. Ashkin, and A. Cable, Phys. Rev. Lett. **57**, 314 (1986).

[52] T. Takekoshi and R. J. Knize, Phys. Rev. Lett. **98**, 210 404 (2007).

[53] J. C. Camparo, J. Chem. Phys. **86**, 1533 (1987).

[54] W. Happer, Rev. Mod. Phys. **44**, 169 (1972).

[55] A. R. Bhagwat and A. L. Gaeta, Opt. Express **16**, 5035 (2008).

[56] D. G. Ouzounov, F. R. Ahmad, D. Muller, N. Venkataraman, M. T. Gallagher, M. G. Thomas, J. Silcox, K. W. Koch, and A. L. Gaeta, Science **301**, 1702 (2008).

[57] F. Benabid, J. C. Knight, G. Antonopoulos, and P. S. J. Russell, Science **298**, 399 (2002).

[58] S. Ghosh, J. E. Sharping, D. G. Ouzounov, and A. L. Gaeta, Phys. Rev. Lett. **94**, 093 902 (2005).

[59] F. Couny, F. Benabid, P. J. Roberts, P. S. Light, and M. G. Raymer, Science **318**, 1118 (2007).

[60] F. Benabid, P. S. Light, F. Couny, and P. S. J. Russell, Opt. Express **13**, 5694 (2005).

[61] P. Yeh and A. Yariv, Opt. Commun. **19**, 427 (1976).

[62] R. F. Cregan, B. J. Mangan, J. C. Knight, T. A. Birks, P. S. J. Russell, P. J. Roberts, and D. C. Allan, Science **285**, 1537 (1999).

[63] C. J. Hensley, D. G. Ouzounov, A. L. Gaeta, N. Venkataraman, M. T. Gallagher, and K. W. Koch, Opt. Express **15**, 3507 (2007).

[64] http://www.nktphotonics.com/files/files/Air-6-800-040611.pdf.

[65] A. D. Slepkov, A. R. Bhagwat, V. Venkataraman, P. Londero, and A. L. Gaeta, Opt. Express **16**, 18 976 (2008).

[66] A. R. Bhagwat, A. D. Slepkov, V. Venkataraman, P. Londero, and A. L. Gaeta, Phys. Rev. A **79**, 063 809 (2009).

[67] A. R. Bhagwat, *Low-light-level nonlinear optics with rubidium atoms in hollow-core photonic band-gap fibers*, Ph.D. thesis, Cornell University (2010).

[68] A. D. Slepkov, A. R. Bhagwat, V. Venkataraman, P. Londero, and A. L. Gaeta, Phys. Rev. A **81**, 053 825 (2010).

[69] E. B. Alexandrov, M. V. Balabas, D. Budker, D. English, D. F. Kimball, C.-H. Li, and V. V. Yashchuk, Phys. Rev. A **66**, 042 903 (2002).

[70] G. M. Guryanov, A. D. Slepkov, A. L. Gaeta, and K. W. Koch, Surf. Interface Anal. **43**, 566 (2011).

[71] A. Gozzini, F. Mango, J. H. Xu, G. Alzetta, F. Maccarrone, and R. A. Bernheim, Nuovo Cimento D **15**, 709 (1993).

[72] P. R. Hemmer, D. P. Katz, J. Donoghue, M. Cronin-Golomb, M. S. Shahriar, and P. Kumar, Opt. Lett. **20**, 982 (1995).

[73] D. A. Braje, V. Balic, S. Goda, G. Y. Yin, and S. E. Harris, Phys. Rev. Lett. **93**, 183 601 (2004).

[74] C. F. McCormick, V. Boyer, E. Arimondo, and P. D. Lett, Opt. Lett. **32**, 178 (2007).

[75] C. H. van der Wal, M. D. Eisaman, A. Andre, R. L. Walsworth, D. F. Phillips, A. S. Zibrov, and M. D. Lukin, Science **301**, 196 (2003).

[76] V. Boyer, C. F. McCormick, E. Arimondo, and P. D. Lett, Phys. Rev. Lett. **99**, 143 601 (2007).

[77] A. Andre, *Nonclassical states of light and atomic ensembles: Generation and new applications*, Ph.D. thesis, Harvard University (2005).

[78] R. E. Slusher, L. W. Hollberg, B. Yurke, J. C. Mertz, and J. F. Valley, Phys. Rev. Lett. **55**, 2409 (1985).

[79] J. E. Field, K. H. Hahn, and S. E. Harris, Phys. Rev. Lett. **67**, 3062 (1991).

[80] B. J. Dalton, R. McDuff, and P. L. Knight, J. Mod. Opt. **32**, 61 (1985).

[81] B. S. Ham and P. R. Hemmer, Phys. Rev. Lett. **84**, 4080 (2000).

[82] P. Londero, V. Venkataraman, A. R. Bhagwat, A. D. Slepkov, and A. L. Gaeta, Phys. Rev. Lett. **103**, 043 602 (2009).

[83] M. Erhard and H. Helm, Phys. Rev. A **63**, 043 813 (2001).

[84] M. M. Hossain, S. Mitra, B. Ray, and P. N. Ghosh, Laser Phys. **19**, 2008 (2009).

[85] D. E. Roberts and E. N. Forston, Phys. Rev. Lett. **31**, 1539 (1973).

[86] P. Lambropoulos, C. Kikuchi, and R. K. Osborn, Phys. Rev. **144**, 1081 (1966).

[87] D. D. Yavuz, Phys. Rev. A **74**, 053 804 (2006).

[88] W. H. D. von der Goltz and J. Richter, Phys. Scr. **30**, 244 (1984).

[89] M. D. Levenson and N. Bloembergen, Phys. Rev. Lett. **32**, 645 (1974).

[90] V. Venkataraman, P. Londero, A. R. Bhagwat, A. D. Slepkov, and A. L. Gaeta, Opt. Lett. **35**, 2287 (2010).

[91] S. M. Hendrickson, M. M. Lai, T. B. Pittman, and J. D. Franson, Phys. Rev. Lett. **105**, 173 602 (2010).

[92] F. Nez, F. Biraben, R. Felder, and Y. Millerioux, Opt. Commun. **102**, 432 (1993).

[93] W. Demtroder, *Laser Spectroscopy* (Springer-Verlag, 1982).

[94] K. Shimoda, *High-Resolution Spectroscopy, Vol. 13* (Springer-Verlag, 1976).

[95] J. E. Bjorkholm and P. F. Liao, IEEE J. Quantum Electron. **10**, 906 (1974).

[96] F. Biraben, B. Cagnac, and G. Grynberg, Phys. Rev. Lett. **32**, 643 (1974).

[97] K. Saha, V. Venkataraman, P. Londero, and A. L. Gaeta, Phys. Rev. A **83**, 033 833 (2011).

[98] S. N. Bagayev, V. P. Chebotayev, and E. A. Titov, Laser Phys. **4**, 224 (1994).

[99] D. W. Kammler, *A First Course in Fourier Analysis* (Cambridge University Press, 2007).

[100] Q. A. Turchette, C. J. Hood, W. Lange, H. Mabuchi, and H. J. Kimble, Phys. Rev. Lett. **75**, 4710 (1995).

[101] I. Fushman, D. Englund, A. Faraon, N. Stoltz, P. Petroff, and J. Vuckovic, Science **320**, 769 (2008).

[102] M. D. Lukin and A. Imamoglu, Phys. Rev. Lett. **84**, 1419 (2000).

[103] J. Gea-Banacloche, Phys. Rev. A **81**, 043 823 (2010).

[104] T. P. Spiller, K. Nemoto, S. L. Braunstein, W. J. Munro, P. van Loock, and G. J. Milburn, New J. Phys. **8**, 30 (2006).

[105] W. J. Munro, K. Nemoto, R. G. Beausoleil, and T. P. Spiller, Phys. Rev. A **71**, 033 819 (2005).

[106] K. Nemoto and W. J. Munro, Phys. Rev. Lett. **93**, 250 502 (2004).

[107] S. D. Barrett, P. Kok, K. Nemoto, R. G. Beausoleil, W. J. Munro, and T. P. Spiller, Phys. Rev. A **71**, 060 302(R) (2005).

[108] H. Chang, Y. Du, J. Yao, C. Xie, and H. Wang, Europhys. Lett. **65**, 485 (2004).

[109] H.-Y. Lo, P.-C. Su, and Y.-F. Chen, Phys. Rev. A **81**, 053 829 (2010).

[110] B.-W. Shiau, M.-C. Wu, C.-C. Lin, and Y.-C. Chen, Phys. Rev. Lett. **106**, 193 006 (2011).

[111] J. P. Poizat and P. Grangier, Phys. Rev. Lett. **70**, 271 (1993).

[112] V. Venkataraman, K. Saha, P. Londero, and A. L. Gaeta, Phys. Rev. Lett. **107**, 193 902 (2011).

[113] A. J. Olson, E. J. Carlson, and S. K. Mayer, Am. J. Phys. **74**, 218 (2006).

[114] N. K. Langford, S. Ramelow, R. Prevedel, W. J. Munro, G. J. Milburn, and A. Zeilinger, Nature **478**, 360 (2011).

[115] M. S. Malcuit, D. J. Gauthier, and R. W. Boyd, Phys. Rev. Lett. **55**, 1086 (1985).

[116] K. Uesaka, K. K.-Y. Wong, M. E. Marhic, and L. G. Kazovsky, IEEE J. Sel. Top. Quantum Electron. **8**, 560 (2002).

[117] C. J. McKinstrie, J. D. Harvey, S. Radic, and M. G. Raymer, Opt. Express **13**, 9131 (2005).

[118] H. J. McGuinness, M. G. Raymer, C. J. McKinstrie, and S. Radic, Phys. Rev. Lett. **105**, 093 604 (2010).

[119] H. G. C. Werij, J. E. M. Haverkort, and J. P. Woerdman, Phys. Rev. A **33**, 3270 (1986).

[120] W. Franzen, Phys. Rev. **115**, 850 (1959).